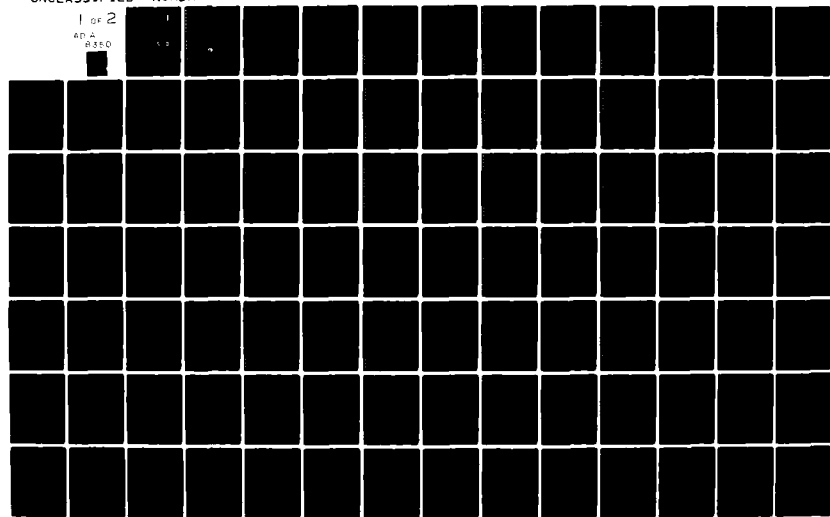


AD-A118 350 NAVAL OCEAN RESEARCH AND DEVELOPMENT ACTIVITY NSTL S--ETC F/G 8/3
A NUMERICAL STUDY OF LOOP CURRENT INTRUSIONS AND EDDY SHEDDING, (U)
JUN 80 H E HURLBURT, J D THOMPSON

UNCLASSIFIED NORDA-TN-64

NL

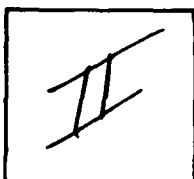
1 of 2
AP A
R350



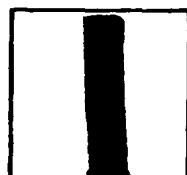
PHOTOGRAPH THIS SHEET

AD A118350

DTIC ACCESSION NUMBER



LEVEL



INVENTORY

NORDA Tech Note 64

DOCUMENT IDENTIFICATION

May 80

DISTRIBUTION STATEMENT A

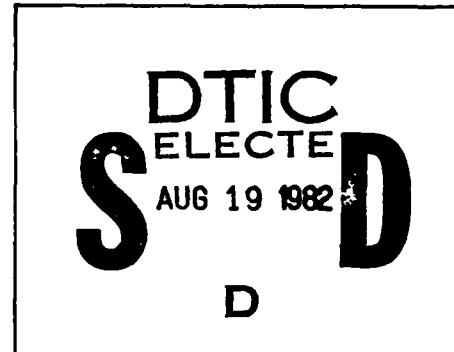
Approved for public release;
Distribution Unlimited

124

DISTRIBUTION STATEMENT

ACCESSION FOR	
NTIS	GRA&I
DTIC	TAB
UNANNOUNCED	
JUSTIFICATION	
BY	
DISTRIBUTION /	
AVAILABILITY CODES	
DIST	AVAIL AND/OR SPECIAL
A	

DISTRIBUTION STAMP



DATE ACCESSIONED



82 08 18 026

DATE RECEIVED IN DTIC

PHOTOGRAPH THIS SHEET AND RETURN TO DTIC-DDA-2

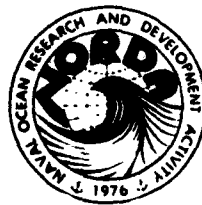
AD A118350

NORDA Technical Note 64

**A Numerical Study of Loop Current
Intrusions and Eddy Shedding**

H. E. Hurlburt
J. Dana Thompson

May 1980



**Environmental Simulation Branch
Code 322**

**NAVAL OCEAN RESEARCH AND DEVELOPMENT ACTIVITY
NSTL Station, Mississippi 39529**

DISTRIBUTION STATEMENT A

Approved for public release
Distribution Unlimited

ABSTRACT

The dynamics of the eddy shedding by the Loop Current in the Gulf of Mexico have been investigated using three nonlinear numerical models: two-layer, barotropic, and reduced gravity. The barotropic and reduced gravity models demonstrate the individual behavior of the external and internal modes, and provide insight into how they interact in the two-layer model. Because of the economy of the semi-implicit free surface models, it was possible to perform over 100 experiments to investigate the stability properties of the Loop Current. Typically the models were integrated 3 to 5 years to statistical equilibrium on a 1600×900 km rectangular domain with a resolution of 20×18.75 km. Prescribed inflow through the model Yucatan Channel was compensated by outflow through the Florida Straits.

A long-standing hypothesis is that the Loop Current sheds eddies in response to quasi-annual variations in the inflow. We find that the Loop Current can penetrate into the Gulf, bend westward, and shed realistic anticyclonic eddies at almost an annual frequency with no time variation in the inflow. In this regime, the eddy shedding rate depends on the internal Rossby wave speed, an eddy diameter derived from conservation of potential vorticity on a β -plane, the angle of the inflow, and to a lesser extent on the Reynolds number. Eddy shedding can be prevented by reducing the Reynolds number sufficiently. However, the Loop Current still spreads far westward. The steady state solution for a highly viscous case was found to be almost the same as the mean over an eddy cycle for a lower viscosity case which shed discrete eddies of large amplitude. Eddy shedding and westward spreading of the Loop can be prevented at higher Reynolds numbers when the beta Rossby number, $R_B = v_C / (\beta L_p)^2 > 2$, where the appropriate length scale, L_p , is one-half the port separation distance and v_C is the velocity at the core of the current. Differential rotation (β) is also of

great importance in determining the diameter and westward speed of the eddies and the penetration of the Loop Current into the Gulf. In a few of the two-layer experiments, baroclinic and mixed instabilities were encountered, but experiments dominated by a horizontal shear instability of the internal mode produced the most realistic results. For sufficiently high Reynolds numbers the shear instability occurred in both the barotropic and reduced gravity models. However, for realistic parameter values eddy shedding occurred in the two-layer and reduced gravity models, but not in the barotropic model.

Consistent with potential vorticity conservation dynamics, the Loop Current and its eddy shedding behavior was quite insensitive to the location and width of the inflow and outflow ports, so long as the western boundary did not interfere with the shedding process and the ports were not separated by much less than $1/\sqrt{2}$ times the theoretical eddy diameter, i.e., when $R_B < 2$. When the entire eastern boundary was opened, the outflow remained confined to a current adjacent to the southern boundary. Also, while the solution depends on the maximum velocity at inflow, it is relatively insensitive to the shape of the inflow profile.

In the presence of significant deep-water inflow through the Yucatan Straits, bottom topography may prevent Loop Current penetration, westward spreading, and eddy shedding. In these cases the interaction between the bottom topography and the pressure field near the Florida Shelf results in a near balance between the pressure torques and the nonlinear terms in the mass transport vorticity equation. When the Yucatan Straits deep water inflow is reduced or the Florida Shelf is moved to the east, the eddy shedding reappears. A kinematic analysis shows that a sufficiently strong current following f/h contours of the Florida Shelf and intersecting the Loop Current at large angles can locally prevent northward penetration of the Loop Current and effectively reduce the port separation. Thus, the effect of the Florida Shelf is similar to cases in the reduced gravity model

where the ports are too close for eddy shedding to occur, i.e., when $R_B > 2$. Bottom topography also inhibits development of baroclinic instability, yielding solutions more closely resembling those from the reduced gravity model than from the two-layer flat bottom model. However, movement of the shed eddies is significantly modified by the introduction of topography.

In the presence of realistic time variations in the upper layer inflow, the eddy shedding period is dominated by the natural period rather than the forcing period, although the influence of the latter is not negligible.

1. Introduction

The Gulf of Mexico is remarkable for the variability and intensity of its circulation. The Loop Current in the eastern Gulf is of particular interest since it supplies a significant fraction of the source water for the Gulf Stream - approximately $30 \times 10^6 \text{ m}^3 \text{ sec}^{-1}$ (Nowlin, 1972). Entering the Gulf through the Yucatan Straits, the Loop Current traces an anticyclonic path which may extend far to the north before turning southward and exiting through the Straits of Florida. Large anticyclonic eddies have been observed to break off from the Loop Current following these intrusions (Fig. 1). The eddies typically have diameters of about 360 km and translate into the western Gulf with a mean speed of 2.4 cm sec^{-1} (Elliott, 1979). One hypothesis holds that the persistent anticyclonic gyre in the western Gulf is periodically renewed by these break-off eddies (Cochrane, 1972; Behringer, et al. 1977). This contrasts with the suggestion by Sturges and Blaha (1976) that the western gyre may be driven by wind-stress curl.

Cochrane (1965) proposed that the path for the Loop Current might vary in response to an annual variation in the strength and cross-stream structure of the surface currents in the Yucatan Straits. Leipper (1970), Cochrane (1972), Maul (1977), and others have contributed limited observational evidence for a seasonal cycle in the Loop Current, although each author identified considerable year-to-year variability in the data. Recently, Molinari (1978) has challenged the hypothesis of an annual cycle in the Loop Current:

Circulation patterns in the Gulf given by climatological averages and several synoptic studies suggest an annual cycle for the intrusion of the Loop Current. The Loop intrudes north, in these representations, into the Gulf during late winter and spring, reaches maximum penetration in the Gulf during the summer, sheds an eddy which drifts west during the late summer and fall and exhibits minimum penetration in the winter. A reanalysis of the historical data set suggests that the climatological results are severely biased by the temporal sampling distribution. In fact, large summer-fall intrusions

occurred in 1966, 1969, 1973, and 1974, followed by maximum penetration in the winter, rather than summer.

Glaring inadequacies both in the data-base outside the Loop Current and our knowledge of the dynamics of the circulation in the Gulf are apparent. Circulation patterns in the absence of the Loop or detached eddies are unknown. Thus, the magnitude and region of exchange between the eastern and western Gulf are unknown. Little data (even less current meter data) exist to define the deep circulation. The effect of cold fronts on the circulation, the effect of the boundary conditions at the Yucatan and Florida Straits on the Loop Current, and the effect of the wind on the circulation have yet to be quantified. As basic a question as what drives the western Gulf circulation, detached eddies or curl of the wind stress is still unanswered. The time appears appropriate for the use of simple analytical and/or numerical models to address these questions and to provide the basis for more process oriented observational studies rather than the circulation mapping exercises of the past.

The purpose of this paper is to simulate and understand the dynamics of the Loop Current and its eddy shedding using an ensemble of numerical models, including two-layer, barotropic, and reduced gravity prototypes. A series of important inter-related questions are addressed: Can a simple model simulate the Loop Current and eddy shedding in statistical agreement with the limited observations? Is the eddy shedding rate controlled by internal dynamics or by external changes in boundary conditions? What determines the scale of the shed eddies? What dynamics control the Loop Current penetration and eddy break-off? How does the magnitude and cross-stream profile of the current through the Yucatan Straits affect Loop Current behavior? What happens to the eddies once they are shed? What is the influence of bottom topography on eddy shedding and the Loop Current?

Because of the efficiency of the primitive-equation model formulation, in which free-surface and internal gravity waves are treated implicitly, over 100 model experiments covering a wide range of the parameter space were integrated to statistical equilibrium. Previous studies using a barotropic model (Paskausky and Reid, 1972) and a quasi-geostrophic two-layer model (Wert and Reid, 1972) were extremely limited in the range of parameter space studied and the models were not integrated to statistical equilibrium.

The formulation and parameters of the three models used in this study are presented in section 2. Numerical aspects of model design are discussed in Appendix B, where particular attention is given to the semi-implicit treatment of the gravity waves, to the boundary conditions for the resulting Helmholtz equations, and to the boundary conditions at the open ports. In section 3 we first explore the capability of the numerical models to perform realistic simulations of the Loop Current and the eddy shedding. Using realistic parameters, we determine, which, if any, of the models produce eddies with realistic size, amplitude, and movement and the observed quasi-annual period of eddy shedding.

In section 3b we vary the model parameters to assess the influence of the internal dynamics on the eddy shedding by the Loop Current and on the character of any shed eddies. Regression analysis is used to test a number of dynamical hypotheses based on Rossby wave theory and on conservation of potential vorticity on a β -plane. In section 3c we compare a steady solution with a low Reynolds number to a linear viscous solution and to the mean of a case which exhibited eddy shedding. The regimes found in a barotropic flat bottom model are discussed in section 3d and compared to those of the reduced gravity model, noting the role of the divergence term in the vorticity equation in creating the differences. In section 3e we compare the relative realism of results from cases with horizontal shear instability, baroclinic instability, and mixed stability.

In section 4 we investigate the importance of external influences on the eddy shedding by the Loop Current. In the three subsections we explore the response of the model (a) to changes in the location, width, and separation of the inflow and outflow ports, (b) to the introduction of bottom topography, and (c) to spatial and temporal changes in the inflow transport. In section 4a some of the results for the reduced gravity and barotropic flat bottom models are summarized in a stability regime diagram. In section 4b a kinematic analysis is used in explaining the

important role of the Florida Shelf when there is sufficient deep water inflow through the Yucatan Straits. The influence of the topography on the baroclinic stability of the Loop Current is also considered.

2. The Gulf of Mexico models

Three models are used in this study: two-layer, barotropic, and reduced gravity. The last two are mathematically identical but have differing gravitational accelerations. In the reduced gravity model a value appropriate for the first internal mode is used and the lower layer is assumed infinitely deep and at rest. The barotropic and reduced gravity models demonstrate the individual behavior of the external and internal modes and provide insight into how they interact in the two-layer model. They also allow us to investigate certain phenomena in the simplest context.

The two-layer and reduced gravity models are assumed to be stably stratified and a fixed density contrast is specified between the two immiscible layers. All other thermodynamic effects are neglected. For all three models we assume a hydrostatic, Boussinesq fluid with a free surface in a rotating right-handed coordinate system. Retaining only the first term in the perturbation expansion for the advective terms, the vertically integrated equations of motion used in the

models are

$$\frac{\partial \vec{V}_i}{\partial t} + (\nabla \cdot \vec{V}_i + \vec{V}_i \cdot \nabla) \vec{V}_i + \hat{k} \times f \vec{V}_i = -h_i \nabla P_i + \frac{\vec{\tau}_i - \vec{\tau}_{i+1}}{\rho} + A \nabla^2 \vec{V}_i , \quad (1)$$

$$\frac{\partial h_i}{\partial t} + \nabla \cdot \vec{V}_i = 0 , \quad (2)$$

where $i = 1, 2$ for the two-layer model, $i=1$ for the barotropic and reduced gravity models and

$$\nabla = \frac{\partial}{\partial x} \hat{i} + \frac{\partial}{\partial y} \hat{j} ;$$

$$P_1 = g n_1 ;$$

$$P_2 = P_1 - g' h_1 ;$$

$$\vec{V}_i = h_i \vec{v}_i = h_i (u_i \hat{i} + v_i \hat{j}) .$$

$$g' = \frac{g(\rho_2 - \rho_1)}{\rho},$$

$$f = f_0 + \beta(y - y_0),$$

$$\vec{\tau}_i = \tau_i^x \hat{i} + \tau_i^y \hat{j}.$$

See Appendix A for symbol definitions.

In the reduced gravity model, the lower layer momentum equation degenerates to $\nabla p_2 = 0$, and in the barotropic model $\vec{\tau}_2$ becomes the bottom stress. Laplacian horizontal friction is such a crude representation of sub-grid scale motion that we did not believe it necessary to use the more complicated form which actually results from the derivation of the model equations. However, a number of experiments were performed in which $Ah\nabla^2\vec{v}$ rather than $A\nabla^2\vec{V}$ was used for horizontal friction. Only small quantitative differences were found except in the two-layer model with bottom topography and significant deep water transport. There the regime boundary between steady and eddy shedding regimes was shifted. For further details, see Blake, et al. (1980).

Figure 2 shows the model domain superimposed on a map of the Gulf of Mexico. We use a 1600×900 km rectangular domain, neglecting the 20° counter-clockwise rotation. Thus, the Coriolis parameter, $f=f(y)$ only. We use the β -plane approximation for that variation. The model is driven from rest by inflow through the southern port (Yucatan Straits). This is exactly compensated by outflow through the eastern port (Florida Straits). In most experiments the inflow port is 160 km wide, centered 400 km from the eastern boundary. The outflow port is 150 km wide, centered 75 km from the southern boundary. In a few cases the Florida and Yucatan Straits are explicitly included as extensions to the model domain. Wind forcing is neglected in the experiments described here. This does not imply that we believe wind forcing is unimportant to the Gulf circulation. Rather, we have chosen the Loop Current forcing as the focus of this study. Figure 3 shows the idealized bottom topography of the Gulf used in some experiments.

Except at the inflow and outflow ports, the walls are rigid and the no-slip condition is prescribed on the tangential flow. At inflow the profile of transport, V_i , is prescribed. In most cases this profile is parabolic. Because the current is nearly geostrophic, the upper layer velocity maximum is west of the center of the Yucatan Straits. The normal flow at the eastern port is self-determined with the integral constraint that the total transport out from each layer match the inflow. Usually the amplitude of the tangential component was set to zero one-half grid distance outside the physical domain at both ports. This weak over-specification at outflow eliminates the possibility that the Loop Current will exit the basin at unrealistic angles. More realistically, outflow should occur through a channel modeling the Florida Straits. This was done in a few cases. See Appendix B for further discussion of the design of the semi-implicit numerical models.

The parameters of a "standard" case for each model are given in Table 1. The value of g' is the equivalent for a reduced gravity model. In the two-layer model this value is multiplied by $(H_1+H_2)/H_2$ to yield the same internal values for the gravity wave speed, radius of deformation, and Rossby wave speed as in a reduced gravity model. The inflow transport is spun up with a time constant of 30 days. The only dissipation in the model is due to horizontal friction. Interfacial and bottom stresses were excluded in almost all cases. Two cases were selected in which the potential role of bottom friction was the greatest. These were repeated including quadratic bottom friction and the results are discussed in section 3. Our standard case value for the horizontal eddy viscosity is larger than required for stable integration of the model. This value yielded a constant eddy shedding period for the Loop Current. Smaller values produced some irregularity in this period without substantially altering the long term statistical properties of the eddy shedding process. Although lower eddy viscosities were used in some cases, the larger value was used in most to decrease the length of the integration required to obtain stable statistics and to facilitate the analysis of the results.

Table 1. Model Parameters for Standard Case

A	$10^7 \text{ cm}^2 \text{ sec}^{-1}$	β	$2 \times 10^{-13} \text{ cm}^{-1} \text{ sec}^{-1}$
f_0	$5 \times 10^{-5} \text{ sec}^{-1}$	ρ	1 gm cm^{-3}
g	980 cm sec^{-2}	τ_i	0
g'	3 cm sec^{-2}	Δx	20 km^*
H_1	200 m	Δy	18.75 km^*
H_2	2800 m	Δt	1.5 hr
Domain Size, x_L by y_L			1600 x 900 km
Southern Port Width, L			160 km
Eastern Port Width, L_e			150 km
Center of southern port at x_p			1200 km
Center of eastern port at y_p			75 km
Upper Layer Inflow Transport**			$20 \times 10^6 \text{ m}^3 \text{ sec}^{-1}$ (20 Sv)
Lower Layer Inflow Transport			$10 \times 10^6 \text{ m}^3 \text{ sec}^{-1}$ (10 Sv)
Angle of inflow from x-axis, θ_i			90°
For the barotropic model the initial maximum depth is $H=3000$ m and the inflow transport is 30 Sv.			
* for a given variable			
**also for the standard reduced gravity model			

3. The influence of internal dynamics on eddy shedding by the Loop Current

Our first goal was to simulate the Loop Current and its eddy shedding in a manner which resembles the observed behavior. A nonlinear two-layer hydrodynamic model was chosen as the simplest model likely to succeed. A second active layer allowed the possibility of baroclinic instability and other modal interactions, and allowed inclusion of both an idealized pycnocline and idealized topography of the Gulf.

Once we demonstrated the ability of the model to perform a realistic simulation, we 1) examined the dynamics of the eddy shedding Loop Current in the simplest context, 2) looked for the existence of other regimes within the neighboring parameter space, and 3) examined the effects of topography, time variations in the inflow, and changes in the port configuration. The third area of investigation is discussed in section 4.

a. A simulation of the eddy shedding by the Loop Current

A longstanding hypothesis is that the Loop Current sheds eddies in response to quasi-annual variations in the vorticity and the inertial character of the current through the Yucatan Straits. These variations in the total transport, or the horizontal and vertical structure presumably affect the penetration distance of the Loop Current. When the current retreats, an eddy is left behind. Despite the popularity of this idea, we first searched for purely internal mechanisms where the eddy shedding results from unstable configurations of the Loop Current, independent of any finite amplitude perturbation due to time variations in the inflow.

Instead of starting with the simplest possible model and progressing toward more complicated experiments, we designed our first experiment to be as realistic as possible within the context of the two-layer model and a time invariant inflow profile for \vec{V} . We then looked for the simplest model which produced essentially

the same results. The parameters for the first numerical experiment using the two-layer model are listed in Table 1, except that the upper layer inflow transport is 25 Sv, and the lower layer 5 Sv. The idealized topography for the Gulf of Mexico shown in Figure 3 is also included. The inflow transport is steady except for spin-up with a time constant of 30 days.

Figure 4 shows a sequence of snapshots of the pycnocline anomaly at 70-day intervals. The pycnocline anomaly is the deviation of the interface from the initial horizontal surface. Downward deviations are positive (upper layer thickness greater than initial). Figure 4a shows the Loop Current already penetrating far into the Gulf and beginning to develop an eddy structure. Figure 4b shows an eddy starting to break off from the loop. Figure 4c shows the Loop Current and eddy just after separation. At this stage the Loop Current is a source-sink flow with less penetration into the Gulf. Figure 4d shows the eddy has moved westward and the Loop Current has penetrated further into the Gulf. Returning to Figures 4a and 4b, we see that when an eddy reaches the western boundary, it moves northward with final decay in the northwestern part of the basin. Figure 5a shows the pycnocline as a function of time at the longitude $x = 1010$ km from the western boundary.

Even though the inflow profile for \vec{V} is steady, the eddy shedding occurs in a regular manner with a period of 290 days. This period compares favorably with the quasi-annual period observed. Furthermore, when parameters suitable for the Gulf of Mexico are used, the size, amplitude, and movement of the eddies are also consistent with observations (Nowlin, 1972; Cochrane, 1972; Elliott, 1979). Of particular interest is the realistic value for the eddy shedding period predicted by the model with no time variation in the inflow, since the popular hypothesis is that the Loop Current exhibits a quasi-annual shedding period in response to the seasonal variations in the inflow through the Yucatan Straits.

Thus far, we have shown that the model can realistically simulate observed features of the eddy shedding by the Loop Current when model parameters realistic for the Gulf of Mexico are used. In addition, we have shown that time variations in the inflow are not required for the eddy shedding to occur at a realistic rate.

b. Dynamics of the eddy shedding by the Loop Current

At this point we want to examine the dynamics of the eddy shedding by the Loop Current in the simplest context. Figure 5 shows the pycnocline anomaly vs. time at a longitude 190 km west of the center of the inflow port for three different cases. Figure 5a is for the case with bottom topography already described. Figure 5b is for a two-layer flat bottom case using the parameters given in Table 1. Figure 5c is for a reduced gravity experiment using the same parameters, except that the lower layer is infinitely deep and at rest. Most striking is that all three experiments produce nearly the same results in terms of eddy shedding period, eddy diameter, and eddy amplitude, within 20% or less in almost all respects. In all three, discrete eddies are shed in a regular manner with little evidence of other oscillations. The most notable difference is that the case with the bottom topography of Figure 3 did not begin to shed eddies for almost three years. The barotropic model evolved to a steady state without shedding eddies in this

parameter range with 30 Sv inflow and 3000 m depth (see Section 4, Fig. 23a).

The ability of the reduced gravity model to produce essentially the same results as the two-layer model is sufficient to demonstrate that the discrete eddy shedding regime found in these three cases is not due to baroclinic instability, but instead is due to a horizontal shear instability of the internal mode. The reduced gravity, two-layer flat bottom, and two-layer model with idealized Gulf of Mexico topography do not agree in all the dynamical regimes we found, as we shall see later. However, they do agree for a regime in accord with observed features of the Loop Current-eddy system. This suggests that the simplest useful model to study the dynamics of the eddy shedding from the Loop Current is the reduced gravity model.

Before turning to the reduced gravity model, we will demonstrate the importance of differential rotation (β) to the eddy shedding. Figure 6 shows the free surface anomaly at day 1080 for an f-plane case using the two-layer flat bottom model with the parameters of Table 1, except that $\beta=0$ and the inflow angle is 27° west of normal. Even with the westward inflow component, the solution evolved to the steady state source-sink flow shown in Figure 6 without shedding an eddy. The experiment was continued after adding a time varying inflow with an annual signal much larger than observed (total inflow transport ranging from 20 to 40 Sv). Still no eddy shedding occurred. With a sufficiently high Reynolds number, no doubt some physical instability would occur. However, it is clear that β plays an essential role in the discrete eddy shedding regime shown in Figures 4 and 5.

A large number of numerical experiments were conducted using the reduced gravity model. All of those with a steady inflow, time invariant values of other specified parameters, and port geometry not grossly different from the Gulf of Mexico are listed in Table 2. Barotropic flat-bottom cases are also included. Fortunately, we were able to perform enough reduced gravity experiments to test a

Table 2 - Reduced Gravity (RG) and Barotropic Flat Bottom (BT) Model Experiments

Case	Differences from Table 1	d_m	y_e	b_m	P_m	c_m	v_{in}	v_{mx}	h_e	h_m	h_a	Re	R_B	Notes
Reduced gravity experiments														
RG1	standard	373	364	574	327	3.21	72.9	74.0	250	353	180	58.3	.88	
RG2	$\beta=0$	-	67	209	N	-	72.6	-	-	323	160	58.1	∞	
RG3	$\beta=1$	502	475	745	784	2.00	75.1	71.2	253	373	210	60.1	1.81	
RG4	$\beta=4$	272	261	414	152	5.98	70.4	71.1	250	336	165	56.3	.42	
RG5	$\beta=8$	164	185	292	79	9.97	67.8	44.6	242	283	90	54.2	.20	
RG6	$f_0=2$	323	352	505	132	12.07	82.1	81.7	242	286	105	65.7	.99	
RG7	$f_0=3.65$	354	369	556	218	5.17	76.7	74.6	248	322	150	61.4	.93	
RG8	$A = 3$	367	351	526	366	3.91	72.9	89.1	282	395	210	194.4	.88	1
RG9	$A = 6$	367	364	551	344	3.42	72.8	79.8	266	371	200	97.1	.88	2
RG10	$A = 12$	367	358	570	318	3.20	72.7	70.4	250	344	175	48.5	.88	
RG11	$A = 30$	288	296	518	W	-	73.5	29.5	212	248	97	19.6	.89	
RG12	$L=80$, 10 Sv, $x_p=1160$, $y_p=112$	304	297	479	277	3.47	76.1	60.8	238	304	120	30.4	.74	
RG13	$L=80$, 10 Sv, $x_p=1240$, $y_p=37.5$	298	292	472	276	3.55	76.2	59.7	237	302	120	30.5	1.16	
RG14	$L=120$, 15 Sv, $x_p=1180$, $y_p=56$	340	337	533	306	3.45	75.6	70.5	247	333	160	45.4	.84	
RG15	$L=240$, 30 Sv, $x_p=1140$, $y_p=112$	415	398	616	346	3.21	69.3	72.0	256	378	230	83.2	.62	
RG16	.1 Sv	169	122	244	W	-	.5	.2	200	200	.4	.4	.006	
RG17	1 Sv	175	131	250	W	-	4.5	1.3	201	202	4.0	3.6	.054	
RG18	10 Sv	246	254	421	294	3.55	39.9	26.1	220	247	55	31.9	.48	
RG19	15 Sv	316	315	500	304	3.28	57.1	53.4	240	305	125	45.7	.69	
RG20	25 Sv	407	397	619	360	3.29	87.4	90.2	264	398	260	69.9	1.06	

Table 2 cont.

Case	Differences from Table 1	d_m	y_e	b_m	p_m	c_m	v_{in}	v_{mxe}	h_e	h_m	h_a	Re	R_B	Notes
RG21	30 Sv	452	404	640	428	3.74	101.8	102.2	285	456	325	81.4	1.23	
RG22	30 Sv, $x_L=1760$, $y_L=1200$	441	418	646	357	3.60	98.6	101.3	286	450	315	78.9	.63	
RG23	30 Sv, $y_L=1200$	434	398	627	394	3.84	98.6	98.6	290	453	320	78.9	1.19	
RG24	$y_L=1200$	363	359	561	320	3.34	71.4	71.6	256	354	180	57.1	.86	
RG25	$x_L=2000$, $x_p=1600$	375	351	556	339	3.63	72.7	75.1	248	358	190	58.2	.88	
RG26	$x_L=2000$	367	361	566	335	3.32	72.0	71.7	255	355	180	57.6	.22	
RG27	$\Delta x=10$ km, $\Delta y=9.375$ km	380	369	589	329	3.18	74.4	72.3	246	347	180	59.5	.90	
RG28	free slip boundaries	367	367	577	343	3.22	73.0	74.9	250	349	185	58.4	.88	
RG29	$A\hat{h}\nabla^2\vec{V}$ replaced $A\nabla^2\vec{V}$	336	348	531	333	3.54	72.8	74.8	265	364	185	58.2	.88	
RG30	$L_e=75$, $y_p=37.5$	370	364	571	328	3.20	72.9	73.6	252	351	180	58.3	.90	
RG31	Fla. Straits added to domain	375	362	574	327	3.21	73.0	74.6	248	353	185	58.4	.88	
RG32	D_l , $L_e=160$, $y_p=80$, $\theta_i=102.1^\circ$	384	373	580	316	3.16	69.0	83.9	247	366	195	55.2	.83	
RG33	D_l , $L_e=80$, $y_p=40$, $\theta_i=101.4^\circ$	372	368	570	323	3.21	68.6	81.4	249	362	190	54.9	.85	
RG34	D_l , $L_e=320$, $y_p=160$, $\theta_i=102.0^\circ$	387	376	582	313	3.16	69.1	84.3	246	367	195	55.3	.82	
RG35	$x_p=1000$, $y_p=225$	373	360	570	325	3.29	72.9	69.4	254	355	185	58.3	.35	
RG36	$L=80$, 10 Sv, $x_p=960$, $y_p=225$	284	295	476	302	3.35	77.1	56.6	240	298	120	30.8	.34	
RG37	Yucatan Peninsula in Fig. 22	341	472	653	430	3.20	71.3	69.8	251	344	210	57.0	.86	
RG38	uniform inflow profile for V	348	328	536	308	3.26	63.0	53.2	237	305	125	50.4	.76	
RG39	$\theta_i = 116.6^\circ$	403	312	535	284	3.16	77.8	85.6	246	368	200	62.2	.94	
RG40	D2	-	55	219	N	-	71.1	-	-	329	130	56.9	2.02	

Table 2 cont.

Case	Differences from Table 1	d_m	y_e	b_m	P_m	c_m	v_{in}	v_{mxe}	h_e	h_m	h_a	Re	R_B	Notes
RG41	D2, $A = 3$	-	60	209	N	-	71.3	-	-	334	145	190.1	2.03	
RG42	D2, $A = 30$	-	30	270	N	-	72.5	-	-	322	135	19.3	2.06	
RG43	D2, 10 Sv	234	252	418	301	3.57	40.0	22.1	215	238	40	32.0	1.14	
RG44	$L_e = y_L, x_L = 1760$	389	369	585	308	3.23	73.5	77.1	246	357	190	58.8	0.00	3
RG45	$L_e = y_L, x_L = 2000$	366	358	567	341	3.34	72.0	72.2	252	350	180	57.6	0.00	3
RG46	$L_e = y_L, L = 80, 10 \text{ Sv}, x_p = 1160$	293	295	473	270	3.63	76.3	59.2	236	299	120	30.5	0.00	3
RG47	D2, $A = 50, 17.7 \text{ Sv}$	-	0	188	N	-	65.5	-	-	309	120	10.5	1.86	
RG48	D2, 10 Sv, $H_1 = 3000 \text{ m}$	175	126	242	W	-	3.0	1.0	201	201	2.5	2.4	.087	
RG49	$A = 30, 4.2 \text{ Sv}, x_p = 1500$	-	0	65	N	-	18.0	-	-	230	30	4.8	2.30	
RG50	$A = 3, 1 \text{ Sv}, \text{free slip b.c.}$	163	104	188	W	-	4.5	1.7	201	202	3.7	12.0	.054	
Barotropic flat bottom experiments														
BT1	standard	182	146	262	W	-	9.2	3.0	H	1	3	7.3	.11	
BT2	$H = 200 \text{ m}, 10 \text{ Sv}$	212	271	439	W	-	45.7	16.9	H	8	17	36.6	.55	
BT3	$H = 300 \text{ m}, 20 \text{ Sv}$	211	290	461	71	10.52	60.9	37.9	H	18	18	48.7	.74	
BT4	$H = 300 \text{ m}, 25 \text{ Sv}$	235	323	464	52	*	76.1	64.1	H	34	52	60.9	.92	4
BT5	$H = 300 \text{ m}$	264	358	485	51	*	91.5	86.2	H	52	70	73.2	1.10	4
BT6	$H = 300 \text{ m}, 45 \text{ Sv}$	385	420	574	95	*	137.2	164.3	301	122	150	109.8	1.66	4
BT7	$\beta = 0, H = 300 \text{ m}$	-	66	197	n	-	91.4	-	-	50	60	73.1	∞	
BT8	D2, 300 Sv	-	54	173	n	-	91.5	-	-	50	52	73.2	2.61	

Symbol Definitions for Table 2

- N,n Stable regime for the reduced gravity model (N) and the barotropic model (n) in which there was no westward spreading of the Loop Current and no eddy shedding.
- W,w Stable regime for the reduced gravity model (W) and the barotropic model (w) in which there was westward spreading of the Loop Current, but no eddy shedding.
- d_m North-south diameter in km of an eddy measured between speed maxima as the center passed 110 km west of the western boundary of the inflow port. For regime W,w all quantities were calculated treating the loop as we would an eddy.
- y_e Distance from the southern boundary in km of the eddy pressure centers as they passed a longitude 10 km west of the western boundary of the inflow port. In regime N,n quantities were calculated at whatever longitude the extreme value occurred.
- b_m Distance from the southern boundary in km of the northern speed maximum as the center of an eddy passed 110 km west of the western boundary of the inflow port.
- p_m Eddy shedding period in days. In the stable cases the type of stable regime is listed.
- c_m Average westward speed in cm/sec of an eddy between 110 km and 310 km west of the western boundary of the inflow port. In cases marked by an asterisk (*) this was not clearly defined due to interaction with other eddies.
- v_{in} Maximum current speed at inflow in cm/sec.

- v_{mxe} Maximum current speed in cm/sec 110 km west of the western boundary of the inflow port as an eddy passed through that longitude.
- h_e Representative depth in m of the interface in an eddy as the center passed 110 km west of the western boundary of the inflow port. This was taken as the mean of the values at the northern and southern speed maxima.
- h_m Maximum depth in m of the interface in an eddy as the center passed a longitude 110 km west of the western boundary of the inflow port. In the barotropic cases it is the maximum FSA in cm.
- h_a Amplitude in m of the eddy pycnocline deformation as the eddy center passed 10 km west of the western boundary of the inflow port. This was measured relative to the ambient value of the pycnocline anomaly surrounding an eddy and is not necessarily the same as the maximum pycnocline anomaly in an eddy. In the barotropic cases we used FSA in cm.
- Re Reynolds number, $v_{in}L_h/A$ where L_h is half the width of the southern (inflow) port.
- R_B Beta Rossby number, $v_{in}/(\beta L_p^2)$ where L_p is half the distance between the centers of the ports. When the entire eastern boundary is open, $L_p = \infty$. In cases marked by D2 an eastern port centered 75 km south of the western boundary of the inserted land mass was used (Fig. 17).

The values in this table were measured to within 3% or better, except for h_a which was only determined within about 10%.

Additional information on differences from Table 1

Units: A in $10^6 \text{ cm}^2 \text{ sec}^{-1}$, β in $10^{-13} \text{ cm}^{-1} \text{ sec}^{-1}$, f_o in 10^{-5} sec^{-1} , inflow in Sv, L , L_e , x_L , y_L , x_p , y_p in km

$L_e = .9375L$ unless explicitly given

- D1 The Yucatan and Florida Straits were added to the model domain (Fig. 20). In these cases the value of θ_i measured from the x-axis is an average over an eddy cycle at the entrance to the Gulf; v_{in} is also measured at the entrance to the Gulf. At the entrance to the Yucatan Straits, the inflow was in the y-direction.
- D2 A land area was inserted to match the location of the Florida Shelf (Fig. 17).

Notes on results in Table 2

- 1 Irregular eddy shedding period: 322-438 days, std. dev. = 37 days; std dev for d_m = 5 km, for b_m = 13 km. Values in the table are means for the last 12 eddy cycles in a 15-yr integration. The range of eddy periods is similar to that observed (Behringer, et al., 1977).
- 2 Irregular eddy shedding period: 328-352 days, std dev = 8 days. The value in the table is the mean over the last 5 eddy cycles in a 7-year integration.
- 3 These experiments did not reach statistical equilibrium within the 5 to 10 year integrations (see section 4a). Values in the table are for the 5th eddy or eddy cycle. Significant rates of change are given in percent per eddy cycle for each case:
 - RG44: -.8 for d_m , -.3 for b_m , 2.5 for p_m ,
 - RG45: -3 for d_m , -2 for b_m , 4.5 for p_m , 1.5 for c_m ,
-3 for v_{mxe} , -1.5 for y_e ,
 - RG46: -.6 for d_m , 2.7 for p_m , -1 for c_m , -.4 for y_e
- 4 Some values may not be representative due to the distortion of the eddies as they interacted with the strong secondary circulation.

number of dynamical hypotheses using regression analysis. In all cases sufficient data is included in the tables to repeat the analysis. Of the cases listed in Table 2, 35 were used in the regression analyses. Only the Yucatan Peninsula case, the cases with the entire eastern boundary open, the stable cases, and the barotropic cases were excluded, unless otherwise noted.

Once an eddy is shed, it is observed to move westward. Using data from the tables, we found that the linear correlation between the westward component of the eddy movement and the non-dispersive internal Rossby wave speed, $c_{inr} = \beta g' h_1 / f^2$, is 0.991. However, averaged over the 35 cases used, this theoretical speed is 40% greater than observed in the numerical model, when h_e from Table 2 is used for h_1 . Including the dispersive contribution to the phase speed reduced this difference to <7%, but degraded the correlation, although it was still ≥ 0.90. Using h_e from Table 2 yielded better agreement than using the mean thickness of the upper layer or the maximum thickness at the center of the eddy, indicating some nonlinear contribution to the westward speed of the isolated eddies. McWilliams and Flierl (1979) discuss the propagation and dynamics of isolated eddies in a variety of situations, most more nonlinear than evolved in this study.

Reid (1972) presents an argument based on conservation of potential vorticity on a β -plane to estimate the penetration of the Loop Current into the Gulf of Mexico. We have found an extension of that argument and its application to be useful in understanding a number of dynamical aspects of the numerical solutions.

In a frictionless, steady state, reduced gravity model

$$\frac{\zeta_1 + f}{h_1} = \text{constant} \quad (4)$$

along a streamline, where ζ_1 is the relative vorticity in the active layer. If we assume the flow is geostrophically balanced, then contours of h_1 are streamlines, and with the β -plane approximation (4) becomes

$$\zeta_1 + \beta y = \zeta_0 , \quad (5)$$

where we have set $y_0 = 0$ and ζ_0 is the relative vorticity when $y = 0$. Writing ζ in natural coordinates and neglecting variations in radius of curvature

$$\zeta_1 = v_c \frac{d\theta}{ds} \quad (6)$$

at the core of the current where there is no contribution from shear, where v_c is the speed at the core of the current, ds is an element of arc length positive in a clockwise direction, and θ is the angle between the velocity vector and the positive x-axis. Noting $\frac{dy}{ds} = \sin \theta$, (5) becomes

$$\sin \theta \frac{d\theta}{dy} = - \frac{\beta}{v_c} y + \frac{v_{co}}{v_c} \sin \theta_0 \frac{d\theta}{dy} \Big|_{y=0} . \quad (7)$$

To facilitate integration of (7), we assume $v_c = \text{constant}$ along the streamline of the core to get

$$\cos \theta = \cos \theta_0 + \frac{\beta}{2v_c} y^2 - y \sin \theta_0 \frac{d\theta}{dy} \Big|_{y=0} . \quad (8)$$

This neglects the point that $v_c \neq \text{constant}$ along a streamline, if there are variations in radius of curvature. Blake (1980) has demonstrated the validity of (8) under less restrictive assumptions.

We can estimate the north-south diameter of an eddy measured between speed maxima, if we take $\theta_0 = \pi$ at the southernmost extent (the origin) and $\theta = 0$ at the northernmost extent. Shortly before an eddy breaks off from the Loop Current, the

flow is approximately westward at the inflection point between the cyclonic flow near the inflow port and the anti-cyclonic flow of the forming eddy. For an infinite radius of curvature at the origin (8) becomes

$$d = 2r = 2(v_c/\beta)^{1/2} , \quad (9)$$

where d is the desired diameter and r is the radius. This is consistent with a scale for beta kossby number, $R_B = v_c/(Br^2) = 1$. The penetration of the current into the basin can be estimated from (8) by setting $\theta = 0$ at the northernmost extent. This yields

$$b = \frac{r^2}{r_0} + \left[\frac{r^4}{r_0^2} + 2r^2(1 - \cos \theta_0) \right]^{1/2} , \quad (10)$$

where b is the northernmost penetration of the core of the current measured from the point of origin, and r_0 is the radius of curvature of the current at the point of the origin. The numerical model verifies the usefulness of the results from this crude analysis.

We tested the validity of (9) as an estimate of the north-south diameter of the eddies measured between the speed maxima. Averaged over 35 cases, (9) overestimated the diameter by 6%, when the maximum speed at inflow, v_{in} , was used to estimate v_c . The eddy diameter, d_m , was measured as the eddy center passed a longitude 110 km west of the western boundary of the inflow port. In most cases the error was <5%. In the cases with low Reynolds number (see Table 2) or at very low latitudes, (9) overestimated the diameter by more than 10%. The linear correlation between the eddy diameters predicted by (9) and by the numerical model was 0.87.

We did not attempt a direct verification of (10). Instead, we performed a simpler test using a regression equation of the form

$$b = A_0 + A_1 d , \quad (11)$$

where A_0 and A_1 are regression coefficients. This is an appropriate regression equation for (10), if all cases use the same origin, and at the origin θ_0 is the same for every case, and $r_0 = \infty$. Omitting the case with inflow 27° west of normal, this regression equation was tested using values of d_m and b_m from 34 numerical solutions. The linear correlation between the penetration distance and the eddy diameter was 0.986, and the average error of the regression fit was 2%. The values for the regression coefficients were $A_0 = 108.4$ km and $A_1 = 1.232$. Note only 1/5 of the total penetration is given by A_0 and $A_1 > 1$. When (9) and the maximum speed at inflow, v_{in} , were used to estimate d for use in (11), the linear correlation was 0.89, and the average error of fit was 5%. The values for the regression coefficients became $A_0 = 88.6$ km and $A_1 = 1.211$. This analysis clearly demonstrates the importance of differential rotation in determining the diameter of the eddies, and the penetration of the model Loop Current into the Gulf.

One of the most intriguing aspects of the eddy shedding by the Loop Current is the prediction of the eddy shedding period. We have found that when parameters realistic for the Gulf of Mexico are used, the eddy shedding period predicted by the numerical model is close to the quasi-annual period observed, even though no time variations in the prescribed inflow profile for \vec{V} were included. Thus, we must ascribe the eddy shedding to some instability inherent in the internal dynamics of the system, and we might describe the eddy shedding period as the period of the instability. However, the Loop Current does not necessarily meet any instability criterion during most of the period between the shedding of eddies. That is, the eddy shedding period is not determined by the growth rate of the horizontal shear instability, but by the time required for the Loop Current to move into an unstable configuration, as it first penetrates into the Gulf and then bends westward. When it finally bends into an unstable configuration and an eddy is about to break off, contours of growth rate for the instability are crossed so rapidly that the growth of the instability itself contributes little to the total

eddy shedding period. This is a picture of a spin-up process which eventually becomes unstable. The spin-up is reinitiated after the break-off of each eddy. This spin-up is not inherently unstable when dissipation is included, as will be shown in the next sub-section. In some regions of parameter space the northward penetration and westward bending proceed to a steady state, and no eddy shedding occurs.

The northward penetration and westward bending can be illustrated by considering internal Rossby wave dynamics and Reid's argument in the form of a quasi-isostatic adjustment process. For geostrophic divergence, the continuity equation, (2), for the reduced gravity model becomes

$$\frac{\partial h}{\partial t} - \frac{\beta V}{f} = \frac{\partial h}{\partial t} - c_{inr} \frac{\partial h}{\partial x} = 0 , \quad (12)$$

where c_{inr} is the non-dispersive internal Rossby wave speed. This illustrates the role of internal Rossby wave dynamics in the westward spreading of the Loop Current. We have already demonstrated the high, 0.991, linear correlation between the westward movement of free eddies in the numerical model and the non-dispersive internal Rossby wave speed. The maximum rate of pycnocline deepening on the west side of the Loop implied by (12) is about 5 m/day for our standard reduced gravity case. Now pick the first inflection point on the stream after inflow on each of the panels in Figure 4. Measured from this point, b from (10) reduces to

$$b = \left(2 \frac{v_c}{\beta} (1 - \cos \theta_0) \right)^{1/2} . \quad (13)$$

In Figure 4 we note the inflection point moves only slightly northward during the northward penetration and subsequent westward bending of the Loop Current. During this process the current at the inflection point rotates counterclockwise due to the influence of internal Rossby wave dynamics on the loop, starting from a nearly northward direction, $\theta_0 = \pi/2$. As θ_0 increases from $\pi/2$ to π , b increases most rapidly at first. Later the westward bending increases more rapidly. Hence, purely from a

consideration of Reid's argument and the influence of internal Rossby wave dynamics, we have a picture of the Loop Current first primarily penetrating into the basin and later primarily bending westward. This is not an inherently unstable evolution as we will illustrate below, and again in the next subsection. Also, without the Rossby wave influence the current can assume a steady source-sink configuration with no westward spreading such as shown in Figure 6.

Figure 7 shows what happens when β is turned off just before the Loop Current is about to shed an eddy. In Figure 7 β was reduced to zero with a time constant of 10 days starting at day 1300 for the standard reduced gravity case depicted in Figure 5c. Figure 7 shows the westward spreading is halted and the eddy shedding process appears frozen. When β is reduced to zero starting 20 days later at day 1320 (results not shown), the eddy shedding is completed as the source-sink portion of the current retreats eastward toward the steady state configuration. The eddy which separates remains almost stationary. Even apart from the westward spreading, β is not neutral in the instability process, since it influences the curvature of the flow. In barotropic instability theory for a mean zonal flow β is commonly a stabilizing factor. In our case it is clearly a destabilizing factor in regions where it tends to increase the magnitude of the flow curvature.

At this point we will test the hypothesis that the eddy shedding period is a small multiple of the time required for an eddy to move an eddy diameter. This multiple depends on the inflow angle of the current. From the previous analysis these are clearly important factors determining the time required for the Loop Current to bend into an unstable configuration. We will test this hypothesis using a regression equation of the form

$$p_e = A_0 + A_1 d (1 + \cos \theta_0)^{1/2} / c_e \quad (14)$$

where p_e is the period of the eddy shedding, θ_0 is the angle of the inflow with the positive x-axis, and c_e is the speed with which an eddy moves westward after separation from the Loop Current. In the first test, values observed directly in the numerical solutions, d_m and c_m , were used for d and c_e . The linear correlation between the eddy shedding periods observed in the numerical solutions, p_m , and the predictor in (14) is 0.95. The average fit error is 8%, and the regression coefficients are $A_0 = 45.1$ days and $A_1 = 2.336$. Only 14% of the period is left to the constant A_0 .

The regression equation (14) was tested a second time using theoretical values for d and c_e . The values of d were obtained from (9) using v_{in} to estimate v_c . The non-dispersive internal Rossby wave speed, c_{inr} , was used for c_e . The linear correlation between predictor and predictand is 0.96 with an average fit error of 7%. The regression coefficients are $A_0 = 56.8$ days and $A_1 = 2.906$. Only 1/6 of the eddy shedding period is predicted by the constant, A_0 . Of the 35 cases, 26 had fit errors less than the mean percentage error. The low viscosity case with $A=3 \times 10^6 \text{ cm}^2\text{sec}^{-1}$, the 30 Sv case with standard basin size, and two of the narrow, 80 km, inflow port width cases exhibited by far the largest fit errors, between 62 and 72 days. The predicted period was too short for the two former, too long for the two latter.

Examination of Table 2 shows that the role of friction should be considered. The striking result is that as the Reynolds number is increased, so is the eddy shedding period. Four cases show the period increasing inversely with the eddy viscosity, and six show the period increasing directly with the inflow port width. Some insight into this perhaps counter-intuitive result can be gained by considering some simple frictional modifications to the previous inviscid arguments. We used the maximum velocity at inflow when using (9) to estimate d . Downstream the speed at the core of the current may decrease due to diffusion, or

entrainment may occur. In the higher Reynolds number cases important secondary circulations occur. These are not necessarily in phase with the eddy shedding, and may account for the irregular eddy shedding period that occurred when we set $A = 3 \times 10^6 \text{ cm}^2 \text{ sec}^{-1}$. As modifications to the previous inviscid analysis, these ideas are consistent with frictional modifications of the eddy shedding period observed in Table 2.

We have performed regression analyses using various measures of frictional effects as predictors. For example, a diffusion time scale for Laplacian friction can be written as L^2/A . We used the inflow port width for the length scale, L. This was first used in a regression equation of the form

$$p_e = A_0 + A_1 L^2/A \quad (15)$$

When all 35 cases were used, the linear correlation between p_e and L^2/A was only 0.13, and the average fit error was 24%. When the data was stratified to remove cases where β , f_0 , v_{in} , or inflow angle differed significantly from the standard case, the correlation for the 21 remaining cases was 0.82. The average fit error was 3%. However, the range of periods was very limited, only 90 days.

Finally, a test was conducted using a multiple regression equation of the form

$$p_e = A_0 + A_1 d (1 + \cos \theta_0)^{1/2}/c_e + A_2 L^2/A \quad (16)$$

Although frictional effects could be included in the multiple regression analysis in a number of ways, we will discuss only this simple one. When d is calculated from (9) using v_{in} for v_c and c_{inr} is used for c_e , the partial correlation for the first predictor is 0.962, for the second, 0.129. The multiple correlation is 0.978 and the average fit error is 6%. The regression coefficients are $A_0 = 17.2$ days, $A_1 = 2.932$, and $A_2 = 0.121$. Only 5% of the eddy shedding period is contained in

the constant A_0 .

A wide variety of cases have been used in the regression analyses. Some of the changes should not affect the eddy diameter or the eddy shedding period, according to the hypotheses we have tested. We repeated the standard case with double grid resolution ($\Delta x = 10$ km, $\Delta y = 9.375$ km for each dependent variable). Table 2, Case RG27 shows the solution was little affected. Changing the formulation for friction from $A\nabla^2\vec{V}$ to $Ah\nabla^2\vec{v}$ in the standard reduced gravity case had only minor effects, the most notable being a 10% reduction in the eddy diameter, d_m . Adding the Florida Straits to the model domain had virtually no effect, vindicating our usual treatment of the eastern port. Changing from no slip to free slip boundary conditions also had little effect on the eddies or the eddy shedding except in the northwest portion of the basin, where the eddies in the no slip case experienced their final decay. In the free slip case the eddies decayed more slowly in that region and formed northward and eastward boundary currents in the northwest part of the basin. In another case we changed the shape of the prescribed inflow profile for V from our usual parabolic shape to uniform across the port. This case fit well with the hypotheses we have tested, suggesting that the maximum velocity at inflow is of primary importance, not the shape nor vorticity distribution of the inflow profile.

By far the largest fit error in the multiple regression analysis, (16), was the 73 day under-prediction for the 30 Sv inflow case with the standard sized basin (Table 2, Case RG21) when v_{in} was used for v_c in (9) and c_{inr} for c_e . Extending the basin 300 km northward reduced the under-prediction to 50 days, the second largest error. Extending the basin 300 km northward and 160 km eastward reduced the fit error to 5 days. Such extensions to the basin had only minor effect in the standard 20 Sv case (see Table 2, Cases RG24-26). Similar results were obtained when d_m was used for d and c_m was used for c_e in (14), showing the fit errors are not

due to the use of theoretical values in (16). The case with $\beta = 10^{-13} \text{ cm}^{-1} \text{ sec}^{-1}$ exhibited even larger eddies than the 30 Sv cases. However, they were less vigorous and their properties fit well in most of the regression analyses. The effects of different port configurations are discussed in Section 4.

The view of the instability of the eddy shedding Loop Current, presented earlier in this section, is not the only useful one. Figure 8 a, b offers a different picture of the eddy evolution and propagation. Figure 8a shows the mean over 3 eddy cycles for the standard reduced gravity case. This shows that in the mean the model eddies produce a western boundary current in the Gulf with northward flow in the upper ocean. Figure 8b is a snapshot of the deviation from the mean at day 1800. The deviations depict a wavetrain originating northeast of the inflow port and decaying near the western boundary. Note the properties of the positive and negative deviations are quite similar. This suggests that for our nearly circular eddies, the appropriate regression coefficients for (14) are $A_0 = 0$ and $A_1 = 2$, if we use the east-west diameter of the deviations of a particular sign for d and c_m for c_e . This is roughly in accord with the values $A_0 = 45$ days and $A_1 = 2.34$ we obtained using d_m for d . The east-west diameter of the deviations for the standard reduced gravity case is $d_1 \approx 420$ km for the downward (positive) deviations associated with the eddy and $d_2 \approx 505$ km for the upward (negative) deviations between the eddies, compared to 373 km for d_m from Table 2, Case RGl. To check the consistency of our data, the eddy shedding period implied by $p_e = (d_1 + d_2)/c_m$ is 334 days, compared to the 327 days actually measured (Table 2, Case RGl).

c. Stabilization of the Loop Current by reducing the Reynolds number

We have already demonstrated that setting $\beta=0$ has a powerful stabilizing effect on the Loop Current. In section 4 we discuss the important effects of port separation and topography on the stability of the Loop Current. In this subsection we demonstrate a stable regime for the Loop Current obtained by reducing the

Reynolds number, $Re = v_c L_h / A$, where we take v_c as the speed at the core of the current, and L_h as half the port width. We reduced Re in two ways from the standard reduced gravity case, 1) by increasing the eddy viscosity by a factor of 3 to $A = 3 \times 10^7 \text{ cm}^2 \text{ sec}^{-1}$, and 2) by reducing the inflow transport by a factor of 200 to obtain an essentially linear solution. Since the reduced gravity model required only 1½ minutes of computer time per year when $\Delta t = 3$ hours, reducing the transport was a more expedient method of obtaining a linear solution comparable to the standard case than linearizing the numerical model. In the linear case the amplitude of the inflow affects only the amplitude of the solution. Linearity was verified by comparing solutions with inflows of 1 Sv and 0.1 Sv.

The lower panels of Figure 8 show the pycnocline anomaly for (c) the steady state solution obtained with $A = 3 \times 10^7 \text{ cm}^2 \text{ sec}^{-1}$, and (d) the steady state linear solution corresponding to the standard case, obtained by using an inflow transport of 0.1 Sv. The westward spreading due to differential rotation is clearly evident in both cases. Although the westward spreading is a strong destabilizing influence, it does not necessarily lead to an unstable configuration, when dissipation is included. When the simple Laplacian friction is just great enough to prevent the large amplitude discrete eddies we obtained in the standard case, it demonstrates remarkable skill in parameterizing the mean over an eddy cycle (compare Fig. 8a and 8c). In another numerical experiment we initialized from the steady state shown in Figure 8c. We kept $A = 3 \times 10^7 \text{ cm}^2 \text{ sec}^{-1}$, but reduced β to zero with a time constant of 10 days. When we did this, the Loop Current retreated toward a source-sink flow similar to Figure 6. In the process a very weak eddy was left behind.

d. Barotropic flat bottom model results

The barotropic and reduced gravity models are mathematically identical but

have differing gravitational accelerations. The vorticity equation for both models is

$$\zeta_t + NL + f(u_x + v_y) + \beta v = A \nabla^2 \zeta \quad (17)$$

where ζ is the relative vorticity and NL represents the nonlinear terms. In the case of a flat bottom Gulf of Mexico model, both have the same steady state linear solution for the same inflow velocity, except that the amplitude of the barotropic and reduced gravity "h"-anomaly fields is in the ratio of g'/g . The vorticity balance is between planetary vorticity advection (βv), and horizontal diffusion ($A \nabla^2 \zeta$). For the parameters of the standard case given in Table 1, the flat bottom barotropic model evolves to a steady state with a pattern of free surface anomaly contours almost identical to the linear solution shown in Figure 8d, cf. Figure 23a. Some important effects of topography in this case are presented in Section 4.

The flat bottom barotropic model begins to exhibit eddy shedding at Reynolds numbers slightly higher than in the reduced gravity case. Figure 9a shows the steady state solution for the barotropic model with a Reynolds number comparable to a reduced gravity case which was weakly unstable. Increasing the Reynolds number by 1/3 produces the weak eddy shedding regime shown in Figure 9b, with weak eddies superimposed on a mean ridge. The eddies propagate westward along the ridge. The reduced gravity model and the two-layer model (both with a flat bottom and the topography of Figure 3) exhibit similar regimes with a weak horizontal shear instability. However, when we increased the Reynolds number further, the character of the barotropic solutions was somewhat different from the other models. The other models developed discrete eddy shedding with weak secondary circulations (see Figures 4 and 5). Only when the Reynolds number was increased still further did the secondary circulations become important. In the barotropic model we did not find the discrete eddy shedding regime with weak secondary circulations. Instead the secondary circulations became important at Reynolds numbers lower than those at

which the discrete eddy shedding occurred (see Figs. 9c and 9d).

A shorter barotropic eddy shedding period (Table 2) and the preceding discussion demonstrate significant differences between the barotropic flat bottom and reduced gravity models due to the role of horizontal divergence. Its role is unimportant in the former, important in the latter. In the reduced gravity model the radius of the eddies is several times greater than the internal radius of deformation, $(g'h_1)^{1/2}/f \approx 45$ km; in the barotropic case several times less than the barotropic radius of deformation, $(gh)^{1/2}/f \approx 1000$ km for $h = 300$ m as in Figure 9b,c,d. Thus, unlike the reduced gravity model the horizontal divergence in the barotropic model is not approximately geostrophic, and the Rossby wave propagation is dispersive, as opposed to nearly non-dispersive in the reduced gravity case, cf. (12). In the barotropic model a rigid lid would eliminate the horizontal divergence entirely in the flat bottom case, yielding an infinite barotropic radius of deformation and purely dispersive Rossby waves.

The interference of the secondary circulations and the distortion of the eddies prevent us from making satisfactory measurements of c_m , etc. in the barotropic model. This hinders quantitative comparison with the reduced gravity model. However, a qualitative comparison is possible. When we set $\beta = 0$, the solution is stabilized as in the other models, and a source-sink flow similar to Figure 6 develops. Further, as predicted by equations (9) and (10), the diameter of the eddies and their penetration into the Gulf is similar (see Table 2). Since the barotropic Rossby waves are dispersive, the barotropic spin-up is more rapid and the eddy shedding period is shorter, about 50 days for the cases shown in Figures 9c and 9d. The complicated patterns shown in these figures are repeated in detail on this 50-day cycle. The stability regimes for the Loop Current are re-examined in section 4, when the role of port separation is included.

e. Cases of baroclinic or mixed stability

The standard two-layer flat bottom case (Table 1) exhibited regular discrete eddy shedding much like Figure 4 with little sign of other oscillations (Fig. 5b). When the eddy viscosity for this case is reduced by a factor of 3 to $A = 3 \times 10^6 \text{ cm}^2 \text{ sec}^{-1}$, the character of the eddy shedding is markedly altered. Figure 10 shows a sequence of six snapshots covering only one quarter of an eddy shedding cycle. A model representation of the Florida Straits has been added to the basin. This did not significantly affect the results as discussed below. Figure 10a looks much like the standard case, but the rest of the sequence is quite different. Figure 10b shows the eddy, which was about to shed in Figure 10a, becoming severely distorted. In Figure 10c,d it has fractured into two eddies. Figure 10e shows the two eddies coalescing. In Figure 10f they have returned to the form of a single eddy. During the 3/4ths of the eddy cycle not shown, the Loop Current penetrates into the Gulf, bends westward, and begins to form an eddy structure. These phases are much like the standard case, except for a strong undulation of the Loop Current.

Figure 11a shows the kinetic energy for each layer in the rectangular part of the basin as a function of time. Clearly evident are two fairly regular oscillations, one of 380 days, the other of 53 days. The longer one is the eddy shedding cycle. The shorter is associated with an undulation of the Loop Current and the fracturing of the eddies. Because these two cycles are not harmonically related, the details of each eddy cycle are quite different. Figures 11b and 11c show the absence of the high frequency oscillation in the standard two-layer flat bottom case, and in the reduced gravity case with $A = 3 \times 10^6 \text{ cm}^2 \text{ sec}^{-1}$ (Table 2, Case RG8). The latter is the same eddy viscosity used for the case shown in Figures 10 and 11a. Another difference in Figure 11a from the standard case (Fig. 11b) is the periodic large growth of the kinetic

energy in the lower layer, lagging the peaks in the upper layer by about 90° . The time that the two energy curves in Figure 11a coincide corresponds to Figures 10d and 10e, showing the baroclinic to barotropic energy conversion which takes place as the eddies fracture. Based on the results of McWilliams and Flierl (1979), we anticipate that Rossby wave dispersion in the lower layer plays an important catalytic role in the subsequent rapid decrease in the lower layer kinetic energy.

Twice we have repeated the experiment with the energy curves shown in Figure 11a without including the Florida Straits as an extension to the basin, once with and once without bottom friction. In both cases the energy curves matched those shown in Figure 11a in detail for over two years. After that they diverged quantitatively, but not qualitatively. The energy curves for the cases with and without bottom friction agreed in detail for the three year duration of the comparison. The bottom friction was quadratic with a drag coefficient of 1.3×10^{-3} . The other flat bottom experiments we performed should be even less sensitive to bottom friction. We repeated the experiments discussed above, but included the topography of Figure 3 and increased the inflow in the upper layer to 25 Sv. Some short term fluctuations (~ 50 days) remained in the energy curves when there was no bottom friction. These were reduced or eliminated when the bottom friction was added, although they were also removed by increasing the lateral friction.

Comparison with the reduced gravity results for the same eddy viscosity (Fig. 11c, Table 2, Case RG8) suggests that the two-layer case (Figs. 10, 11a) is exhibiting a mixed instability, although it is not clear in this case that a contribution from the horizontal shear instability is necessary to explain the eddy shedding. As discussed in section 3b, it is not needed to explain the Loop Current penetration, westward spreading, or tendency to curve back on itself. The rapid rise in

the lower layer kinetic energy lagging the peak in the upper layer kinetic energy is consistent with results obtained by Holland and Lin (1975) for mid-latitude mesoscale eddies. The period of the high frequency oscillation is also similar.

To help clarify the analysis, we looked for a case with a pure signature of baroclinic instability. Figure 12 shows results for a two-layer flat bottom case with the inflow angled 27° west of normal and confined to the upper layer. The snapshots of pycnocline anomaly 30 days apart (Fig. 12a,b) look much like the weak horizontal shear instability regime. However, the phase plot of pycnocline anomaly versus time at $x = 1010$ km from the western boundary (Fig. 12c) shows the period is much shorter, 58 days. Furthermore, there is little evidence of modulation by a longer time scale, except for the first eddy. The amplitude of the oscillation is much stronger on the westward flowing south side of the loop, consistent with a baroclinic instability; e.g., Philander (1976), Rhines (1977).

Figure 13a shows the kinetic energy in the basin as a function of time in the upper and lower layers. It is very similar to the results obtained for baroclinic instability by Holland and Lin (1975), including the maximum in upper layer kinetic energy near the onset of baroclinic instability followed by a rise in lower layer kinetic energy. The period of the oscillation is also similar. In contrast the corresponding reduced gravity case exhibits discrete eddy shedding similar to Figure 4 with a period of 284 days (Table 2, Case RG39). For comparison the kinetic energy in the basin for the reduced gravity case is plotted as a function of time in Figure 13b. A detailed investigation of eddy energetics in the Gulf of Mexico is in preparation.

Figure 14 shows spectra of the pycnocline anomaly at a particular location in the basin for four different cases, a) the standard two-layer flat bottom case, b) the reduced gravity case with $A = 3 \times 10^6 \text{ cm}^2 \text{ sec}^{-1}$, c) the two-layer flat bottom case with $A = 3 \times 10^6 \text{ cm}^2 \text{ sec}^{-1}$, and d) the two-layer flat bottom case with inflow 27° .

west of normal and confined to the upper layer. Parameters not mentioned have the same values as the standard case (Table 1). Figures 14a,b,c exhibit a major peak in the vicinity of one year corresponding to the discrete eddy shedding cycle found in the standard case. In Figures 14a,b no other major peaks are found, except for harmonics. This occurs despite the irregular shedding period found in the case shown in Figure 14b. The irregular shedding is exhibited by higher energy levels at higher frequencies and a noisier looking spectrum, c. f. Fig. 30a. In contrast Figure 14d exhibits a major peak only at 6 cycles/year. A peak near 6 cycles/year is also found in Figure 14c.

Earlier we noted that the discrete eddy shedding regime associated with the horizontal shear instability most resembles observations. Since baroclinic instability becomes important when we reduce the eddy viscosity in the two-layer flat bottom model, does this negate the value of the reduced gravity results? When baroclinic instability becomes important, the results appear less realistic. This question is re-examined in section 4 when we include the topography shown in Figure 3.

4. External influences on the eddy shedding by the Loop Current

We have shown that several distinct flow regimes can exist in the models' statistically steady state. While experiments dominated by a horizontal shear instability of the internal mode produced the eddy shedding behavior most closely resembling that from the actual Loop Current, baroclinic instability, mixed instabilities, and purely steady flows have also been observed in individual experiments with the three model prototypes. Within the shear instability regime, variation of parameters lead to different periods for eddy shedding. Constant inflow transport and realistic values for the parameters yield an eddy shedding period near annual. This suggests that in the actual Loop Current, regular, quasi-annual, eddy shedding might occur with no significant variations in inflow transport or velocity profile -- the shedding being controlled by internal dynamics within the Gulf. To further examine this hypothesis it is necessary to test the sensitivity of the models to spatial or temporal changes in the boundary conditions and to the inclusion of realistic topography.

In this section we first describe the response of the model to changes in location, width, and separation of the inflow and outflow ports. Results from these experiments and those in section 3 are summarized in a stability regime diagram using appropriate definitions of the Reynolds number and beta Rossby number as the axes. Next, the dynamical influence of the large amplitude topography in the Gulf of Mexico is analyzed. Particular attention is given to the topography of the West Florida Shelf. In the presence of deep water inflow through the Yucatan Straits, we have found that this topography exerts a crucial influence on the Loop Current penetration and subsequent eddy shedding. Finally, we explore the model response to spatial and temporal variations in the inflow transport.

Most experiments in this section utilize the reduced gravity model since it is less costly than the two-layer model, but still reproduces the growth of the Loop

Current and generation of Loop eddies characteristic of the horizontal shear instability regime. Experiments involving bottom topography utilize both the barotropic and two-layer models.

a. Port location, boundary conditions, and irregular coastlines

Section 3 has clearly demonstrated that a simple potential vorticity conservation model of the Loop Current is quite useful for interpreting our results. However, we might anticipate that the flow regime, the eddy shedding period, the diameter of the eddies, the extent of Loop Current penetration into the Gulf, and other features of the model solutions also exhibit some dependence on the width and separation of the ports.

The standard 20 Sv reduced gravity case was repeated with the southern port moved 200 km westward and the eastern port 150 km northward. Figures 5c and 15 compare the standard experiment and the moved port case using a t-y plot of PHA 190 km west of the southern port in each case. In the standard experiment the first eddy passes with maximum amplitude at day 335. Subsequent eddies pass at an interval of 327 days. In the moved ports experiment the first eddy passes with maximum amplitude at day 285 with subsequent eddies shed at virtually the same interval as before (Table 2, Cases RG1 and RG35).

If we account for the phase difference of the first eddy due to spin-up, we obtain a direct comparison of spatial structure for the two experiments as shown in Figure 16. These PHA snapshots taken 50 days apart, but in similar phases of model evolution, dramatically illustrate the insensitivity of the eddy shedding behavior to changes in port location or separation. The eddy diameter, the latitude of northernmost penetration of the Loop Current, and the eddy shedding rate have been affected very little.

If the inflow port is moved still further to the west, eddy shedding occurs in

a manner qualitatively similar to that shown in Figure 16. However, the western boundary begins to interfere with the eddy shedding process and slows the shedding rate. For example, when the inflow port is centered 280 km from the western boundary, the eddy shedding period increases to 390 days. Moving the port still further west leads to multiyear eddy shedding periods. If the two ports are moved as close together as possible, with the southern port moved as far east as possible and the eastern port moved as far south as possible, the flow simply enters from the south and exits immediately to the east. No Loop Current growth or eddy shedding is observed.

In Fig. 17 we effectively reduce the port separation by inserting a land mass. Results from these moved ports experiments demonstrate that if the ports are closer than a certain minimum distance, a steady source-sink regime with no westward spreading replaces the eddy shedding regime. A similar result occurs when we set $\beta=0$ (Fig. 6). Even if the ports are sufficiently separated to allow eddy shedding, results in section 3 show that reducing the Reynolds number sufficiently will prevent the eddy shedding and produce a steady regime with westward spreading of the Loop (Fig. 8c).

To synthesize these diverse model results, it is useful to introduce two nondimensional parameters based on the vorticity equation, (17), and the model results: the Reynolds number, $Re = v_{in}L_h/A$, and the beta Rossby number, $R_B = v_{in}/(\beta L_p^2)$, where v_{in} is the maximum speed of the current on inflow, L_h is half the width of the inflow port, and L_p is half the distance between the centers of the ports. Results from Table 2 for barotropic and reduced gravity experiments have been plotted as a function of Re and R_B in a regime diagram (Fig. 18). The three regimes, eddy shedding (E), steady westward spreading (W), and steady source-sink (N) are indicated by symbols for each experiment. This is not meant to preclude the existence of additional regimes at higher Reynolds numbers where instabilities may occur on scales small compared to the eddies shed

by the Loop Current in these experiments. Each regime is characterized by a distinct range of Re and R_B . The critical beta Rossby number, $R_{BC} \approx 2$ for transition to regime N. For the reduced gravity experiments the critical Reynolds number, $Re_C \approx 25$ for transition from regime W to regime E. For the barotropic cases $Re_C \approx 40$. Although we have not attempted to delineate the regime boundaries in detail, several experiments have exhibited characteristics of two regimes. For example, near the transition from regime E to regime W, all the models exhibited eddy-shedding superimposed on a westward spreading ridge in the free surface (Fig. 9b).

Using (9) from the conservation of potential vorticity analysis in section 3, we can also express R_B as the ratio of the eddy radius, $r = (v_{in}/\beta)^{1/2}$, to the port separation, $2 L_p$. For approximately $r/L_p > \sqrt{2}$, neither westward spreading nor eddy shedding occur. The critical port separation can be expressed as

$$L_{pc} = (v_{in} / \beta R_{BC})^{1/2} = r / (R_{BC})^{1/2} \quad (18)$$

where $R_{BC} \approx 2$ and L_{pc} is half the critical distance between the centers of the ports. In our experiments we have not detected any dependence of R_{BC} on Re or other model parameters, although we would anticipate some dependence on the angle of inflow, the geometry, and the orientation of the basin. The importance of R_B to the stability of the Loop Current has also been noted by T. Sugimoto (personal communication), who found all three regimes in laboratory tank simulations of the Gulf circulation.

Using the regime diagram (Fig. 18), the vorticity equation, (17), and the conservation of potential vorticity analysis in section 3, we can state several general conclusions about the model Loop Current and the eddy shedding. In regime W the flow spreads westward and evolves to a steady state with no eddy shedding. The flow resembles the linear viscous solution (Fig. 8d) where planetary vorticity

advection (βv) balances horizontal friction ($A\nabla^2\zeta$). Weak nonlinearity may be present, causing the westward spreading to occur at a higher latitude than if the flow were linear (Figs. 8c, 9a).

From (17) nonlinearity becomes important in regime E. In the presence of differential rotation, β , and increased conservation of potential vorticity, the Loop Current tends to curve back on itself, cutting off eddies (e.g., Figs. 4, 16). The role of the divergence term, $f(u_x + v_y)$, was discussed in section 3d. Near the transition between regimes W and E weak eddies are superimposed on a mean westward spreading loop (Fig. 9b).

In regime N where $R_B = v_{in}/(\beta L_p^2) > 2$, the nonlinearity, the small port separation or small β , and the tendency of the flow to conserve potential vorticity while in approximate geostrophic balance all act in conjunction to prevent the westward spreading and to limit the northward penetration of the current. The nonlinear terms counter the westward spreading due to planetary vorticity advection, the eastern port fixes the location of the current at outflow, and the tendency to conserve potential vorticity influences the path of the current. For normal inflow with no curvature, (8) predicts no westward spreading and (13) predicts the maximum northward penetration of the Loop Current to be $b = (2 v_c/\beta)^{1/2}$, when it is not constrained by a small port separation. The currents in regime N evolve to a steady state before penetrating that far. These results suggest that the current must penetrate approximately that distance for westward spreading and eddy shedding to occur. Given the constraint of a small port separation, it is evident from sketching alternative paths that paths with substantially greater or lesser penetrations would conform even less well with (8) than that shown in Figure 17. In regime N cases with low Reynolds numbers, the horizontal diffusion would tend to prevent sharp curvature of the current.

Our experiments thus far suggest that, in the reduced gravity model with $Re > 25$,

potential vorticity is so well conserved in the Loop Current that, within limits, port location has little influence on its behavior. To explore this point further, experiments with the reduced gravity model were conducted in which the entire eastern boundary was opened (Table 2, Cases RG44-46). The Loop Current was free to choose any path out of the basin along the eastern boundary. The open eastern boundary conditions were applied as before, this time to the entire eastern side of the model. Figure 19 provides a snapshot and a phase plot of PHA from an experiment with an east-west extent for the model domain of 1760 km. The phase plot should be compared to Figure 5c and the snapshot was chosen to be in a phase of eddy shedding similar to Figure 7a. The Loop Current still exits the basin along the southern boundary at all times. The eddy shedding period is similar to the standard 20 Sv reduced gravity case (Table 2, Cases RGl and RG44), but slowly increases monotonically as the Loop Current spins up a gyre in the eastern Gulf which has the north-south scale of the basin. This spin-up occurs on a time scale long compared to the eddy shedding period.

Based on these results, and recognizing the strong tendency for the Loop Current to conserve potential vorticity, we speculate that the actual Loop Current may have "chosen" its present outflow path from the Gulf of Mexico. Florida at one time was totally submerged and the extensive carbonate seabed (Martin and Case, 1975) may have been eroded by the Loop Current over geological time scales to form the Florida Straits.

Though we have examined the models' sensitivity to changes in port location, it is also important to investigate their sensitivity to changes in details of the inflow and outflow boundary conditions. In this case model response was investigated by moving the specification of the inflow and outflow conditions from immediately adjacent to the basin to positions upstream on inflow and downstream on outflow. Thus, the Yucatan and Florida Straits were added to the domain by the

addition of three rectangular land masses. Figure 20 provides results of this experiment for the standard reduced gravity model and two additional experiments in which the width of the Florida Straits was first halved and then doubled, while the inflow transport remained constant. Figure 20 shows the PHA at day 1080 for all three experiments. Clearly there is little qualitative difference in the eddy size in the three cases and, even after three years, very little phase difference in the eddy shedding cycle. (See Table 2, Cases RG32-34 for additional comparisons).

Intuitively, it seems likely that the domain-averaged kinetic and potential energies would be considerably different for the three different outflow port widths considered. For example, since the transport on outflow must equal that on inflow, a higher flux of kinetic energy on outflow would be expected for the half-width case as compared to the other two. To investigate this further we consider the kinetic energy equations for the reduced gravity model:

$$\frac{\partial}{\partial t} (KE) + \nabla \cdot (\vec{V} KE) + \nabla \cdot (\vec{V} P) - P \nabla \cdot \vec{V} = \rho \vec{V} \cdot \vec{F} \quad (19)$$

$$\frac{\partial}{\partial t} (PE) + P \nabla \cdot \vec{V} = 0 \quad (20)$$

where $P = \rho g'(h-H)$, $KE = \frac{1}{2} \rho h(u^2 + v^2)$ and $PE = \rho g'(h-H)^2$. Here h is the instantaneous layer thickness and H is the mean thickness.

The second term on the left-hand side of (19) represents kinetic energy flux divergence, the third term represents pressure work divergence, and the fourth term represents potential to kinetic energy conversion. The term on the right is the dissipation. Averaging over the rectangular part of the domain, contributions to the kinetic energy flux and pressure work occur only at the ports. Since we have included the straits we are able to calculate flux terms at the ports directly.

Over an eddy cycle, in statistical equilibrium, the tendency terms for the domain averaged kinetic energy and potential energy vanish, as do the potential to

kinetic energy conversion terms. Figure 21 presents box diagrams for the domain-averaged energy for the standard reduced gravity experiment, the half-width outflow experiment, and the double width outflow experiment, respectively. Time averages of each term were taken over exactly one eddy cycle in each case.

For the standard case the rate of pressure working on the inflow and outflow is an order of magnitude larger than the kinetic energy flux on inflow or outflow. The net rate of pressure working on the basin is roughly four times the rate of net kinetic energy flux into the basin. For the half-width outflow experiment the rate of kinetic energy outflow is quadrupled. However, the pressure work term on outflow is only about half the value for the standard case. The net result is that the total kinetic and potential energy for the basin remains almost the same as in the standard case. For the double-width experiment the kinetic and potential energies in the basin are only slightly larger than in the other two cases and the kinetic energy outflow is reduced by about 16 percent from the standard case. While the kinetic energy flux and the rate of doing pressure work at the outflow port may vary markedly among these experiments, the net kinetic and potential energy in the basin varies little.

Before leaving this aspect of model response to external variables we wish to evaluate the influence of a coastline irregularity in the actual Gulf of Mexico, the Yucatan Peninsula. To investigate this external influence we conducted an experiment identical to the standard reduced gravity case but with the Yucatan Peninsula represented as a rectangular block just west of the inflow port. It should be noted in Figure 2 that this geometry actually better represents the Yucatan Shelf than the Yucatan Peninsula. Figure 22 presents a snapshot of PHA for

that case at day 1080 and a phase plot at $x = 1010$ km. While the eddy shedding still occurs, the eddy shedding period for this case is 430 days, 100 days longer than for the standard case. This is due to at least three factors. The first, and apparently most important, is that while the minimum penetration latitude does not change markedly, the maximum latitude of Loop Current penetration is about 100 km greater. This means that in the Yucatan Peninsula case, the Loop Current must undergo greater changes in its penetration distance over an eddy cycle, thus increasing the eddy shedding period. In section 3 we noted that reducing the north-south extent of the basin can in some cases increase the eddy shedding period. This was effectively done in part of the basin when the Yucatan Peninsula was inserted. The eddies were also required to shed at a higher latitude, reducing the internal Rossby wave speed by about 7%, thus from (14) potentially increasing the eddy shedding period by a similar amount. However, this effect was not reflected in the actual movement of the eddies (Table 2, Cases RG1 and RG37).

b. Bottom topographic influences

Thus far we have examined the dynamics of the Loop Current in terms of a reduced gravity system and a barotropic or two-layer system with a flat bottom. Figure 2 shows that the bottom topography of the Gulf of Mexico varies dramatically over the basin. While the bottom is deeper than 3500 m in the western Gulf, it is 180 m deep or less over roughly 20% of the Gulf area. Along the Campeche escarpment the bottom slopes are greater than one percent and in the vicinity of the Yucatan and Florida Straits they may be very nearly as large. From simple scaling of the depth-averaged vorticity equation, it is clear that in the vicinity of the Loop Current, bottom slopes may result in vorticity advection (through the topographic beta effect, $-\frac{f}{h} \vec{v} \cdot \nabla h$) larger than the planetary vorticity advection. We have already demonstrated the crucial role of beta in the eddy shedding process. We must now investigate the additional influence of the

topography. Further, it is likely that the baroclinic instability and mixed instability which we observed in the flat bottom experiments is considerably modified by the bottom roughness. Rhines (1977) has shown that significant bottom variations on scales greater than the deformation radius are important for preserving vertical shear. Without this bottom influence the energy cascade toward depth-independent flow may have a time scale of only a few months. The results of McWilliams and Flierl (1979) suggest that such a cascade would make the eddies increasingly subject to dispersion, particularly in the lower layer.

We have included the Gulf topography in the idealized fashion discussed in section 2 and shown in Figure 3. We have retained the large scale features of the topography, maintained the proper depth scales and preserved the significant slopes in this idealization. Much of the topographic variability on scales less than the deformation radius has been removed.

To illustrate the control of the topography on the barotropic mode, we designed a one-layer experiment with topography which was identical to a flat bottom barotropic experiment in which no eddy shedding occurred. The deepest water was 3000 m in each case, and a constant 30 Sv inflow was applied with a parabolic cross-stream inflow profile. Other parameters are also standard (Table 1). Figure 23 shows the steady state FSA for both cases. No eddy shedding occurred in either experiment. Note that the bottom topography exerts such overwhelming control on the current in Figure 23b that upon entering the Gulf it traverses a 5000 km path clockwise around the basin to the outflow port rather than take the 400 km direct path. The strong tendency for this barotropic current to follow f/h contours is reflected in the outline of the FSA, which looks very similar to the bottom depth contours in Figure 3. Through the topographic beta effect, the divergence term in the vorticity equation, (17), is of crucial importance in the case with topography, unlike the flat bottom case.

Before investigating direct topographic influences due to inflow in the deep water, we will conduct a set of three nearly identical experiments with standard parameters (Table 1), except that in the first experiment we use the reduced gravity model with 25 Sv inflow, in the second we use the two-layer, flat bottom model with 25 Sv in the upper layer, no inflow transport in the lower layer, and in the third we add bottom topography to the second experiment. These experiments were integrated to statistical equilibrium for six years. Figure 24 shows snapshots of PHA for each experiment during year 6 and Figure 25 shows phase plots of PHA for the first five years in a north-south section at $x = 810$ km.

Although each experiment was forced with the same inflow transport in the upper layer, it is clear that the energy of the eddy following separation is markedly different in the three cases. Loss of energy to the deep water through a generalized baroclinic instability (Rhines, 1977) is impossible in the reduced gravity cases. Consequently, the eddy maintains its intensity as it approaches the western boundary. However, in the flat bottom case, where loss of energy to the deep water is possible, the eddies are weaker than in the reduced gravity experiment and lose much of their energy by the time they reach the western boundary. Further, by the time they reach the western Gulf they have a smaller diameter than the eddies from the other two experiments. For the bottom topography experiment the eddy intensity is intermediate between the reduced gravity and the two-layer flat bottom experiment. Also, for both the topography experiment and the reduced gravity experiment the shed eddies are discrete, whereas in the flat bottom experiment we observe a westward bending loop with eddies imbedded in it. The latter is characteristic of the weak eddy shedding regime near the transition between regimes E and W (Fig. 18). The case with a pure signature of baroclinic instability (Figs. 12, 13a) is identical to the flat bottom case discussed here except that the inflow is 27° west of normal and the upper layer inflow transport is 20 Sv rather than 25 Sv. It also exhibits eddies superimposed on a westward

bending loop, but the period of the eddies is only 58 days.

The eddy shedding period in days for these three cases is 360 for the reduced gravity, 161 for the two-layer flat bottom, and 248 for the two-layer with Gulf topography. The short eddy shedding period in the two-layer flat bottom case is apparently a consequence of the loss of energy from the upper to the lower layer, which tends to weaken the Loop Current. The eddies shed from the Loop are thus neither as intense, nor as large ($r \approx (v_C/\beta)^{1/2}$) in the two-layer flat bottom experiment as in the reduced gravity experiment. Since we found in section 3 that the eddy shedding period was, to a good approximation, directly proportional to the eddy size, (14), we expect weaker eddies to shed at a higher rate. Our results are consistent with the prediction that the eddy shedding period is shortest in the experiment with greatest energy loss from the Loop Current to the lower layer and longest for the reduced gravity case with no transfer of energy to the lower layer.

Even the case with a pure signature of baroclinic instability is quite consistent with these ideas, both in terms of the $r \approx (v_C/\beta)^{1/2}$ scale and an eddy period of $p_e = 2d/c_e$, c.f. (14), where $A_0 = 0$ and $A_1 = 2$ are regression coefficients suggested at the end of section 3b for a continuous wave train, when d is the east-west diameter of an eddy. Thus, in a mixed stability regime we find an eddy period which depends on the partitioning of the energy transfer between the paths for baroclinic and horizontal shear instabilities, although a higher frequency similar to that for the baroclinic instability tends to be superimposed (compare Figs. 25b and 11a with mixed stability to Figs. 12c and 13a with baroclinic instability). In the mixed stability regime the primary period falls between those for pure baroclinic and pure horizontal shear instability. These ideas will be the subject of further investigation in future work.

Both the eddy shedding period and the eddy diameter for the reduced gravity model are closer to those for the bottom topography experiment than to those for

the flat bottom experiment. Since inclusion of Gulf topography significantly reduces the transfer of energy to the deep water compared to the flat bottom model, our use of the reduced gravity model, which totally prevents such a transfer, is both useful and in some ways more realistic than the use of a two-layer flat bottom model. Thus the reduced gravity model may be more representative of the actual Gulf than the two-layer flat bottom model.

Bottom topography in conjunction with deep water inflow through the Yucatan Straits can have an additional important effect on the path and stability of the Loop Current. We will indicate the transport distribution (in Sv) between the two layers by the notation T_1/T_2 , where T_1 represents the upper layer transport on inflow and T_2 represents the lower layer transport on inflow. In the next experiment we utilize the model with bottom topography described above. At the end of year 6 we gradually increase the deep water transport from 0 to 10 Sv with a time constant of 30 days. Figure 26a shows the domain-averaged kinetic energy for years 4-8. Note that the eddy shedding totally ceases when the deep transport is increased even though the maximum vertical shear decreases by only about 10%. The nearly steady flow of the Loop Current is indicated by the PHA at day 2880 in Figure 26b. When the deep transport is again reduced to zero the eddy shedding resumes, as we will demonstrate shortly.

Initially, two hypotheses were considered for explaining these model results. The first is that the topographic beta effect acts to oppose planetary vorticity advection on inflow due to the downward sloping topography. This would inhibit westward spreading and subsequently eddy shedding. The second is that the Campeche Bank blocks the westward spreading of the Loop and also inhibits the eddy shedding process. One experiment to test these hypotheses involved totally removing both the Campeche Bank and the bottom slope on inflow. Figure 27a shows the modified topography used for this experiment. Using this topography we repeated the

previous experiment which produced a steady flow with a 25/10 transport profile. After three years of integration the model reached a steady state very similar to that of the full bottom topography experiment (Fig. 26b). Clearly, neither the bottom slope on inflow nor the Campeche Bank topography are responsible for this steady regime. At the beginning of year 4 we gradually reduced the deep water transport to zero using a 30-day time constant. Eddy shedding resumed as in the full topography case. This is shown by the domain averaged kinetic energy in Figure 27b. In another experiment we used the topography of Figure 27a, except that we moved eastward by 100 km all of the topographic features along the eastern boundary. Unlike the previous case, the 25/10 transport profile produced eddy shedding. This demonstrates the importance of the location of the Florida Shelf in controlling the dynamics.

To elucidate the dynamics of the transition from stable to unstable regimes, we first examined the kinematics of the flow using the upper layer continuity equation, (2). In the steady state the divergence term, $h_1 \nabla \cdot \vec{v}_1$, is balanced by the advective term, $\vec{v}_1 \cdot \nabla h_1$. In Figure 28 we have plotted the bottom topography, the divergence term and the advective term for the steady regime over a 500 x 500 km region near the outflow boundary. The large divergence over the topography ($0.024 \text{ cm sec}^{-1}$) is clearly shown in Figure 28b.

We can gain further insight into the role of the advective term in (2) by assuming quasi-geostrophy such that

$$\vec{v}_1 \cdot \nabla h_1 \approx \vec{v}_{lg} \cdot \nabla h_1 = \frac{g}{f} J(h_2 + D, h_1) ,$$

where \vec{v}_{lg} is the geostrophic velocity and D is the height of the topography above a reference level. The Jacobian may also be rewritten as $J(n_2, n_1)$, where n_1 is the deviation of the free surface from its rest value and n_2 is the interface deviation from its rest value. Figure 28d is a contour map of $\frac{g}{f} J(n_2, n_1)$. It is virtually

identical to Figure 28c, confirming quasi-geostrophy.

Since the flow is quasi-geostrophic, $\vec{v}_1 \cdot \nabla h_1 \approx \vec{v}_{1g} \cdot \nabla h_1 = \vec{v}_{2g} \cdot \nabla h_1$. We will use this information to show how the flow in the lower layer can prevent the northward penetration of the Loop Current. The magnitude of $\vec{v}_{2g} \cdot \nabla h_1$ is greatest when relatively strong lower layer currents flow at large angles to contours of upper layer thickness. Comparison of Figures 26b (contours of $h_1 - H_1$) and 26c (contours of lower layer pressure) shows that this occurs when the Loop Current approaches the Florida Shelf, since a current in the lower layer tends to follow the f/h contours of the shelf. If this current is strong enough for the advection to balance the divergence associated with the approaching Loop in (2), then the interface deepening and Loop Current penetration in this region are halted.

How does this affect the penetration of the remainder of the Loop? We have seen two cases (Figs. 26 and 27) where the Loop penetration ceased entirely. In a third case, where the Florida Shelf had been moved further eastward, the Loop Current penetrated far into the Gulf and shed eddies. The Florida Shelf in conjunction with the lower layer flow effectively changes the port separation by locally limiting the northward penetration of the current. If this results in $R_B > 2$ when we measure $2 L_p$ as the distance between the center of the inflow port and the point of maximum $\vec{v}_1 \cdot \nabla h_1$ (Fig. 28), then the current falls into regime N with source-sink flow, a regime discussed in section 4a (Fig. 18). This is illustrated by comparing Figs. 17 and 26b. Figure 17 is a reduced gravity case with a land mass inserted which was designed to match the location of the Florida Shelf.

At the beginning of year 4 we reduced the deep water inflow transport in the experiment shown in Figure 27. Soon after, the Loop Current penetrated northward into the Gulf, spread westward, and proceeded to shed eddies in a regular fashion. When the lower layer inflow transport was reduced, the current in the lower layer

along the Florida Shelf weakened and $\vec{v}_1 \cdot \nabla h_1$ was no longer able to balance the divergence term. Thus, the interface deepened and the Loop Current penetrated northward.

Figure 26a shows a case where the Loop Current had already penetrated far into the Gulf before the lower layer inflow through the Yucatan Straits was increased. When this increase occurred, a current in the lower layer developed along the Florida Shelf slope following f/h contours and the advection ($\vec{v}_1 \cdot \nabla h_1$) began to exceed the divergence term in the continuity equation where the Loop Current crossed the shelf slope, causing the interface to shallow there. Thus, the Loop Current began to retreat southward until an equilibrium occurred near the southern end of the shelf.

It is also of interest to investigate the changes in the vorticity balance due to topography. We find some notable differences from the results of Holland (1973). From a vorticity analysis we can obtain term balances for each layer and for the total fluid column. The steady state mass transport vorticity equations for each layer and for the total depth are

$$(NL)_1 + \beta V_1 + g J(n_1, n_2) - A \nabla^2 \zeta_1 = 0 \quad (21)$$

$$(NL)_2 + \beta V_2 + (g-g') J(n_1, D) - (g-g') J(n_1, n_2) + g' J(n_2, D) - A \nabla^2 \zeta_2 = 0 \quad (22)$$

$$\begin{aligned} \rho_1 (NL)_1 + \rho_2 (NL)_2 + \beta (\rho_1 V_1 + \rho_2 V_2) + \rho_2 (g-g') J(n_1, D) + \rho_2 g' J(n_2, D) \\ - A \nabla^2 (\rho_1 \zeta_1 + \rho_2 \zeta_2) = 0 \end{aligned} \quad (23)$$

We have represented the sum of the nonlinear terms in the vorticity balance by the letters NL, and here $\zeta_i = V_{ix} - U_{iy}$. Note that in each equation there are terms representing pressure torques. For the total mass transport, (23), the bottom pressure torque is represented by two terms. The first term is analogous to Holland's (1973) surface pressure torque term and the second corresponds to his density compensation term.

Figure 29 provides a plot of the term balances in Eq. 21-23 along a section crossing the Loop Current from $x = 600$ km to $x = 1600$ km at $y = 197.5$ km. This section passes directly over the area of strong divergence shown in Figure 28. For both the deep layer and for the sum of the layers the individual pressure torque terms have been combined for plotting purposes.

In the upper layer, across that part of the stream flowing over steep topography, the "thermocline pressure torque" very nearly balances the nonlinear terms. Planetary vorticity advection is surprisingly unimportant, as is vorticity diffusion. In the deep water the length scales are considerably shorter than at the surface, being dominated by the scale of the topographic slope. The term balance is not as clear-cut in the deep water, although the pressure torques still tend to balance the nonlinear terms. The sum of mass transport vorticity from each layer yields a clear balance between the bottom pressure torque and the nonlinear terms over the topography. This is in marked contrast to Holland (1973) who found that, in the Gulf Stream over the continental slope, the bottom pressure torque was balanced by planetary vorticity advection. The nonlinear terms in his experiment contributed less than one percent to the total.

In terms of vorticity, the dynamics for this regime of the Loop Current, when deep transport is significant, may be summarized as follows. The Loop Current becomes "locked" into the steady regime when the deep-water transport is sufficiently large that it produces strong pressure torques which balance relative vorticity advection over the steep slope. In that case deepening of the layer interface is prevented and the Loop Current is unable to penetrate into the Gulf - a prerequisite for spreading westward into the unstable configuration which leads to eddy shedding. When the deep transport is reduced and the pressure torques decrease, the steady balance breaks down and the interface begins to deepen. Once this deepening process begins, the Loop is able to penetrate northward into the

Gulf, spread westward under the influence of Rossby wave dynamics, and reach an unstable configuration.

Our results strongly suggest that the deep water transport through the Yucatan Straits may be of crucial importance for the control of Loop Current penetration and stability. Rather than monitoring the transport and velocities in the upper part of the water column, it may be more important to monitor the deep transport. Significant changes in deep water transport through the Yucatan Straits may be reflected by marked changes in the behavior of the Loop Current. The recently reported observations of southward flow near the bottom of the Yucatan Channel during a one-month period (Hansen and Molinari, 1979) indicate the need for additional modeling and field studies of the deep flow and its influence on the Loop Current.

c. Time-dependent inflow

Our investigations have demonstrated that the growth and instability of the Loop Current do not require time-dependent inflows as an essential element of the dynamics. Nevertheless, it is possible that the variability of total transport and/or current profiles through the Yucatan Straits significantly influences the actual Loop Current behavior. Unfortunately, there exist few direct current measurements in the Yucatan Straits to provide estimates of spatial or temporal variability of the inflow on time scales comparable to the eddy shedding period. Existing geostrophic transport calculations based on hydrographic sections suffer from the classical problem of choice of reference level. Many investigators, including Schlitz (1973), Morrison and Nowlin (1977), Molinari and Yager (1977), Maul (1977, 1979), and Hansen and Molinari (1979) have estimated geostrophic transport through the Yucatan Straits on time scales from days to months. Molinari and Yager (1977) found from repeated hydrographic surveys across the Yucatan Straits during a 26-day period during May 1972, that the mean transport relative to

700 m was 18.2 (\pm 1.3) Sv with a 7% variation in transport over the period. Hansen and Molinari (1979), using both hydrographic data and direct current meter data, estimated total transport across the Straits to be 25.8 Sv during October 3-5, 1970 and 27.1 Sv during October 26-27, 1970. The 5% difference in transport was considered to be within observational error. The cross-stream position of the maximum current above 700 m varied from near the center of the stream to near the western boundary during the three-week period. The 1972-73 estimates of geostrophic transport relative to 700 m by Maul (1979) indicated highest transports and current speeds in December, February, and March and minimum values in May, June and July. His finding is counter to the cycle reported by Fuglister (1951) and Cochrane (1965) who reported speed maxima during the summer months.

Although there are no statistically-significant, annual time-scale measurements of transport through the Yucatan Straits, proxy data from the Florida Straits obtained by Niiler and Richardson (1973) do exist. Seven years of directly measured transport and horizontal current data from Miami to Bimini were fitted to an annual sinusoid, giving a mean total transport of 29.5 Sv with an amplitude of 4.1 Sv and a peak transport in early June. Importantly, there was as much variability within a particular season as from season to season.

For the Yucatan Straits, the oceanographic observations are presently inadequate to provide unbiased estimates of cross-stream current profiles on the eddy shedding time scale. At best the data give short term estimates of mean total transport, cross-stream transport profiles and transport fluctuations. The data suggests that both cross-stream velocity profiles and total transport have short term (days to weeks) fluctuations comparable to the seasonal and longer-term fluctuations.

To test the hypothesis that Loop Current growth and eddy shedding are correlated with transport fluctuations through the Yucatan Straits on the seasonal

time scale, we have conducted numerical experiments in which a time-varying component was superimposed on the mean inflow transport. Unlike Wert and Reid (1972), who varied the velocity profile markedly over an annual cycle while leaving the total transport constant, we have not considered in detail time-dependent fluctuations in the velocity profile across the Straits. However, as discussed in section 3, it is the speed of the Loop Current rather than its relative vorticity distribution which is most important in determining the eddy shedding rate, the diameter of the eddies, and the eddy intensity. For example, the standard 20 Sv reduced gravity experiment with a parabolic inflow profile and maximum inflow speed of 72.9 cm sec^{-1} yielded an eddy shedding period of 327 days and a characteristic eddy diameter of 373 km. The identical 20 Sv experiment with a uniform cross-stream profile and an inflow speed of 63 cm sec^{-1} was also integrated to statistical equilibrium. The conservation of potential vorticity dynamics discussed in section 3 indicate that the eddy diameter and eddy shedding period for this flat profile case should be smaller by the square root of the ratio of the maximum inflow speeds for the two cases. This yields a shedding period for the flat profile case of 304 days and an eddy diameter of 347 km. The observed period for the flat profile experiment is 308 days, the observed diameter 348 km. Thus we are able to explain the results from these two experiments with differing cross-stream profiles on inflow with only a knowledge of the maximum current speeds in each profile. These results suggest that time variations in inflow speed at the core of the current are considerably more important to the shedding process than time variations of the detailed shape of the cross-stream inflow profile. We shall concentrate on this aspect of the time-dependent forcing. The experiments described in this subsection use a time-varying total inflow transport with a parabolic profile for V and relatively small time-dependent variations in the shape of the cross-stream velocity profile associated with upwelling and downwelling at the inflow port.

Four experiments were performed in which a sinusoidally-varying component was

superimposed on the mean 20 Sv inflow of the standard reduced gravity model. Peak-to-peak amplitude of the time-dependent component was 10 Sv. This is at least as large as the observed maximum transport fluctuation observed through the Yucatan Straits on any time scale. Each of the four experiments was run to statistical equilibrium with a period of 360, 240, 180, or 110 days for the time varying component of the inflow. Figure 30 summarizes the results of these experiments in terms of potential energy density plots for the standard case with constant inflow transport and for the 360, 240 and 180 day period time-dependent forcing. These curves were calculated from time series of PHA constructed at a point in the model where shed eddies were always observed to pass. In these experiments the point was located at $x = 810$ km, $y = 421.9$ km.

The 327 day eddy shedding period for the constant inflow case shows up clearly as a pronounced maximum in the spectrum (Fig. 30a). Harmonics near periods of 164, 109, and 82 days are also clearly evident. We will term the 327 day period the "natural" period of oscillation for the standard case. When we add the annual forcing to the mean inflow, the maximum spectral peak shifts to the one-year period, as shown in Figure 30b. There is no peak at the natural period. Harmonics at 6, 4 and 3 months are clearly evident. The annual cycle for the eddy shedding is also observed when individual eddies are monitored in their separation from the Loop Current. This suggests that the maximum in the spectrum may consistently appear at the forcing frequency. However, in the eight month forcing experiment no dominant spectral maximum at the forcing frequency is found (Fig. 30c). Rather, we observe a broad maximum centered near the natural frequency. The eddy shedding periods we actually observe in this model realization range from 7 to 13 months, with considerable variability from one eddy cycle to the next. This is shown in the phase plots for the PHA in Figure 31a. This range of variability for the eddy shedding is comparable to that observed (Behringer, et al. 1977).

The experiment with semi-annual forcing produced a striking result. The eddy shedding period was nearly annual (Fig. 30d). As discussed in section 3, this is because the time scale for the growth of the horizontal shear instability is short compared to the time required for the Loop Current to penetrate into the Gulf and bend westward into an unstable configuration. In this experiment the first maximum in inflow transport for the year occurred when the Loop was just beginning to penetrate into the Gulf. The transport maximum and subsequent decrease did not coincide with an unstable configuration. However, by the time the second yearly maximum in inflow transport occurred, the Loop had penetrated well into the Gulf and the time variation in the inflow was able to exert some influence on the timing of the eddy shedding.

Because the observed period is 356 days while the forcing period is 180 days, the forcing and the shedding gradually shift out of phase until the first transport maximum of the year rather than the second influences the timing of the eddy shedding. Figure 31b shows the phase plot of PHA for years 5 through 15 for this experiment. Note that during years 5 through 10 the eddy passes through our north-south section with maximum amplitude slightly after the beginning of a year. The time between eddy sheddings is 356 days. This yields a very sharp peak in the potential energy spectrum, as shown in Figure 30d. However, by year 11 we see a transition in the time of eddy passage in Figure 31b, and by year 12 the eddies are passing through our section with maximum amplitude just after the middle of a year. Following the transition the eddy shedding period is again approximately 1 year. Were we to recalculate our spectrum for this experiment using a very long record with equal numbers of shed eddies for each phase of eddy shedding, the maximum at the annual period would be reduced and a semi-annual peak should become apparent.

The final experiment with a 110 day forcing period yielded results similar to the semi-annual forcing except that the strong spectral maximum occurred at the 330 day

period with higher harmonics also containing significant energy.

These experiments indicate that time-dependent fluctuations with periods very near the natural eddy shedding period may shift the eddy shedding to nearly the forcing period. For inflow forcing with periods significantly different from the natural period or its harmonics, the eddy shedding may become erratic, with considerable variation in the shedding period. The short time scale for growth of the Loop Current instability compared to the time scale for penetration of the Loop into the Gulf has significant implications for Loop Current response to seasonal time scale fluctuations in inflow forcing. If the Loop is close to an unstable configuration, transport fluctuation at inflow may substantially influence the timing for eddy break-off.

It should be noted that our time-dependent experiments were conducted with the reduced gravity model. However, from section 4b it is clear that changes in deep water transport through the Yucatan Straits may lead to cessation of Loop Current penetration and eddy shedding. Thus, relatively small fluctuations in deep water transport on seasonal or annual time scales could modulate the Loop Current penetration and eddy shedding.

5. Summary and conclusions

We have used three nonlinear numerical models to study the dynamics of the Loop Current-eddy system in the Gulf of Mexico: two-layer, barotropic and reduced gravity. A second active layer allowed the possibility of baroclinic instability, and allowed inclusion of both the pycnocline and idealized topography of the Gulf. The barotropic and reduced gravity models were used to demonstrate the individual behavior of the external and internal modes, and to provide insight on how they interact in the two-layer model. They also allowed us to study certain dynamical features of the system in the simplest context. Because of the economy of the semi-implicit free surface models, it was possible to perform over 100 multi-year experiments to investigate the dynamics of the Loop Current-eddy system. Typically the models were integrated 3 to 5 years to statistical equilibrium on a 1600 x 900 km domain with resolution 20 x 18.75 km. Prescribed inflow through the Yucatan Channel was compensated by outflow through the Florida Straits.

A longstanding hypothesis is that the Loop Current sheds eddies in response to quasi-annual variations in the inflow through the Yucatan Straits. However, we first searched for purely internal mechanisms to produce the eddy shedding. Instead of starting with the simplest possible model and progressing toward more complicated experiments, we designed our first experiment to be as realistic as possible within the context of the two-layer model. This meant including idealized topography of the Gulf. However, in our search for purely internal mechanisms for the eddy shedding, we used a time invariant inflow profile. We found that the model can realistically simulate observed features of the eddy shedding by the Loop Current when model parameters realistic for the Gulf of Mexico are used, including the size, amplitude, and movement of the eddies. We also found that, contrary to an earlier hypothesis, time variations in the inflow are not required for the eddy shedding to occur at a realistic rate.

We next showed that the reduced gravity model is the simplest model which can simulate the basic features of the eddy shedding cycle of the Loop Current. Thus, baroclinic instability is not an essential element of the dynamics. Instead, there is a horizontal shear instability of the first internal mode. We also found that differential rotation is essential for eddy shedding to occur in a realistic manner. When we set $\beta=0$, the solution evolved to a steady source-sink flow with no eddy shedding or westward spreading. This was true even when we augmented the inflow with a large westward component and an annual variation larger than observed.

Fortunately, we were able to perform enough reduced gravity experiments to test a number of dynamical hypotheses using regression analysis. We found that the westward speed of the shed eddies was correlated with the nondispersive internal Rossby wave speed with a correlation coefficient of 0.991, but it was necessary to include dispersion to obtain quantitative agreement of the speeds. Theoretical expressions for the eddy diameter and the penetration distance of the Loop Current into the Gulf were obtained by extending a potential vorticity argument on a β -plane by Reid (1972). The theoretical diameter, $2r$, was consistent with beta Rossby number, $R_B = v_{in}/(\beta r^2) = 1$, and predicted the diameter of the eddies found numerically with an average error of 6%, based only on a knowledge of the value of β and the maximum speed of the current at inflow, v_{in} . A simplification of the expression for penetration distance was tested using regression. We obtained an average fit error of 2% and a linear correlation of 0.986, using eddy diameters obtained numerically. Hence, we have demonstrated the importance of differential rotation in determining the diameter of the eddies, and the penetration of the model Loop Current into the Gulf.

Two time scales are associated with the eddy shedding: the time for the Loop Current to penetrate into the Gulf and spread westward into an unstable

configuration, and the much shorter time scale for the growth of a horizontal shear instability as the eddy separates from the Loop Current. The Loop Current does not necessarily meet any criterion for instability over much of an eddy cycle. The eddy shedding period is a small multiple of the time required for an eddy to move the diameter of the eddy after shedding. This multiple depends on the inflow angle of the current. Thus, in the most realistic regime, the eddy shedding rate depends on the internal Rossby wave speed, an eddy diameter derived from conservation of potential vorticity on a β -plane, and the angle of the inflow. To a lesser extent it also depends on the Reynolds number. As the flow becomes more inertial, the eddy shedding period is increased, perhaps a counter-intuitive result. This is due to the way friction modifies the results predicted by conservation of potential vorticity on a β -plane. Correlations of 0.95 to 0.98 and mean fit errors of 6 to 8% were obtained in our regression predictions of eddy shedding period.

The eddy shedding can be prevented by reducing the Reynolds number sufficiently. However, the Loop Current still spreads far westward. The steady state solution for a highly viscous case was found to be almost the same as the mean over an eddy cycle of a lower viscosity case which shed discrete eddies of large amplitude. In a few of the two-layer experiments, baroclinic and mixed instabilities were encountered, but experiments dominated by a horizontal shear instability of the internal mode produced the most realistic results. For sufficiently high Reynolds numbers the shear instability occurred in both the barotropic and reduced gravity models. However, for realistic parameter values eddy shedding occurred in the two-layer and reduced gravity models, but not in the barotropic model.

Experiments using the reduced gravity model showed that while the solution depends on the maximum velocity at inflow, it is relatively insensitive to the shape of the inflow profile or to the location of the ports. When the ports were

relocated by several hundred kilometers, the Loop penetration, the eddy shedding period, and the eddy diameter, amplitude and movement were little affected, so long as the western boundary did not interfere with the shedding process, and the ports were not unrealistically close. The solution was also quite insensitive to the width of the outflow port. Even when the entire eastern boundary was opened, the outflow was confined to a current adjacent to the southern boundary, suggesting a dynamical rather than a geological explanation for the location of the Florida Straits. These results are consistent with the domination of the model behavior by conservation of potential vorticity dynamics.

Some of the diverse results from the barotropic flat bottom model and the reduced gravity model have been summarized in a regime diagram with Reynolds number, Re vs. beta Rossby number, R_B (Fig. 18). The length scale for Re is one half the port width, for R_B one half the port separation. For low Re and R_B (regime W) the Loop Current spreads westward and evolves to a steady state without shedding eddies. For high Re and low R_B (regime E) the Loop Current sheds eddies with no time variation in the external forcing. Near the transition between regimes E and W the eddies are superimposed on a westward spreading loop. For high R_B (regime N) the Loop Current evolves to a steady source-sink flow with no westward spreading or eddy shedding. The f-plane solution belongs to this regime. The port separation, $2L_p$, is approximately $L_p < r/\sqrt{2}$ for this regime to occur, where $r = (v_c/\beta)^{1/2}$, a theoretical eddy radius, and v_c is the speed at the core of the current.

The Florida Shelf topography plays a crucial role in the Loop Current-eddy shedding dynamics in certain realistic regions of parameter space. If the lower layer inflow through the Yucatan Straits is sufficiently high, then the Loop Current evolves to a steady source-sink flow resembling the N regime with no westward spreading or eddy shedding. The current in the lower layer tends to

follow the f/h contours of the Florida Shelf and intersects the Loop Current in the upper layer at large angles. A kinematic analysis shows that in this situation the advection term can balance the divergence term in the continuity equation for the layered model, if the current in the lower layer is sufficiently strong. Locally, this prevents the deepening of the interface associated with the northward penetration of the Loop Current. This effectively reduces the port separation and forces the current into the N regime. When the Florida Shelf topography is moved 100 km eastward, the westward spreading and the eddy shedding reappears. In terms of vorticity dynamics, the northward penetration of the Loop Current is halted when the interaction between the topography of the Florida Shelf and the pressure field results in a near balance between the pressure torques and the nonlinear terms in the mass transport vorticity equation.

Another important role of the topography is to inhibit baroclinic instability. As a result numerical experiments using the two-layer model with idealized Gulf topography resemble those using the reduced gravity model more closely than those using the two-layer flat bottom model, although the movement of the shed eddies is significantly modified by the introduction of topography.

The response of the current to time-varying inflows was complex. Importantly, the eddy shedding frequency was not dominated by the forcing frequency for realistic transport fluctuations. The natural frequency was of much greater importance in determining the eddy shedding rate in these cases. For example, the reduced gravity model with a constant 20 Sverdrup inflow yielded a natural eddy shedding period of 327 days. When a semi-annual sine-wave fluctuation with a 10 Sv peak-to-peak amplitude was superimposed on the mean inflow, the eddy shedding period was 356 days.

ACKNOWLEDGMENTS

We extend our appreciation to Dr. L. B. Lin, Ruth Preller, John Harding, and Monty Peffley for writing much of the analysis and display software and assisting us in analyzing the model results. We extend our appreciation to Dr. Dan Moore of Imperial College, London who provided the fast vectorized Helmholtz solvers for both rectangular and irregular geometries. They were used in obtaining most of these results. We thank Drs. David Dietrich and Rao Madala for providing Helmholtz solvers used in early versions of the numerical model. We also thank Drs. Steve Piacsek and Juri Toomre for their encouragement of this work. Initial stages of this research were funded by the Department of Energy as part of the Ocean Thermal Energy Conversion Program. Some of the graphics software was supplied by the National Center for Atmospheric Research, Boulder, Colorado. NCAR is sponsored by the National Science Foundation. Computations were performed on the two-pipeline Texas Instruments Advanced Scientific Computer at the Naval Research Laboratory in Washington, DC.

APPENDIX A

List of Symbols for Model Equations

A	horizontal eddy viscosity
D	height of bottom topography above a reference level
f	Coriolis parameter
g	acceleration due to gravity
g'	reduced gravity, $g (\rho_2 - \rho_1)/\rho$
h_1, h_2	instantaneous local thickness of the layers
$H_1, H_2(x, y)$	initial thickness of the layers
t	time
u_1, u_2	x-directed components of current velocity
v_1, v_2	y-directed components of current velocity
\vec{v}_1, \vec{v}_2	$\vec{h}_1 \vec{v}_1, \vec{h}_2 \vec{v}_2$
x, y, z	tangent plane Cartesian coordinates: x positive eastward, y positive northward, z positive upward
β	differential rotation, df/dy
Δt	time increment in the numerical integration
$\Delta x, \Delta y$	horizontal grid increments
η_1	free surface anomaly; height of the free surface above its initial uniform elevation; $\eta_1 = h_1 + h_2 - H_1 - H_2$
η_2	$\eta_2 = H_1 + \eta_1 - h_1 = h_2 - H_2 = - \text{PHA}$
ρ, ρ_1, ρ_2	densities of sea water
τ_i^x, τ_i^y	x and y directed tangential stresses at the top (i) and bottom (i+1) of layer i.

Additional symbols are defined in Tables 1 and 2

APPENDIX B

Numerical Design of the Semi-Implicit Gulf of Mexico Models

The model equations, (1) through (3), are solved numerically on a staggered grid. The smallest representation of the "C" stencil (e.g., Mesinger and Arakawa, 1976) is

$$\begin{array}{c} v \\ u \quad h \quad u \\ v \end{array}$$

Defining the operators,

$$\delta_{mz}(W(z)) = \frac{1}{m\Delta} [W(z+m\Delta/2) - W(z-m\Delta/2)] ,$$

$$\overline{W(z)}^{mz} = \frac{1}{2} [W(z+m\Delta/2) + W(z-m\Delta/2)] ,$$

and

$$\delta^2 = \delta_{xx} (\quad) + \delta_{yy} (\quad) ,$$

where W is a function of the discrete variable, z , Δ refers to a space or time increment, and m is an integer, the finite difference form of the model equations is

$$\begin{aligned} \delta_{2t} U_i &= -\delta_x (\overline{U}_i^x \overline{U}_i^x) - \delta_y (\overline{V}_i^x \overline{U}_i^y) + f \overline{v}_i^y h_i \\ &- H_i \delta_x \overline{P}_i^{2t} - (\overline{h}_i - H_i) \delta_x P_i + \tau_i^x - \tau_{i+1}^x + A \delta^2 U_i^{t-\Delta t} , \end{aligned} \quad (A1)$$

$$\delta_{2t} V_i = -\delta_x (\overline{U}_i^y \overline{V}_i^x) - \delta_y (\overline{V}_i^y \overline{V}_i^y) - f \overline{u}_i^x h_i$$

$$- H_i \delta_y \overline{P}_i^{2t} - (\overline{h}_i - H_i) \delta_y P_i + \tau_i^y - \tau_{i+1}^y + A \delta^2 V_i^{t-\Delta t} , \quad (A2)$$

$$\delta_{2t} h_i = -\delta_x \overline{U}_i^{-2t} - \delta_y \overline{V}_i^{-2t} , \quad (A3)$$

where $i=1,2$, $u=U/h^*$, $v=v/h^*$, the H_i are constants, and all differences are centered in space and time unless otherwise noted.

The time differencing is leap-frog, but an Euler difference is used for start and restart to prevent development of the time splitting associated with this scheme. Every ten days (160 time steps) the solution for two adjacent time steps is averaged, the solution written to a history tape, and an Euler restart performed. This procedure has virtually no effect on our numerical solutions. For advection a variant of the Lilly (1965) scheme, also known as Scheme C from Grammeltvedt (1969), is used. The Holland and Lin (1975) scheme is used for the Coriolis force. Horizontal friction is lagged in time for computational stability. The numerical scheme conserves mass and total energy except for the time average and restart procedure and explicit sources and sinks due to horizontal friction and to inflow and outflow through the ports.

The semi-implicit treatment of the external and internal gravity waves is patterned after Kwizak and Robert (1971) and O'Brien and Hurlburt (1972) and allows us to greatly exceed the usual time step limitation imposed by gravity waves in explicit models. By taking the divergence of the momentum equations and substituting into the continuity equations, the model equations can be solved in favor of n_1 and h_1 to form Helmholtz equations which are coupled in the vertical:

$$\nabla^2 n_1 - a_1 h_1 = a_1 (\Delta t \left[\frac{\partial U_1^*}{\partial x} + \frac{\partial V_1^*}{\partial y} \right] - H_1^*) , \quad (A4)$$

$$\nabla^2 n_1 - \frac{g'}{g} \nabla^2 h_1 - a_2 (n_1 - h_1) = a_2 (\Delta t \left[\frac{\partial U_2^*}{\partial x} + \frac{\partial V_2^*}{\partial y} \right] - H_2^*) , \quad (A5)$$

where we have already performed the time differencing, and $a_j = 1/gH_j \Delta t^2$. The left hand side of (A4) and (A5) are unknown values at time level $n+1$, and the right hand side is the known forcing function at time levels n and $n-1$. U_i^* , V_i^* , and H_i^* are the known forcing functions from the x-momentum, y-momentum, and continuity equations. To facilitate the solution of Helmholtz equations (A4) and (A5) in the two-layer model, they are decoupled in the vertical. Use of Lagrange multipliers is a convenient way to do this, although care is required to avoid large roundoff error in the calculation of the new coefficients of the Helmholtz terms in the decoupled equations.

From (A4) and (A5) it appears that we must know the boundary values for η_1 and h_1 or their normal derivatives at time levels $n-1$ and $n+1$ before we can obtain an interior solution. These are not generally known. In the limit as we approach a solid no-slip boundary the normal momentum equation reduces to a balance between the pressure gradient force, the wind stress, and the Laplacian horizontal friction. The situation is even worse at the eastern port where the normal velocity at the boundary of the model domain is self-determined. This difficulty is easily overcome without further approximation, if we first difference the primitive equations in space and time, and then form the finite difference analogue of the Helmholtz equations algebraically. This procedure also eliminates ambiguity in defining Δx , Δy on a grid with stretched coordinates. It will be illustrated for the barotropic model. The primitive equations can be written in finite difference form as

$$U_{i+\frac{1}{2},j} + \frac{gH\Delta t}{\Delta x_{i+\frac{1}{2},j}} (h_{i+1,j} - h_{i,j}) = U_{i+\frac{1}{2},j}^*, \quad (A6)$$

$$V_{i,j+\frac{1}{2}} + \frac{gH\Delta t}{\Delta y_{i,j+\frac{1}{2}}} (h_{i,j+1} - h_{i,j}) = V_{i,j+\frac{1}{2}}^*, \quad (A7)$$

$$h_{i,j} + \frac{\Delta t}{\Delta x_{i,j}} (U_{i+\frac{1}{2},j} - U_{i-\frac{1}{2},j}) + \frac{\Delta t}{\Delta y_{i,j}} (V_{i,j+\frac{1}{2}} - V_{i,j-\frac{1}{2}}) = H_{i,j}^*, \quad (A8)$$

where the left hand side of (A6) through (A8) are the unknowns at time level $n+1$ and U^* , V^* , and H^* represent all known quantities at time levels n and $n-1$, cf. (A1) through (A3). The grid index in the x -direction is i , in the y -direction, j , with integral values representing the h -grid. Substituting (A6) and (A7) into (A8) we obtain

$$\begin{aligned} h_{i,j} - \frac{a}{\Delta x_{i,j}} \left(\frac{h_{i+1,j} - h_{i,j}}{\Delta x_{i+\frac{1}{2},j}} - \frac{h_{i,j} - h_{i-1,j}}{\Delta x_{i-\frac{1}{2},j}} \right) - \frac{a}{\Delta y_{i,j}} \left(\frac{h_{i,j+1} - h_{i,j}}{\Delta y_{i,j+\frac{1}{2}}} - \frac{h_{i,j} - h_{i,j-\frac{1}{2}}}{\Delta y_{i,j-\frac{1}{2}}} \right) \\ = H_{i,j}^* - \frac{\Delta t}{\Delta x_{i,j}} (U_{i+\frac{1}{2},j}^* - U_{i-\frac{1}{2},j}^*) - \frac{\Delta t}{\Delta y_{i,j}} (V_{i,j+\frac{1}{2}}^* - V_{i,j-\frac{1}{2}}^*) , \end{aligned} \quad (\text{A9})$$

where $a = gH\Delta t^2$. At the western boundary $i=\frac{1}{2}$, and $U_{\frac{1}{2},j}$ is known at the necessary time levels: $n-1$, n , $n+1$. Thus, one half grid distance inside this boundary, instead of (A9), we obtain

$$\begin{aligned} h_{1,j} - \frac{a}{\Delta x_{1,j}} \left(\frac{h_{2,j} - h_{1,j}}{\Delta x_{\frac{3}{2},j}} + \frac{U_{\frac{1}{2},j}}{gH\Delta t} \right) - \frac{a}{\Delta y_{1,j}} \left(\frac{h_{1,j+1} - h_{1,j}}{\Delta y_{1,j+\frac{1}{2}}} - \frac{h_{1,j} - h_{1,j-\frac{1}{2}}}{\Delta y_{1,j-\frac{1}{2}}} \right) \\ = H_{1,j}^* - \frac{\Delta t}{\Delta x_{1,j}} U_{\frac{3}{2},j}^* - \frac{\Delta t}{\Delta y_{1,j}} (V_{1,j+\frac{1}{2}}^* - V_{1,j-\frac{1}{2}}^*) \end{aligned} \quad (\text{A10})$$

The h -field is determined in a similar fashion at the other boundaries and the corners of the h -grid. When the boundary conditions are included in the forcing function on the right hand side of the equation, the problem is reduced to the solution of a Helmholtz equation with homogeneous Neumann boundary conditions one-half grid distance outside the boundary of the h -grid. Hence, the need to know the true value of h or its normal derivative at the boundary has been eliminated.

This is true even at the eastern port where the normal flow is self-determined with the integral constraint that the total transport in each layer exactly compensate the prescribed inflow through the southern port (see Fig. 2). The normal flow at the boundary of the domain in the eastern port is predicted using the x -component of the momentum equation, (1). At times the model predicts inflow for part of the lower layer at the eastern port. The boundary condition used for this inflow is $U_x=0$, eliminating the advective term, $(Uu)_x$, and setting

$$U_{xx} \approx 2 (U_{N-1,j} - U_{N,j})/\Delta x^2 , \quad (A11)$$

where N is the index of the boundary in the x -direction. At outflow points the computational boundary condition used for the normal flow is $U_{xx}=0$. In addition to eliminating a component of the viscous term it causes Lilly's (1965) scheme to be exactly equivalent to using upstream differencing for the $(Uu)_x$ term at outflow, when we perform the computation at time level at $t-\Delta t$:

$$(Uu)_x \approx [U_N(u_N-u_{N-1}) + u_N(U_N-U_{N-1})]/\Delta x . \quad (A12)$$

The evolution of our solutions is sufficiently slow that gravity waves with significant amplitude are not excited, so the reflection of these waves is not a problem. The tangential flow at the ports is set to zero one-half grid distance outside the physical domain of the model. This weak overspecification at outflow eliminates the possibility that the Loop Current will exit the basin at unrealistic angles. More realistically, outflow should occur through a channel modeling the

Florida Straits. This was done in a few of the numerical experiments.

With the modifications described above, we have sufficient information to calculate all the terms in the x-momentum equation required to predict $U_{N,j}^{n+1}$ at the eastern port, except for the normal pressure gradient. This is determined by an integral constraint on the total transport through the eastern port in each layer. When the integral constraint is applied in the determination of $U_{N,j}^{n+1}$, the normal pressure gradient is assumed to be uniform across the port. For approximately geostrophic flow and a north-south oriented boundary as we have here

$$gh_x|_y = - \int_{y_0}^y f u_x dy + gh_x|_{y_0} . \quad (A13)$$

Hence, a uniform pressure gradient is a useful approximation, if the integral in (A13) is much less than the mean pressure gradient, or if the normal pressure gradient is a locally small term in the x-component of the momentum equation at the port. See Hurlburt and Thompson (1973, 1976) and Hurlburt (1974) for discussion of the normal pressure gradient in an east-west oriented cross-section.

We wish to calculate

$$u_{N,j}^{n+1} = -2\Delta t gh_x|_{N,j} + u_{N,j}^{*,n,n-1} , \quad (A14)$$

where u^* represents all the other quantities in the x-momentum equation known at time levels $n, n-1$. Since we assume $h_x \neq h_x(y)$ in the port

$$-2\Delta t gh_x|_{N,j} = \bar{u}_N^{n+1} - \bar{u}_N^{*,n,n-1} , \quad (A15)$$

where the overbar denotes an average across the port. In our case we must express this in terms of transports. Note $\bar{U} = \bar{u}h + \bar{u}'h'$, and $\bar{U}^* = \bar{u}^*h + \bar{u}''h'$, where primed quantities are deviations from the mean. Since $u_{N,j}^{n+1} = u_{N,j}^{*,n,n-1} + \text{constant}$, $u' = u^*$,

$$\bar{u} - \bar{u}^* = (\bar{U} - \bar{U}^*)/\bar{h} \quad (\text{A16})$$

and

$$u_{N,j}^{n+1} = h_{N-\frac{1}{2},j}^{n-1} \left(\bar{U}_N^{n+1} - \bar{U}_N^{*,n,n-1} \right) / \bar{h}_{N-\frac{1}{2}}^{n-1} + u_{N,j}^{*,n,n-1} \quad , \quad (\text{A17})$$

an equation which when integrated across the port gives the desired total transport based on a uniform normal pressure gradient across the port. The h values used are one-half grid distance into the interior at a known time level, and \bar{U}_N^{n+1} is the prescribed total transport in the layer through the port, divided by the width of the port. This transport is the only information at the ports required at a future time level a priori. Since it is prescribed as a function of time, we can predict $u_{N,j}^{n+1}$ in the port before calculating $h_{i,j}^{n+1}$ using the Helmholtz solver. Thus, the solver is provided with the boundary information required even at the ports where the boundary values are self-determined. Once we have $h_{i,j}^{n+1}$, the semi-implicit calculation of $u_{i-\frac{1}{2},j}^{n+1}$ and $v_{i,j-\frac{1}{2}}^{n+1}$ in the interior can be completed.

The behavior of the open boundary condition has been surprisingly good. When a similar boundary condition was used on the west side of the basin, a large amplitude internal Rossby wave in a westward mean flow was observed to pass cleanly through (unpublished results). Although ordinary gravity waves are reflected, Kelvin waves are observed to pass through (Hurlburt, Kindle, and O'Brien, 1976). Strong jets pass through (e.g., see Section 4a, Fig. 19a), as do eddies (unpublished results). In no case in the several applications so far have boundary layers with

significant amplitude appeared along an open boundary of this type. Also no smoothing or extra damping at the boundary was used in our application.

In the open boundary condition with self-determined flow the mean is constrained. In the case of an east-west boundary, deviations from the mean flow are somewhat constrained by the tendency to form a Sverdrup interior (Hurlburt and Thompson, 1973). However, this is not true for a north-south oriented boundary as here, allowing the possibility of unphysical growth of these modes. When the entire eastern boundary of the Gulf of Mexico model was opened, a gyre with the north-south scale of the basin developed in the eastern Gulf on a time scale much longer than an eddy shedding cycle (see Section 4a). It is driven by the strong Loop Current flowing out of the basin along the southern boundary, a physically reasonable result. When the model domain with the open eastern boundary was extended further eastward, the growth rate of the gyre was increased (Table 2, Cases RG44,45), perhaps because a greater percentage of the perimeter of the gyre within the model domain was in contact with the strong southern boundary current. This demonstrates an unphysical aspect of this growth, i.e., the growth rate dependence on the percentage of the gyre within the model domain.

The Helmholtz equations are solved using a vectorized variant of Hockney's (1965) method by Dan Moore (personal communication) for homogeneous Neumann boundary conditions one-half grid distance outside the h-grid. The nonrectangular geometry which incorporated the Yucatan and Florida Straits was included using a version of the capacitance matrix technique by Dan Moore (personal communication, see Hockney 1968, 1970). This requires a second call to the Helmholtz solver. The Yucatan Peninsula was included in one case, in which the Helmholtz equation was solved using a version of the stabilized error vector propagation (SEVP) method by David Dietrich (personal communication). Another version of this method is

described by Madala (1978). The implicit part of the finite difference equations for the gravity waves treat the gravity wave speed as a constant for each vertical mode. Deviations from this constant occur due to the dynamics and the topography. These components of the gravity waves are treated explicitly. This can be done without introducing conditional stability, if the deviations always act to slow the gravity waves from the reference value.

This layered model with transports, U , V , as dependent variables handles topography especially well. The continuity equation is linear in transport. The topography appears multiplicatively in the pressure gradient. The topography is differentiated only to the extent that it affects the velocity field in the advective terms. When large amplitude topography is introduced, restrictions on the time step and the eddy coefficient are affected only to the extent that the topography affects the amplitude of the velocity field (advective CFL condition) and the grid interval Reynolds number.

REFERENCES

- Behringer, D. W., R. L. Molinari, and J. F. Festa, 1977: The variability of anticyclonic current patterns in the Gulf of Mexico. J. Geophys. Res., 82 (34), 5469-5476.
- Blake, D. W., 1980: Trajectory of the Loop Current. (in preparation).
- Blake, D. W., Hurlburt, H. E., and J. D. Thompson, 1980: Parameterization of Laplacian friction in a layered model. (in preparation)
- Cochrane, J.D., 1965: The Yucatan Current and equatorial currents of the western Atlantic. In unpubl. Rept. of Dept. of Oceanography, Texas A&M University, College Station, Ref. (65-17T), 20-27.
- Cochrane, J. D., 1972: Separation of an anticyclone and subsequent developments in the Loop Current (1969). In Contributions on the Physical Oceanography of the Gulf of Mexico, Vol. II. L.R.A. Capurro and J. L. Reid, eds., Gulf Publishing Co., Houston, Texas, 3-51.
- Elliott, B. A., 1979: Anticyclonic rings and the energetics of the circulation of the Gulf of Mexico. Ph.D. Thesis. Dept. of Oceanography. Texas A&M University, College Station, 188 pp.
- Fuglister, F. C., 1951: Annual variations in current speeds in the Gulf Stream. J. Mar. Res., 10, 119-127.
- Grammeltvedt, A., 1969: A survey of finite-difference schemes for the primitive equations for a barotropic fluid. Mon. Wea. Rev., 97, 384-404.
- Hansen, D. V. and R. L. Molinari, 1979: Deep currents in the Yucatan Strait. J. Geophys. Res., 84, 359-362.
- Hockney, R. W., 1965: A fast direct solution of Poisson's equation using Fourier

analysis. J. Assoc. Comp. Mach., 12, 95-113.

Hockney, R. W., 1968: Formation and stability of virtual electrodes in a cylinder.
J. Appl. Phys., 39, 4166-4170.

Hockney, R. W., 1970: The potential calculation and some applications. In Methods in Computational Physics, 9, 135-211.

Holland, W. R., 1973: Baroclinic and topographic influences on the transport in western boundary currents. Geophys. Fluid Dyn., 4, 187-210.

Holland, W. R. and L. B. Lin, 1975: On the generation of mesoscale eddies and their contribution to the oceanic general circulation. I. A preliminary numerical experiment. J. Phys. Oceanogr., 5, 642-657.

Hurlburt, H. E., 1974: The influence of coastline geometry and bottom topography on the eastern ocean circulation. Ph.D. Thesis., Dept. of Meteorology, Florida State University, Tallahassee, 103 pp.

Hurlburt, H. E., J. C. Kindle, and J. J. O'Brien, 1976: A numerical simulation of the onset of El Nino, J. Phys. Oceanogr., 6, 621-631.

Hurlburt, H. E., and J. D. Thompson, 1973: Coastal upwelling on a β -plane. J. Phys. Oceanogr., 3, 16-32.

Hurlburt, H. E., and J. D. Thompson, 1976: A numerical model of the Somali Current. J. Phys. Oceanogr., 6, 646-664.

Kwizak, M., and A. J. Robert, 1971: A semi-implicit scheme for grid point atmospheric models of the primitive equations. Mon. Wea. Rev., 99, 32-36.

Leipper, D. F., 1970: A sequence of current patterns in the Gulf of Mexico. J. Geophys. Res., 75(3), 637-657.

Lilly, D. K., 1965: On the computational stability of numerical solutions of time-dependent non-linear geophysical fluid dynamics problems. Mon. Wea. Rev., 93, 11-26.

Madala, R. V., 1978: An efficient direct solver for separable and non-separable elliptic equations. Mon. Wea. Rev., 106, 1735-1741.

Martin, R. G., and J. E. Case, 1975: Geophysical studies in the Gulf of Mexico. In The Ocean Basins and Margins: Vol. 3, The Gulf of Mexico and the Caribbean. A.E.M. Nairn and F. G. Stehli, eds., Plenum Press, New York. 65-101.

Maul, G. A., 1977: The annual cycle of the Gulf Loop Current. Part I. Observations during a one-year time series. J. Mar. Res., 35, 29-47.

Maul, G. A., 1979: The 1972-1973 cycle of the Gulf Loop Current. Part II. Mass and salt balances of the basin. Symposium on Progress in Marine Research in the Caribbean and Adjacent Regions. Caracas, July, 1976. FAO Fisheries Report No. 200 Supplement, 597-619.

McWilliams, J. C., and G. R. Flierl, 1979: On the evolution of isolated, nonlinear vortices. J. Phys. Oceanogr., 9, 1155-1182.

Mesinger, F. and A. Arakawa, 1976: Numerical Methods Used in Atmospheric Models. GARP Publications Series No. 17. World Meteorological Organization. Genevea, Switzerland. Chapter 4, p. 45.

Molinari, R. L., 1978: An overview of the circulation in the Gulf of Mexico. Summary Report: Working Conference on the Circulation in the Gulf of Mexico. October 18-19, 1978., Tallahassee, Florida. Wilton Sturges and S. L. Shang, eds., 29-30.

Molinari, R. L. and R. E. Yager, 1977: Upper layer hydrographic conditions at the Yucatan Strait during May, 1972. J. Mar. Res., 35, 11-20.

Morrison, J. M., and W. D. Nowlin, 1977: Repeated nutrient, oxygen, and density sections through the Loop Current. J. Mar. Res., 35, 105-128.

Niiler, P. P., and W. S. Richardson, 1973: Seasonal variability of the Florida Current. J. Mar. Res., 31, 144-167.

Nowlin, W. D., 1972: Winter circulation patterns and property distributions. In Contributions on the Physical Oceanography of the Gulf of Mexico, Vol. II. L.R.A. Capurro and J. L. Reid, eds., Gulf Publishing Co., Houston, Texas, 3-51.

O'Brien, J. J. and H. E. Hurlburt, 1972: A numerical model of coastal upwelling. J. Phys. Oceanogr., 2, 14-26.

Paskausky, D. F. and R. O. Reid, 1972: A barotropic prognostic numerical circulation model. In Contributions on the Physical Oceanography of the Gulf of Mexico, Vol. II, L.R.A. Capurro and J. L. Reid, eds., Gulf Publishing Co., Houston, Texas, 163-176.

Philander, S. G. H., 1976: Instabilities of zonal equatorial currents. J. Geophys. Res., 81, 3725-3735.

Reid, R. O., 1972: A simple dynamic model of the Loop Current. In Contributions on the Physical Oceanography of the Gulf of Mexico, Vol. II. L.R.A. Capurro and J. L. Reid, eds., Gulf Publishing Co., Houston, Texas, 157-159.

Rhines, P., 1977: The dynamics of unsteady currents. The Sea, Vol. 6. E. D. Goldberg, I. N. McCave, J. J. O'Brien, and J. H. Steele, eds., Wiley Interscience, New York, 189-318.

Schlitz, R. J., 1973: Net total transport and net transport by water mass

categories for the Yucatan Channel based on data for April, 1970. Ph.D.

Dissertation. Texas A&M University, College Station. 107 pp.

Sturges, W. A. and J. P. Blaha, 1976: A western boundary current in the Gulf of Mexico. Science, 192, 367-369.

Wert, R. T., and R. O. Reid, 1972: A baroclinic prognostic numerical circulation model. In Contributions to the Physical Oceanography of the Gulf of Mexico, Vol. II. L.R.A. Capurro and J. L. Reid, eds., Gulf Publishing Co., Houston, Texas, 177-210.

FIGURE LEGENDS

- Fig. 1 Topography of the 22°C isothermal surface, August 4 to 18, 1966 (Alaminos cruise 66-A-11) from Leipper (1970). Subsequent data (Elliot, 1979) indicates that an anticyclonic eddy separated from the Loop Current within several months.
- Fig. 2 Bathymetry of the Gulf of Mexico based on U. S. Coast and Geodetic Survey Chart 1007 and soundings on file at the Department of Oceanography, Texas A&M University. From Nowlin (1972). The rectangle shows the approximate domain of the numerical model. The locations of the inflow and outflow ports are also indicated.
- Fig. 3 Bathymetry of the idealized Gulf of Mexico model. The deepest water is at 3000 m and the shallowest topography is 400 m deep. The contour interval is 500 m.
- Fig. 4 Sequence of snapshots of the PHA (pycnocline height anomaly) at 70 day intervals showing the life cycle of an eddy starting at day 2210. The contour interval is 20 m. In all the figures dashed contours are negative. PHA is positive downward. The case shown here uses the parameters of Table 1 and the topography of Fig. 3, except that the upper layer inflow transport is 25 Sv, the lower 5 Sv.
- Fig. 5 PHA vs. time 190 km west of the center of the inflow port for 3 cases: (a) case shown in Fig. 4 which includes topography, (b) standard two-layer flat bottom case using parameters from Table 1, (c) standard reduced gravity case using appropriate parameters from Table 1. A regular progression of eddies

through the north-south cross-section is shown in each case.

The contour interval is 30 m.

- Fig. 6 FSA (free surface anomaly, positive upward) at 5 cm contour intervals for a two-layer flat bottom case using parameters from Table 1 except that $\beta=0$ and the inflow is angled 27° west of normal. The solution evolves to the steady state shown here at day 1080.
- Fig. 7 Snapshots of PHA at 60 day intervals beginning at day 1320 for the standard reduced gravity case after β was reduced to zero with a time constant of 10 days starting at day 1300. The westward spreading of the Loop Current has been halted and the eddy shedding process appears frozen. The contour interval is 20 m.
- Fig. 8 PHA for (a) the mean over 3 eddy cycles for the standard reduced gravity case, (b) the deviations from the mean at day 1800, (c) a steady state reduced gravity solution (day 1800) obtained by increasing the eddy viscosity of the standard case to $A = 3 \times 10^7 \text{ cm}^2 \text{ sec}^{-1}$, and (d) the steady state linear solution (day 1080) corresponding to the standard case, obtained using an inflow transport of .1 Sv. The contour interval is 20 m for (a), (b), and (c). In (d) both inflow transport and contour interval were reduced by a factor of 200.
- Fig. 9 FSA for 4 barotropic flat bottom experiments. The appropriate parameters from Table 1 were used except in (a) depth = 200 m, inflow = 10 Sv, (b) depth = 300 m, inflow = 20 Sv, (c) depth = 300 m, inflow = 25 Sv, (d) depth = 300 m, inflow = 30 Sv. The contour interval is 5 cm. Snapshots are at (a) day 720 (b) day

710, (c) day 720, (d) day 1080. In panel (a) the solution is steady.

Fig. 10 Snapshots of PHA at 20 day intervals starting at day 1300 for the standard two-layer flat bottom case except $A = 3 \times 10^6 \text{ cm}^2 \text{ sec}^{-1}$. The model domain has been extended 160 km eastward to include a representation of the Florida Straits. The contour interval is 20 m.

Fig. 11 Kinetic energy in the rectangular part of the basin as a function of time for each layer (upper curve for upper layer) for 3 cases: (a) standard two-layer flat bottom case except $A = 3 \times 10^6 \text{ cm}^2 \text{ sec}^{-1}$ and the domain of Fig. 10 is used, (b) standard two-layer flat bottom case, (c) standard reduced gravity case except $A = 3 \times 10^6 \text{ cm}^2 \text{ sec}^{-1}$. In case (c) the upper curve is potential energy. The value of IC is (a) .7, (b) .5, (c) 5.5.

Fig. 12 Panels (a) and (b) are snapshots of PHA at extremes of an eddy cycle (days 1050 and 1080) when the standard two-layer flat bottom model has inflow 27° west of normal and the lower layer inflow is reduced to zero. Panel (c) is PHA vs time for this case at a longitude 190 km west of the center of the inflow port. The contour interval is 20 m.

Fig. 13 Kinetic energy in the basin vs time for (a) the case shown in Fig. 12. The upper curve is for the upper layer and the lower curve for the lower layer; (b) is for the corresponding reduced gravity case. The value of IC is (a) .55, (b) .9.

Fig. 14 Potential energy spectral densities vs. frequency at a given

location in the basin for 4 cases: (a) the standard two-layer flat bottom case at $x = 1010$ km, $y = 366$ km, (b) the reduced gravity case with $A = 3 \times 10^6 \text{ cm}^2 \text{ sec}^{-1}$ at $x = 1010$ km, $y = 366$ km, (c) the two-layer flat bottom case with $A = 3 \times 10^6 \text{ cm}^2 \text{ sec}^{-1}$ at $x = 1410$ km, $y = 291$ km, and (d) the two-layer flat bottom case with inflow 27° west of normal confined to the upper layer at $x = 1010$ km, $y = 234$ km. Spectra were computed over an integral number of eddy cycles after the solutions reached statistical equilibrium.

- Fig. 15 North-south section of PHA in meters versus time 190 km west of the center of the inflow port for the reduced gravity model with inflow centered at $x = 1000$ km and outflow centered at $y = 225$ km. The contour interval is 30 m.
- Fig. 16 Snapshots of PHA at day 1080 for (a) the standard reduced gravity case and (b) the case shown in Fig. 15. The contour interval is 20 m.
- Fig. 17 Steady state PHA (day 1080) for the standard reduced gravity model but with a section of land area added east of $x = 1440$ km and north of $y = 187.5$ km. The contour interval is 20 m.
- Fig. 18 Regime diagram for three stability regimes: (E) Eddy-shedding, (W) steady westward-spreading (Fig. 8c, d) and (N) steady source-sink (Figs. 6, 17) as a function of Reynolds number (Re) and beta Rossby number (R_B). Lower case letters refer to barotropic experiments; upper case letters refer to reduced-gravity experiments.
- Fig. 19 Snapshot of PHA at day 1080 (a) and y-t phase plot of PHA 190 km west of the center of the inflow port (b) for the standard reduced gravity model except that the eastern boundary is entirely open and the east-west extent is 1760 km. The contour interval is 20 m for (a) and 30 m for (b).

- Fig. 20 Snapshots of PHA at day 1080 for the standard reduced gravity model with the Yucatan and Florida Straits added; (a) for standard outflow port width, (b) for halved outflow port width and (c) for doubled outflow port width. The contour interval is 20 m. The total domain size is 1760 x 960 km.
- Fig. 21 Energy balances for the three models of Fig. 20 averaged over an eddy-cycle and over the rectangular part of the domain.
- Fig. 22 Snapshot of PHA at day 1080 (a) and y-t phase plot of PHA 190 km west of the center of the inflow port (b) for the standard reduced gravity model with the Yucatan Peninsula represented by a rectangular coastline irregularity. The contour interval is 20 m for (a) and 30 m for (b).
- Fig. 23 Steady-state FSA at day 1080 for (a) the flat bottom barotropic standard experiment and (b) the same experiment with bottom topography of Fig. 3 added. Inflow transport was 30 Sv. The contour interval is 2 cm.
- Fig. 24 Snapshots of PHA at day 1980 for (a) the standard reduced gravity model but with 25 Sv inflow, (b) the flat bottom, two-layer model with parameters identical to (a) and no deep water inflow, and (c) identical to (b) but with bottom topography. The contour interval is 20 m.
- Fig. 25 Phase plots of PHA 390 km west of the center of the inflow port for the three models shown in Fig. 24. The contour interval is 30 m.
- Fig. 26 Results for the full bottom topography experiment with inflow transport $T_1 = 25$ Sv and $T_2 = 0$ until year 6 when T_2 increases

to 10 Sv. (a) Domain-averaged upper-layer (top curve) and lower-layer kinetic energy. IC = 1.5. (b) Steady state PHA at day 2880. The contour interval is 20 m. (c) Lower-layer pressure normalized by density at day 2880. The contour interval is .25 $m^2 sec^{-2}$.

Fig. 27 (a) Bottom topography of the idealized Gulf of Mexico when the Campeche Bank and the bottom slope on the inflow are removed. The deepest water is 3000 m and the shallowest water is 400 m. The contour interval is 200 m. (b) Domain-averaged upper-layer (top curve) and lower-layer kinetic energy for this experiment. $T_1 = 25$ Sv and T_2 was increased from 0 to 10 Sv after 3 years. IC = .95.

Fig. 28 Steady-state results (day 1080) for the experiment shown in Fig. 27. (a) Bottom topography (dashed) contoured at 250 m intervals and depth of the interface (solid) contoured at 20 m intervals in a 500 x 500 km section in the southeast corner of the model. (b) Contours of $h_1 \nabla \cdot \vec{v}_1$. (c) Contours of $\vec{v}_1 \cdot \nabla h_1$. (d) Contours of $(g/f) J(n_2, n_1)$. The contour interval in b - d is $30 (x 10^{-4} cm sec^{-1})$.

Fig. 29 Steady-state (day 1080) mass transport vorticity term balances for the experiment shown in Fig. 27 at $y = 168.75$ km across the Loop Current from $x = 1000$ km to $x = 1600$ km for (a) upper layer, (b) lower-layer, and (c) the sum of (a) and (b). From equations (21-23): diffusion (solid), planetary vorticity advection (long dashes), pressure torques (short dashes), and nonlinear terms (dots on solid).

Fig. 30 Potential energy spectral densities versus frequency for the standard reduced gravity model at $x = 810$ km, $y = 421.9$ km with (a) steady forcing and, superimposed on the mean (b) an annual forcing, (c) an eight-month period forcing, and (d) a semi-annual period forcing. The mean transport was 20 Sv; the sinusoidally-varying amplitude was 10 Sv peak to peak. Spectra were computed over an integral number of eddy cycles after the solutions reached statistical equilibrium.

Fig. 31 Phase plots of PHA 390 km west of the center of the inflow port for (a) the eight-month period forcing experiment and (b) the semi-annual period forcing experiment. The contour interval is 30 m.

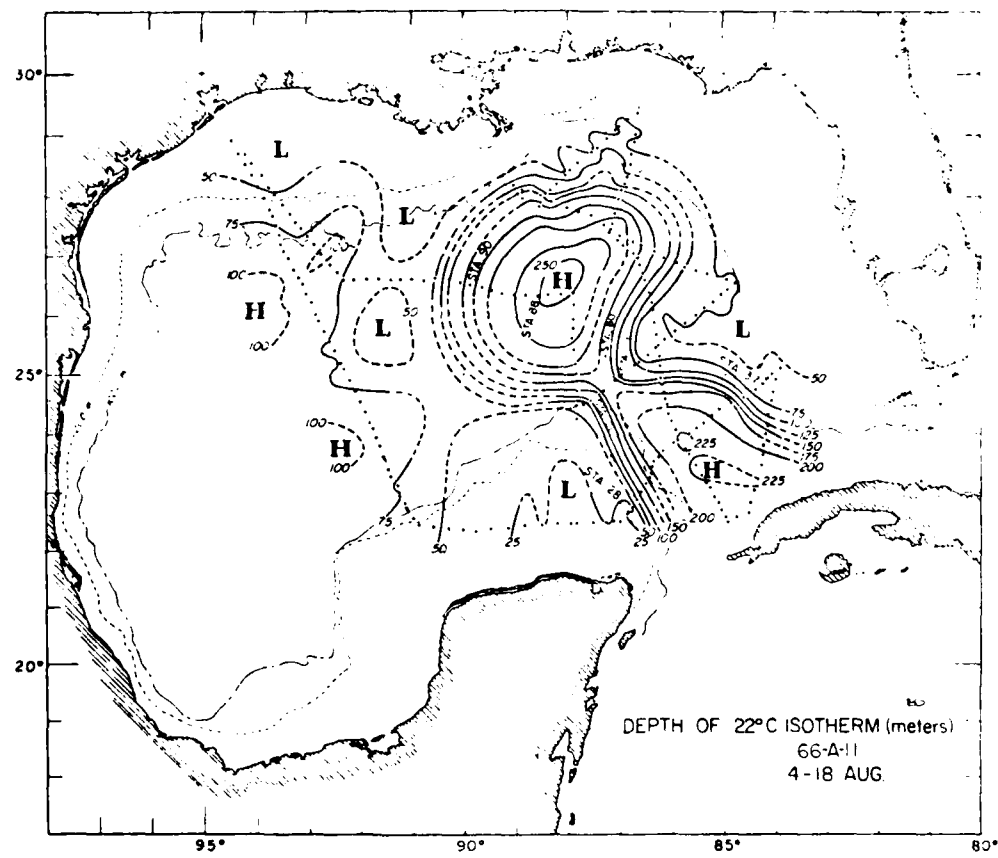


FIGURE 1

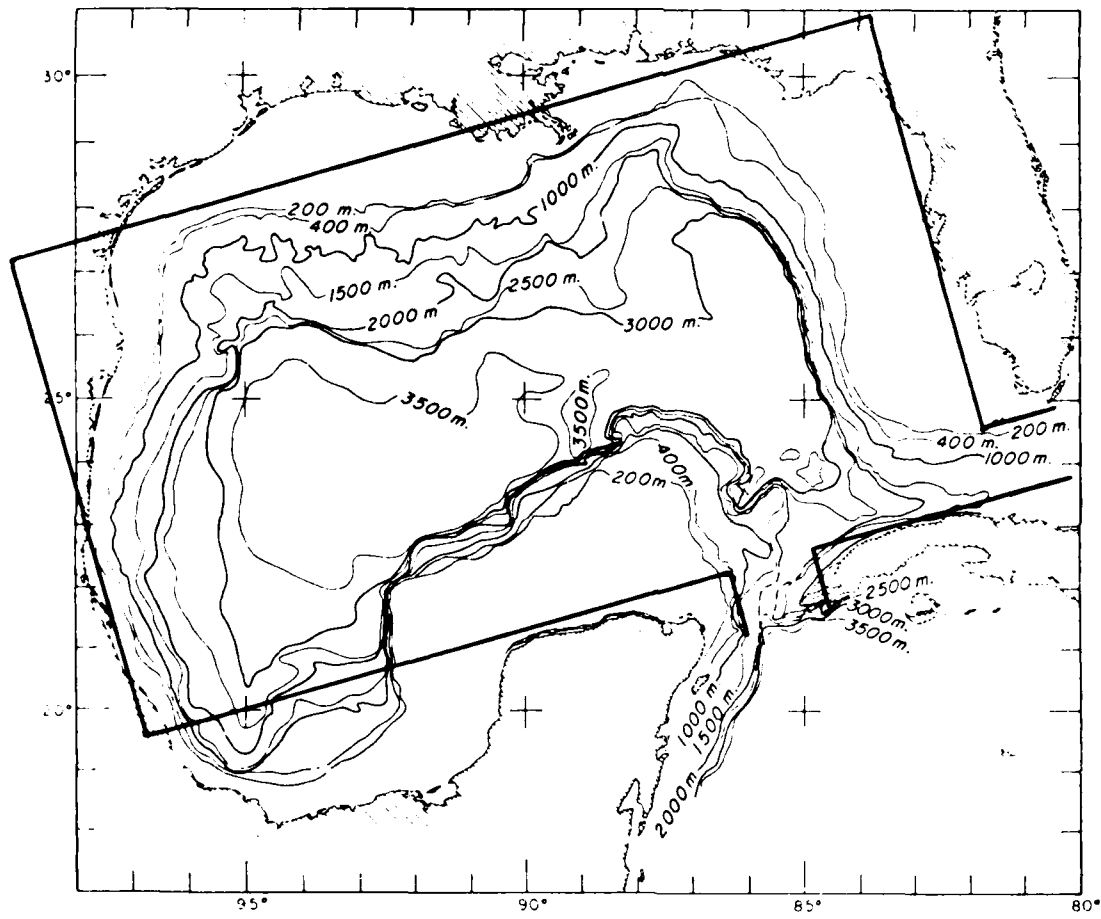


FIGURE 2

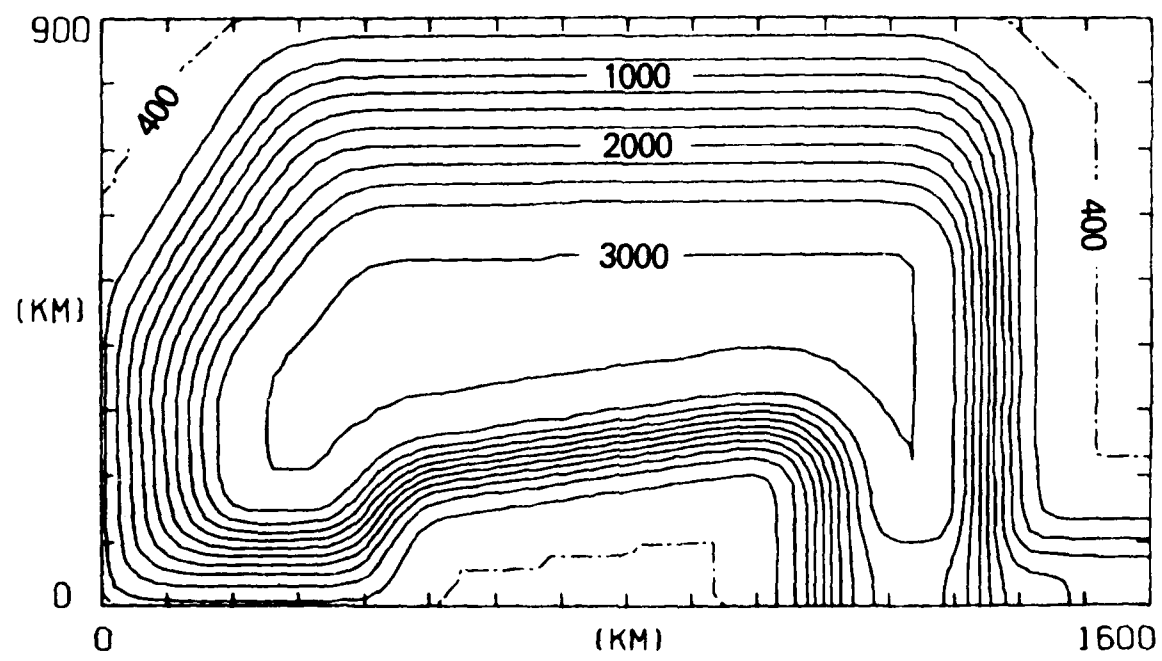


FIGURE 3

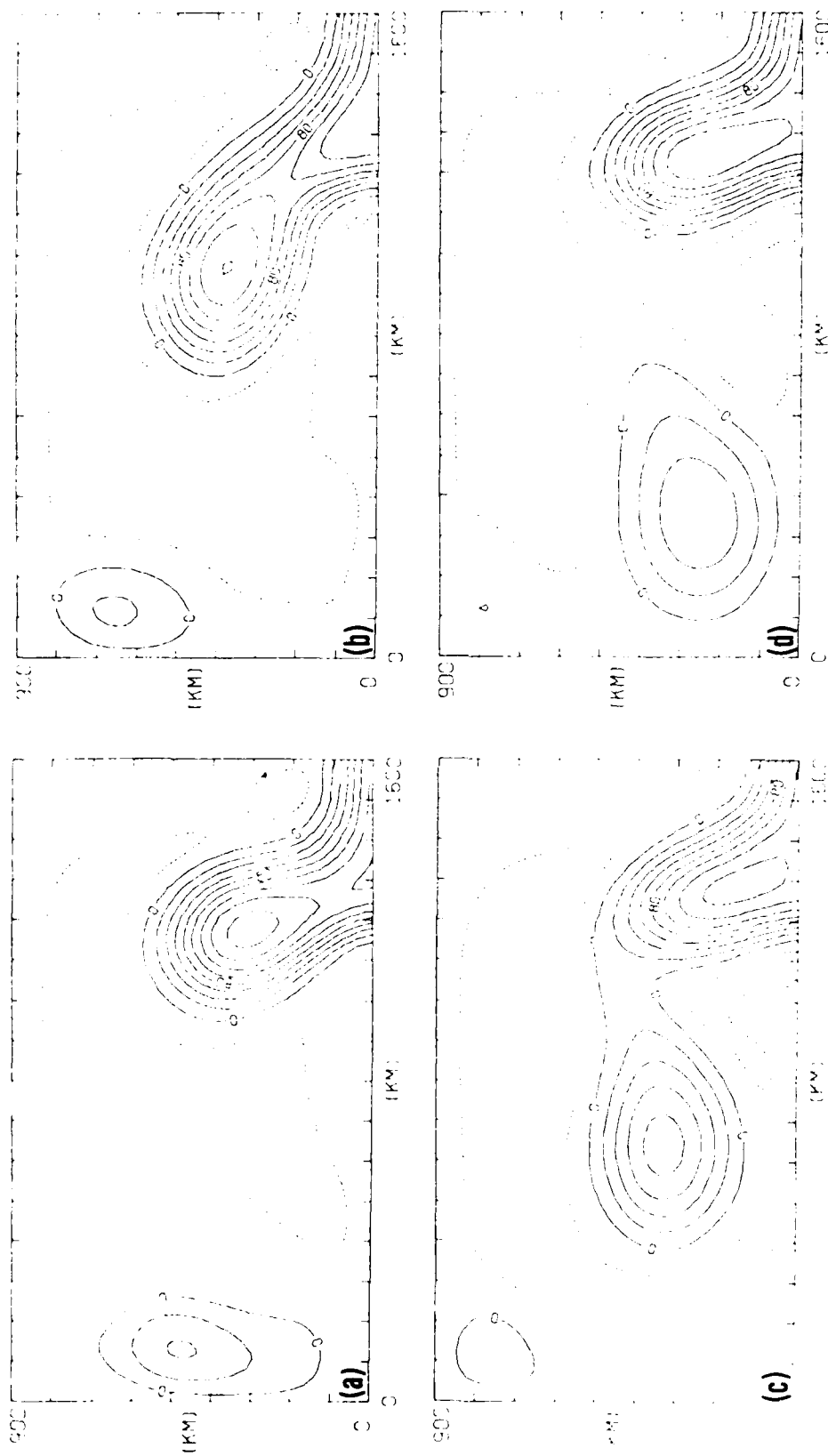


FIGURE 4

AD-A118 350 NAVAL OCEAN RESEARCH AND DEVELOPMENT ACTIVITY NSTL S--ETC F/G 8/3
A NUMERICAL STUDY OF LOOP CURRENT INTRUSIONS AND EDDY SHEDDING. (U)
JUN 80 H E HURLBURT, J D THOMPSON

UNCLASSIFIED NORDA-TN-64

NL

2 of 2

AD A
118350

END
DATE
FILED
09-82
DTIC

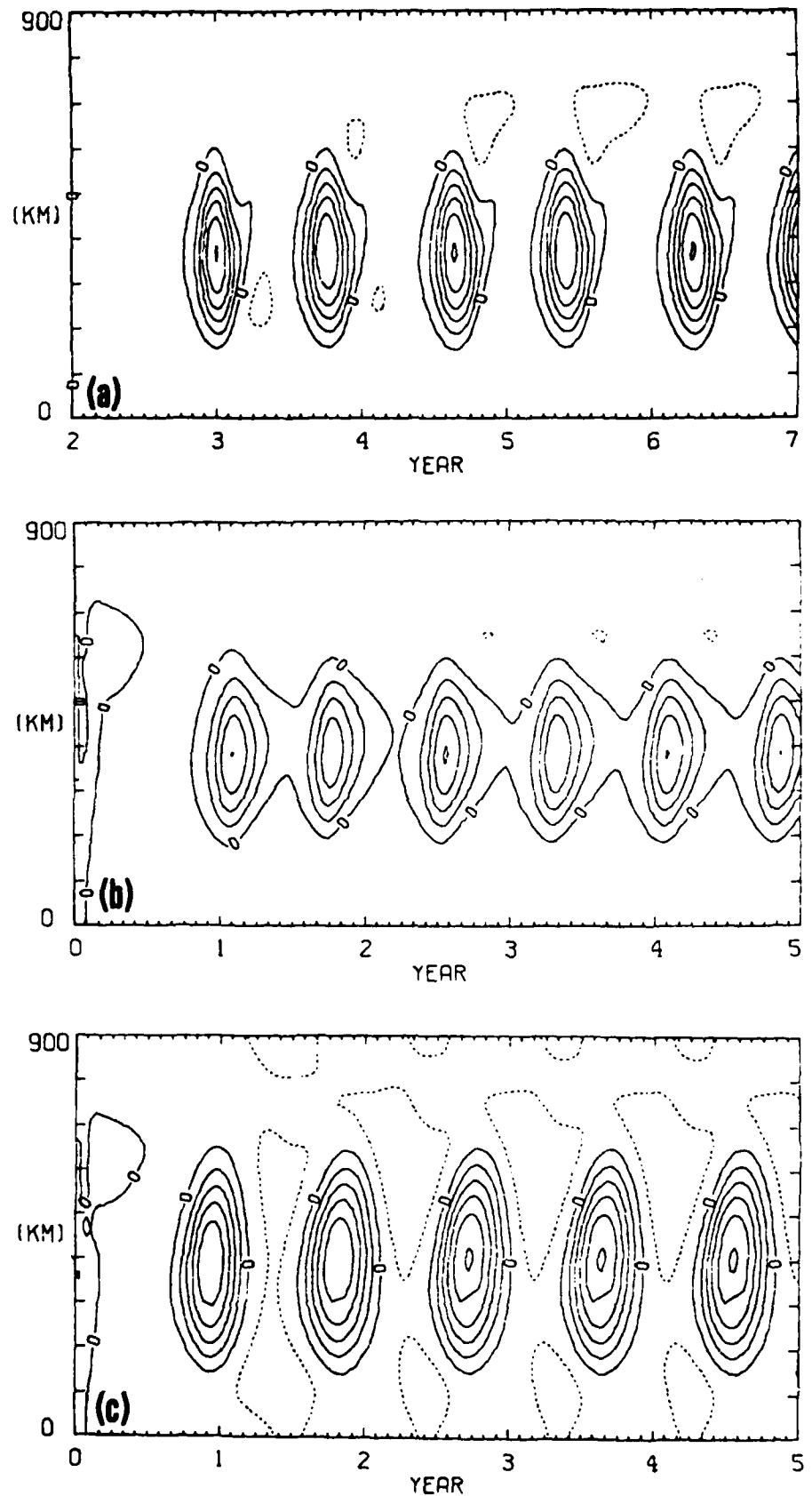


FIGURE 5

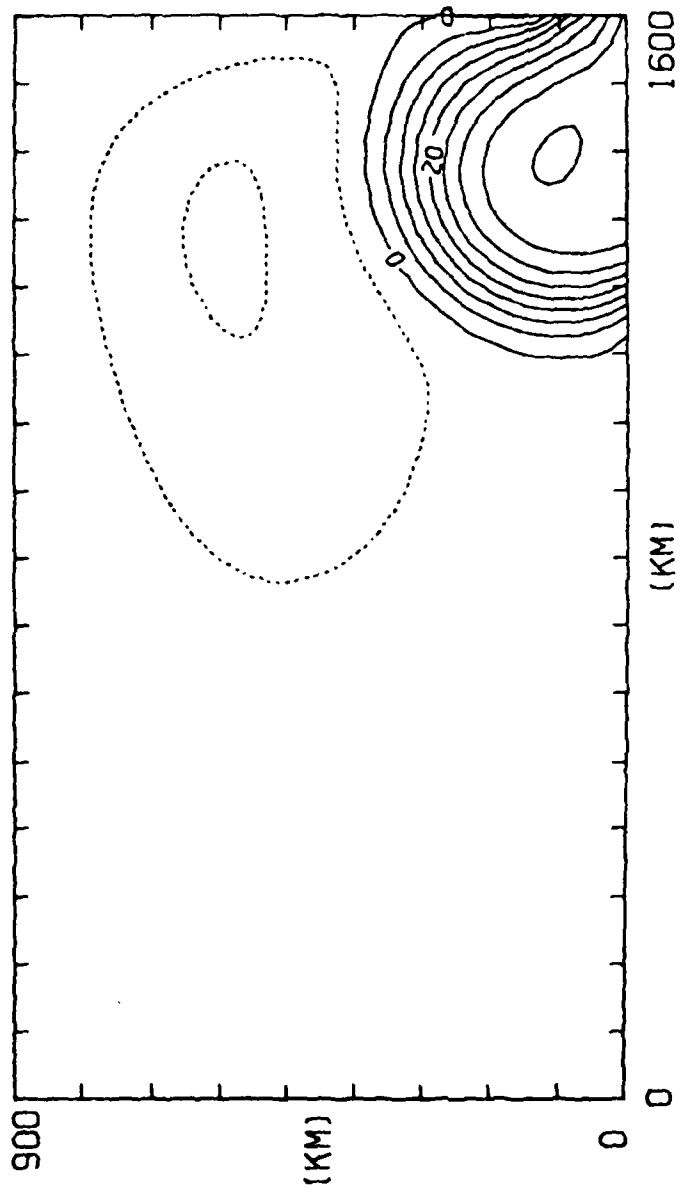


FIGURE 6

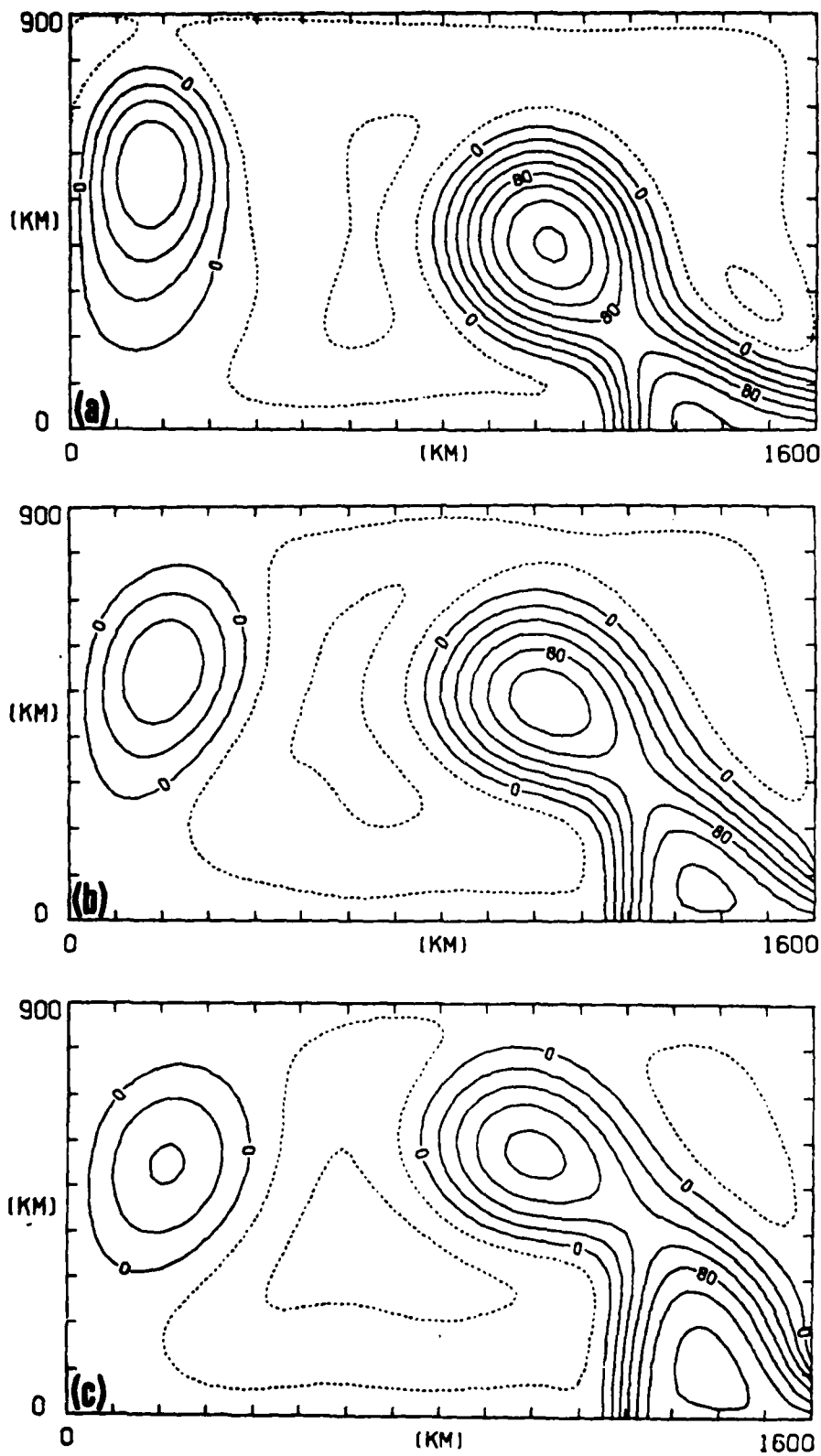


FIGURE 7

FIGURE 2

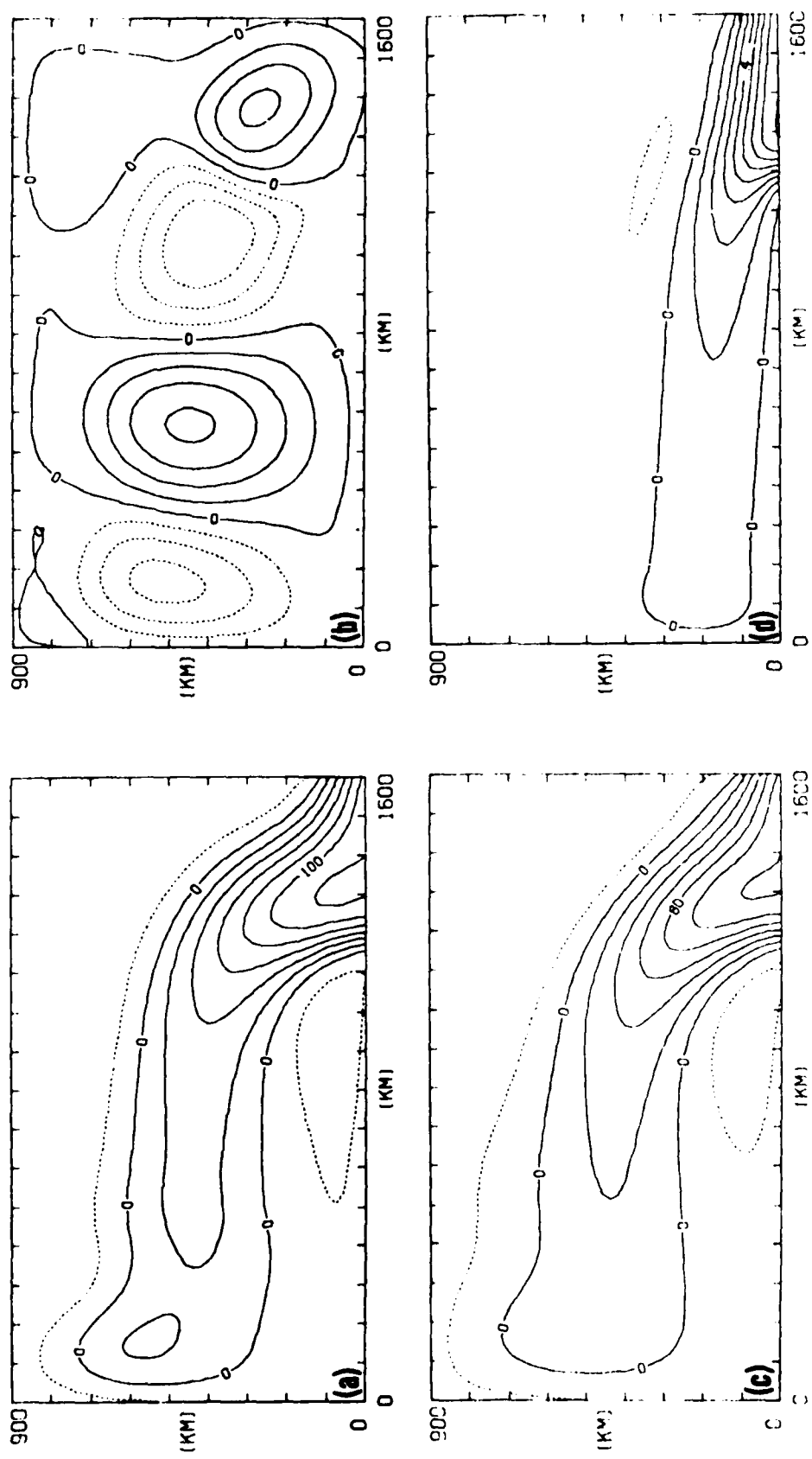
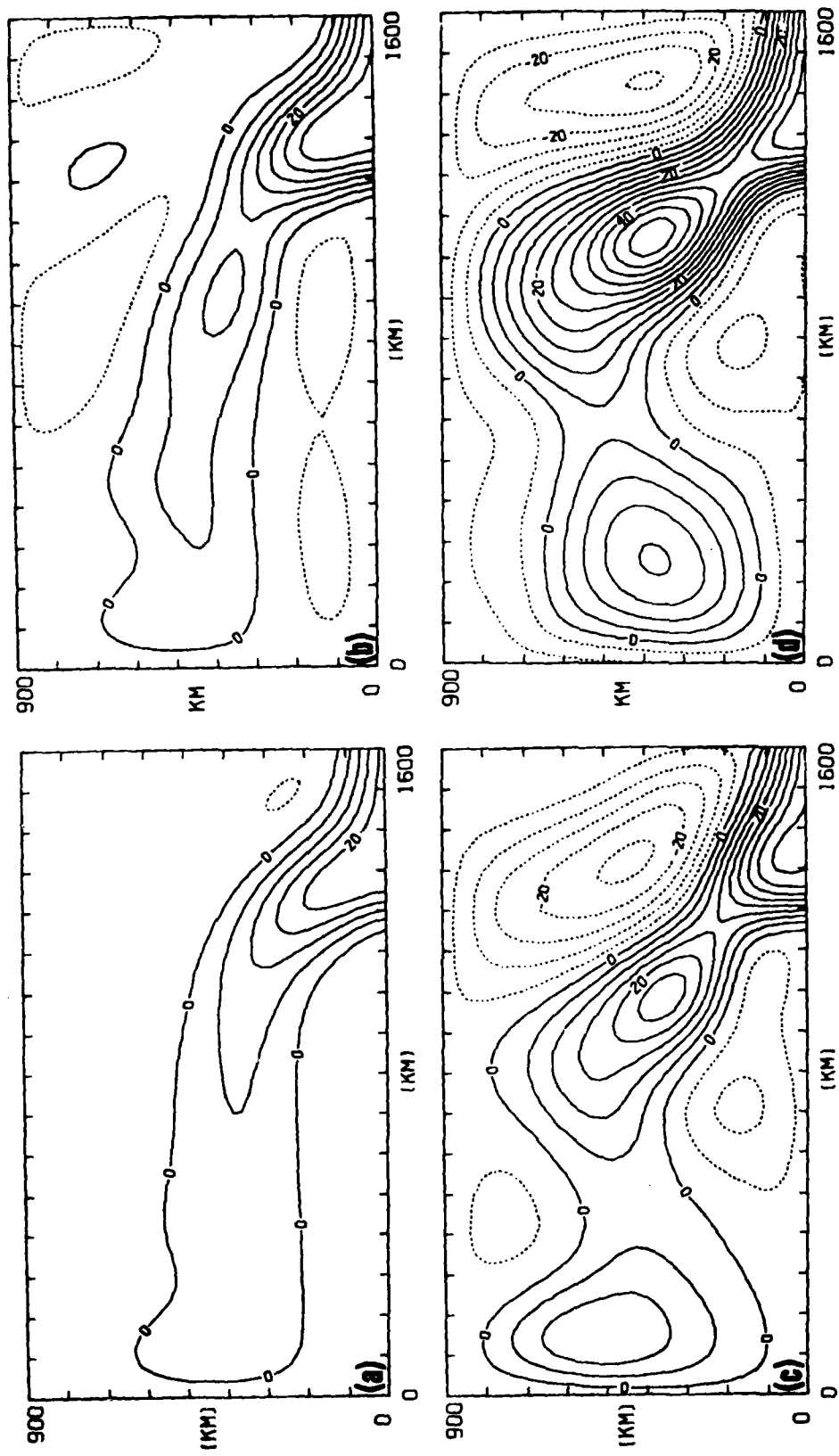


FIGURE 9



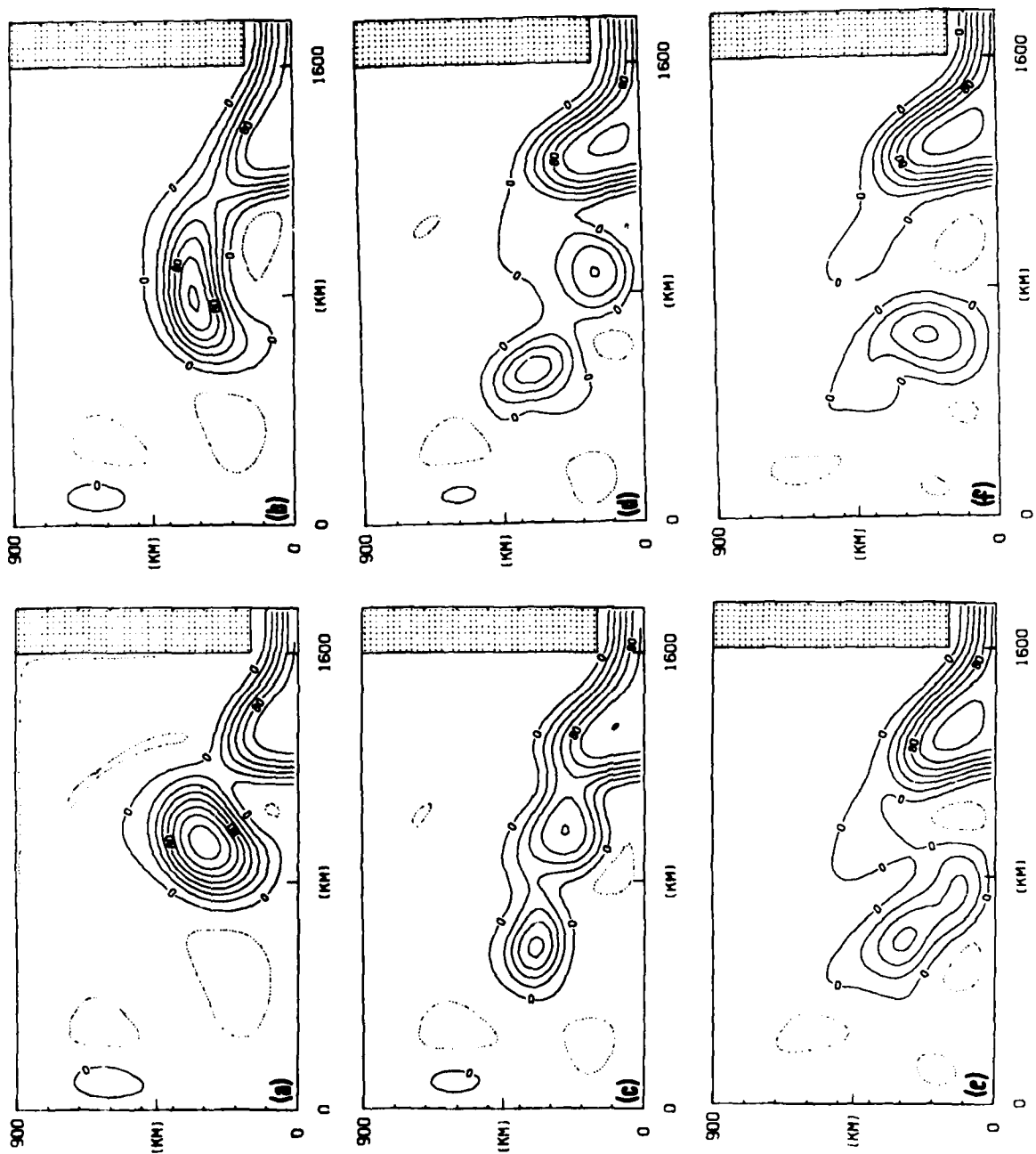


FIGURE 10

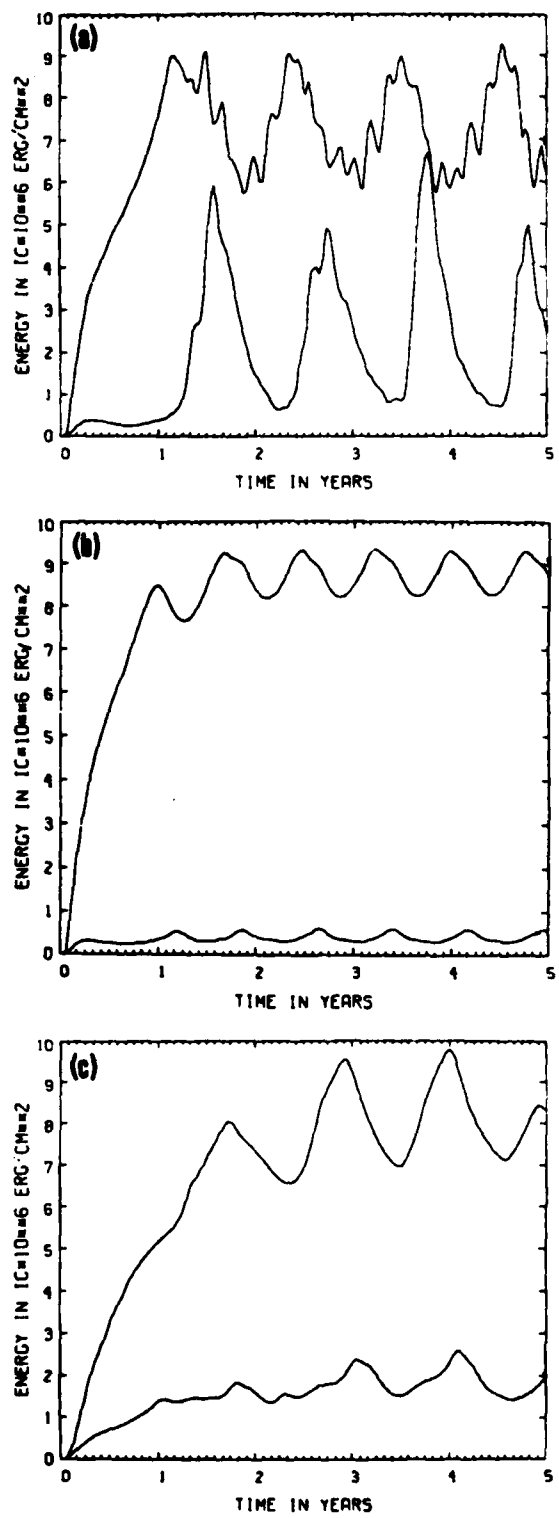


FIGURE 11

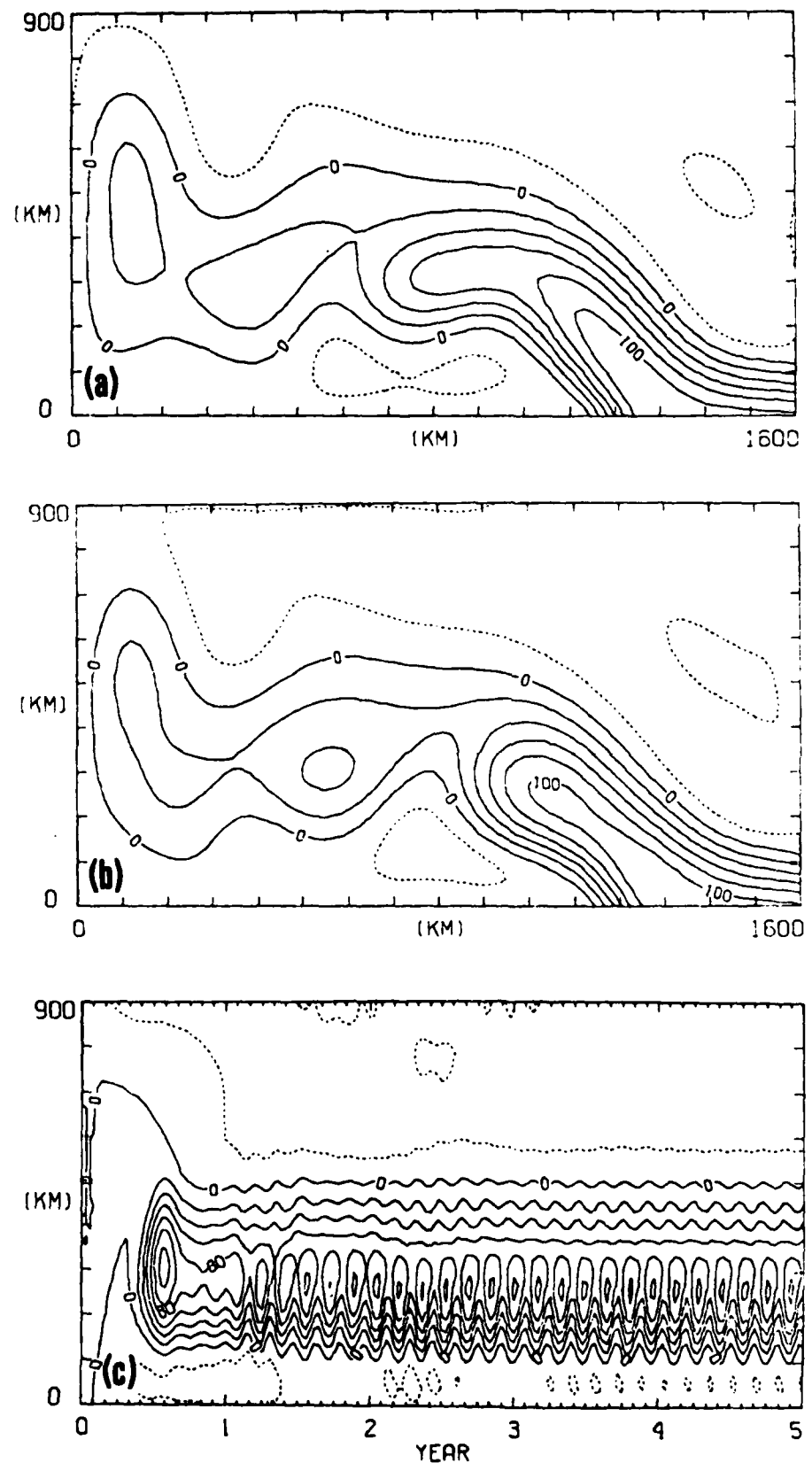


FIGURE 12

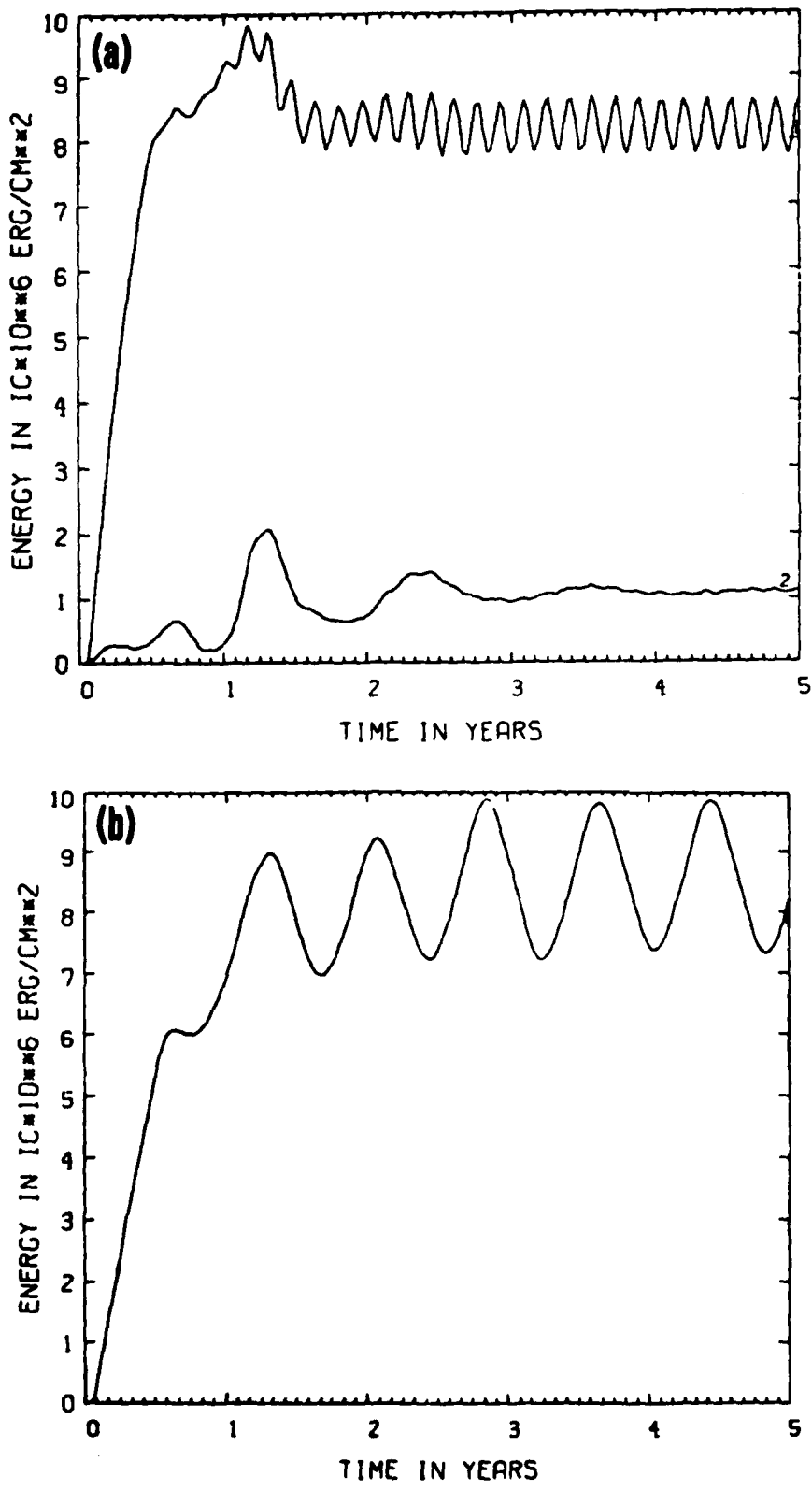


FIGURE 13

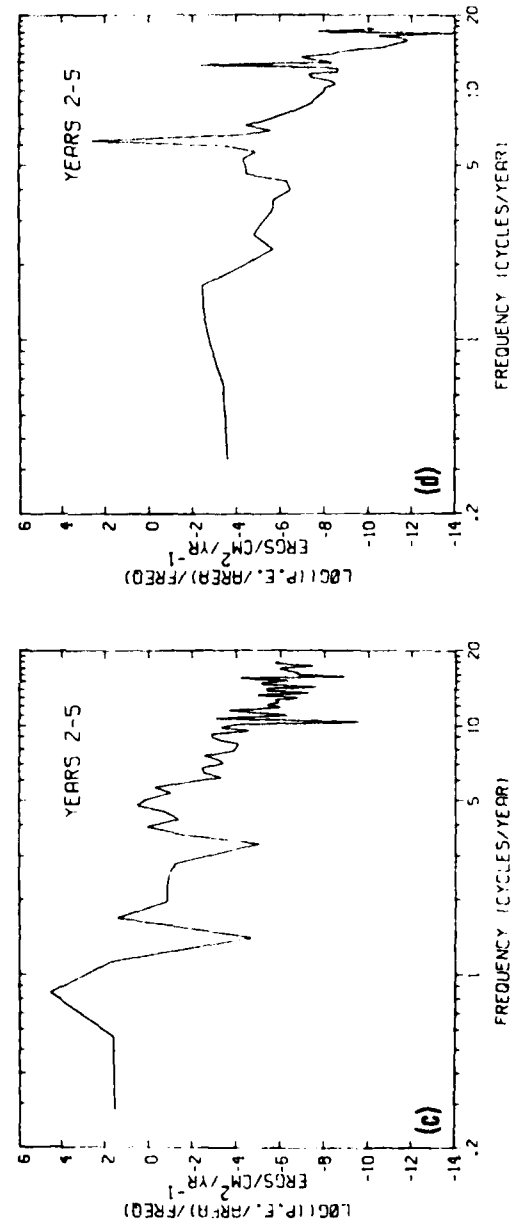
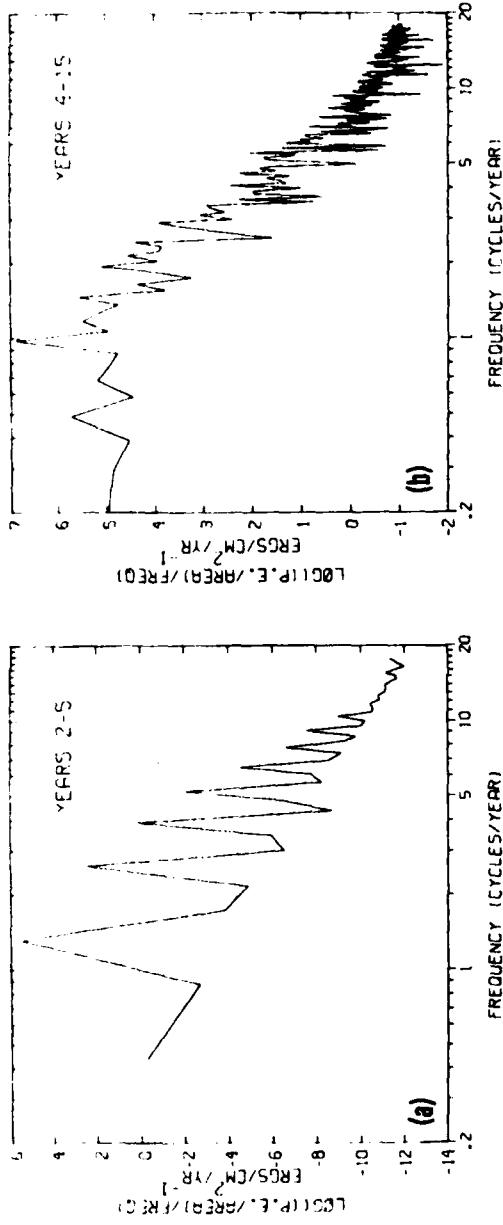
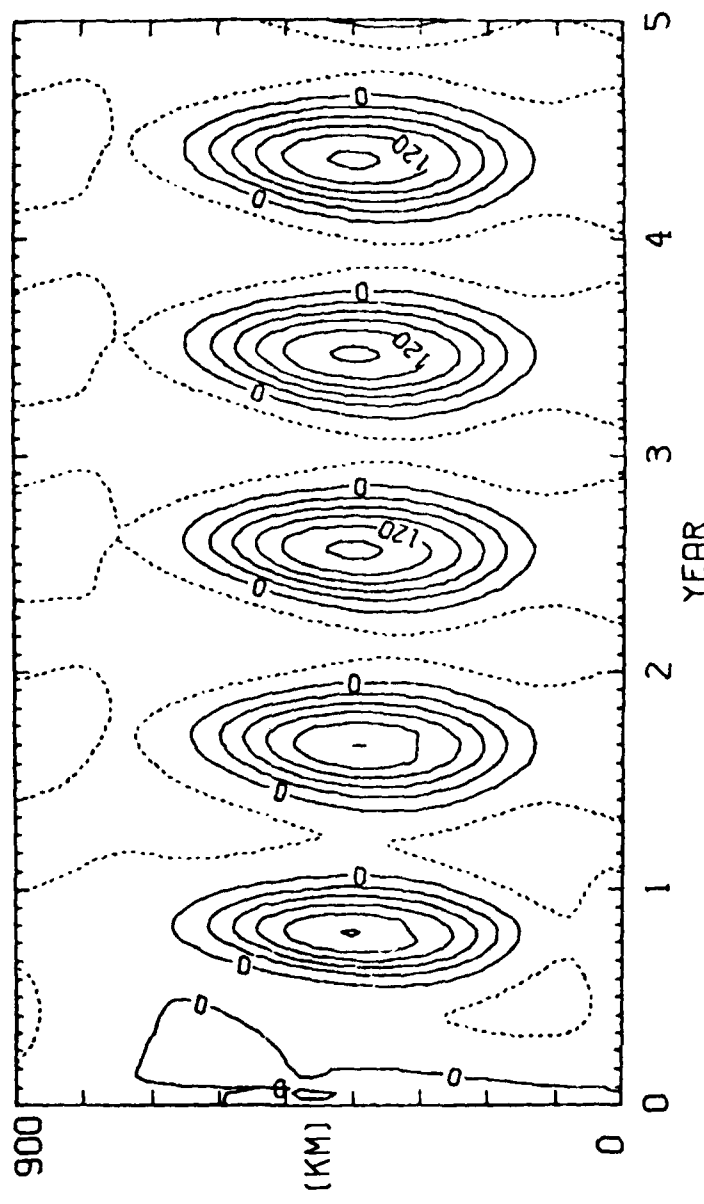


FIGURE 14

FIGURE 15



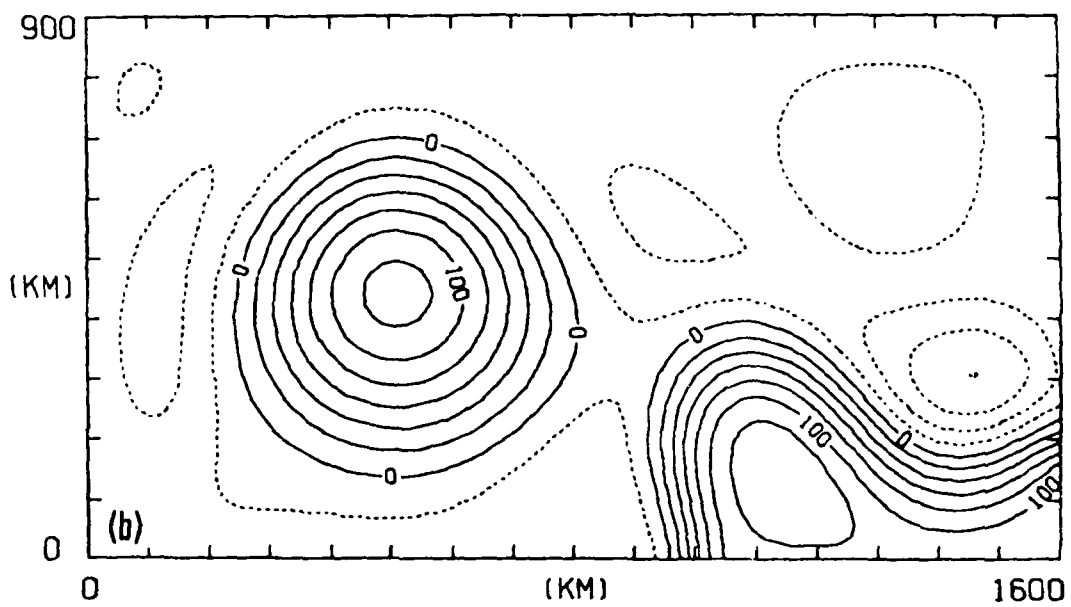
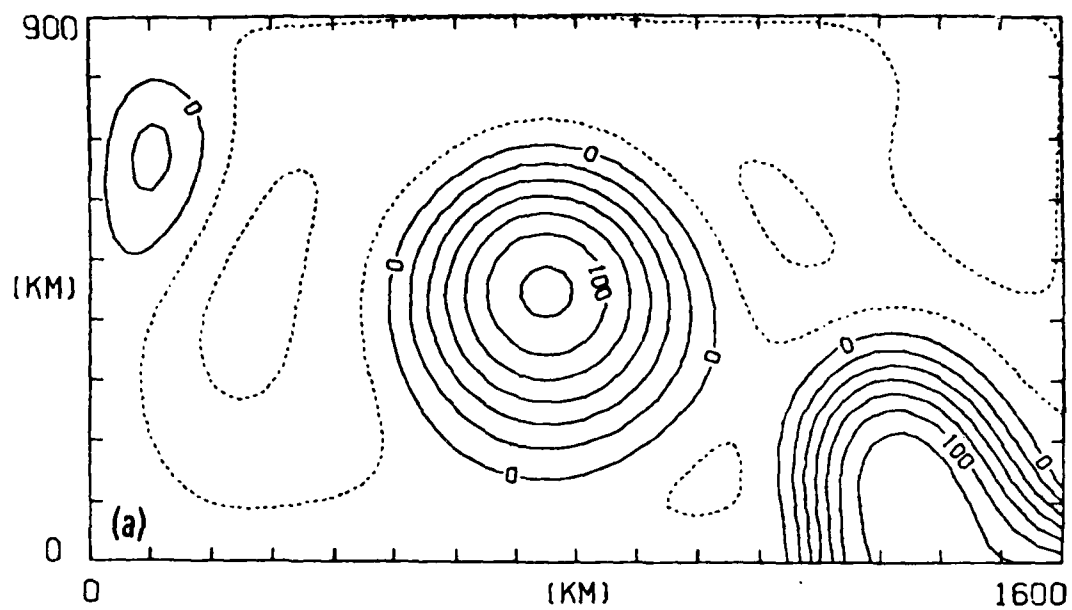


FIGURE 16

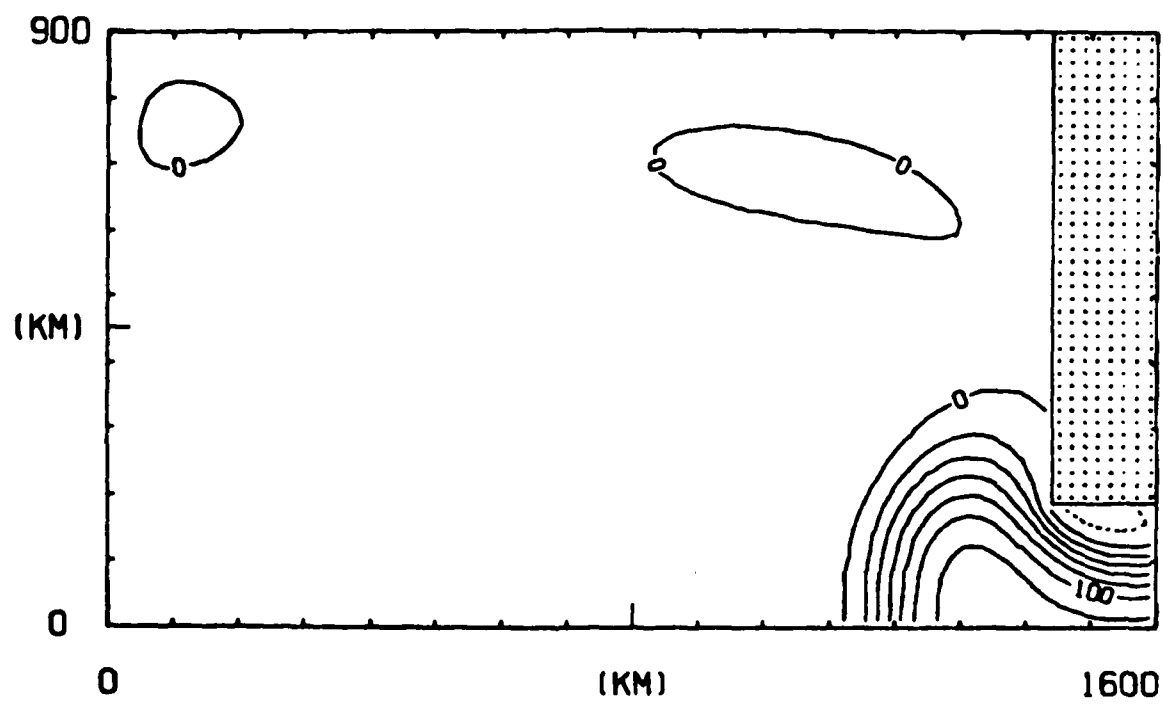


FIGURE 17

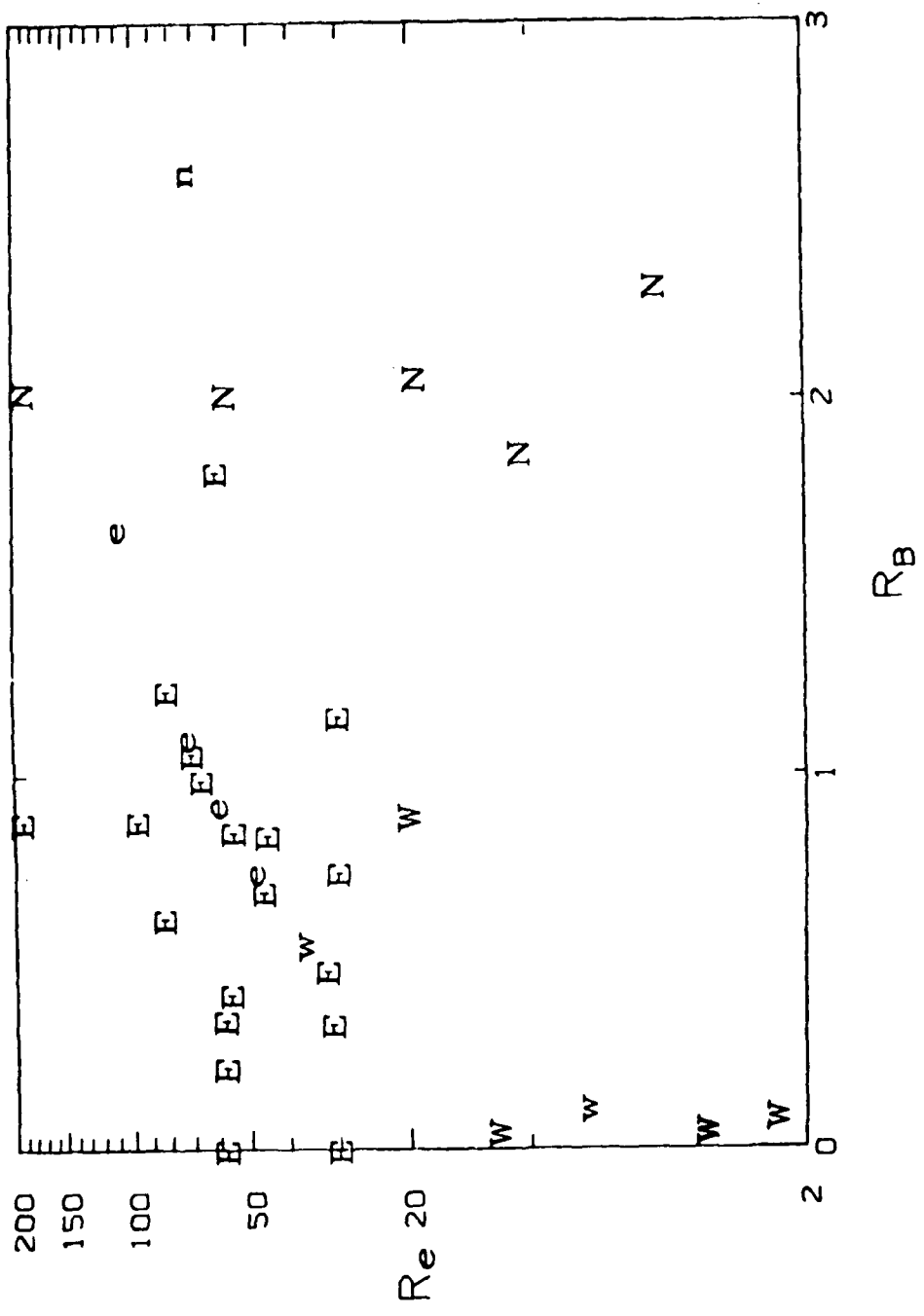


FIGURE 18

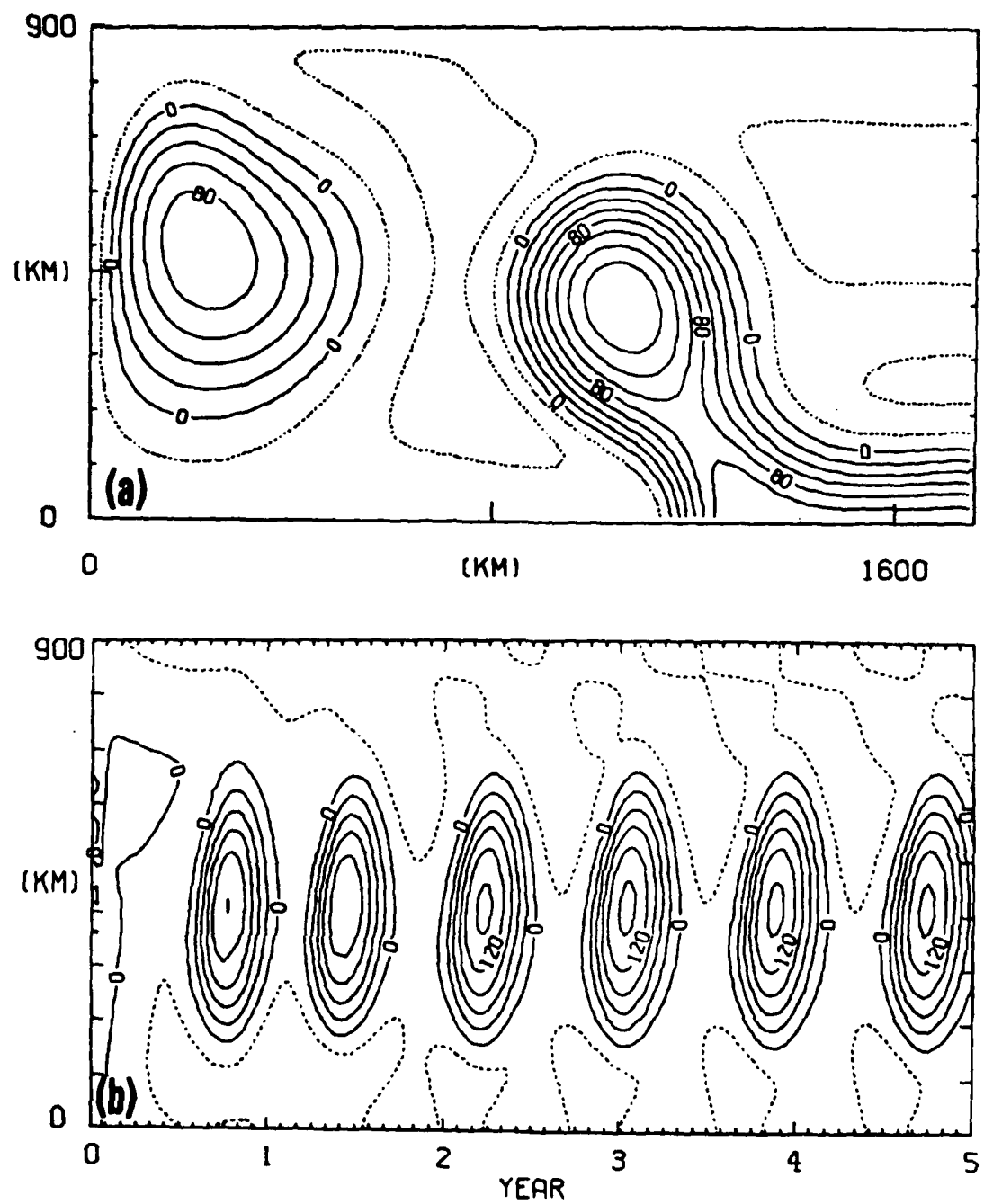


FIGURE 19

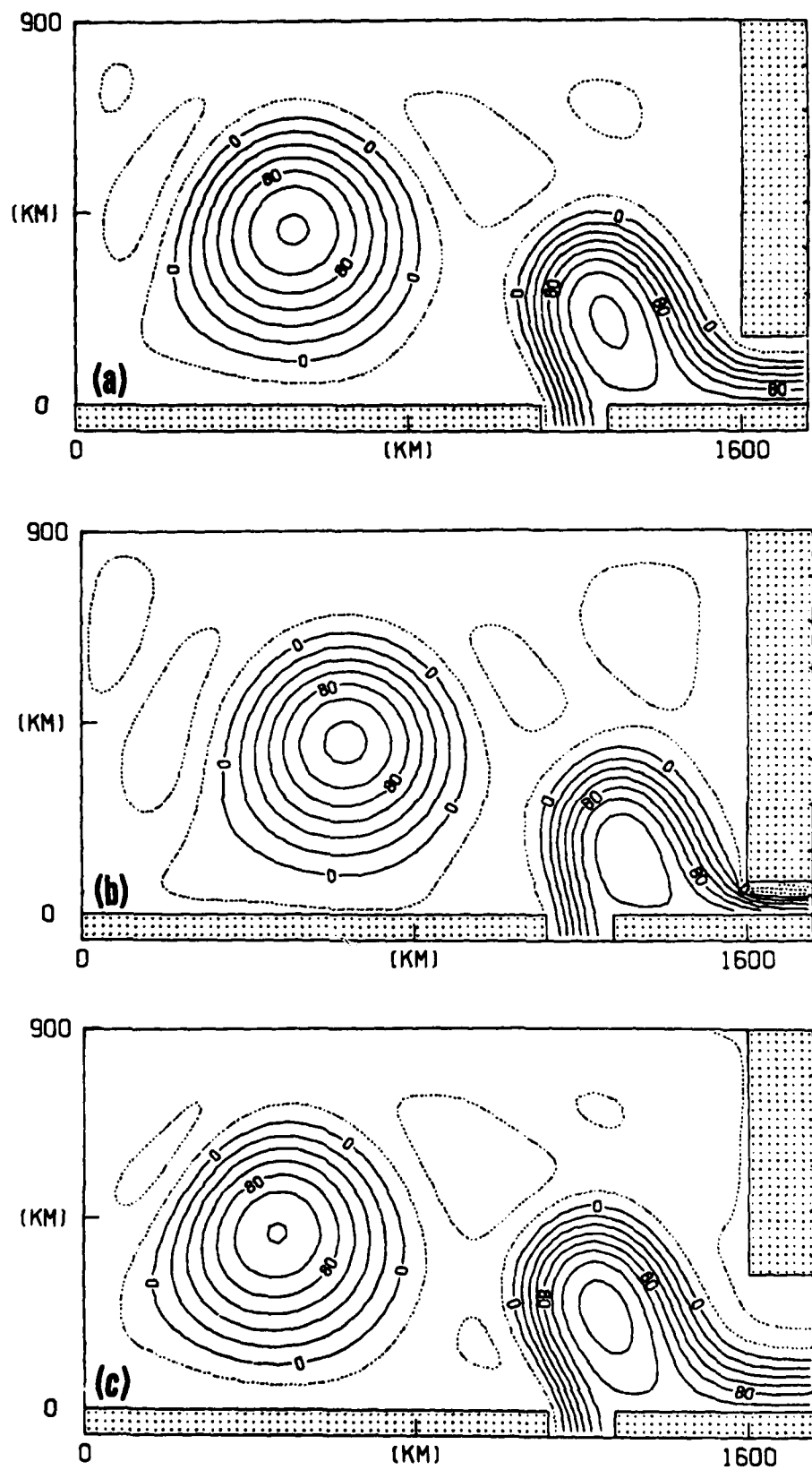


FIGURE 20

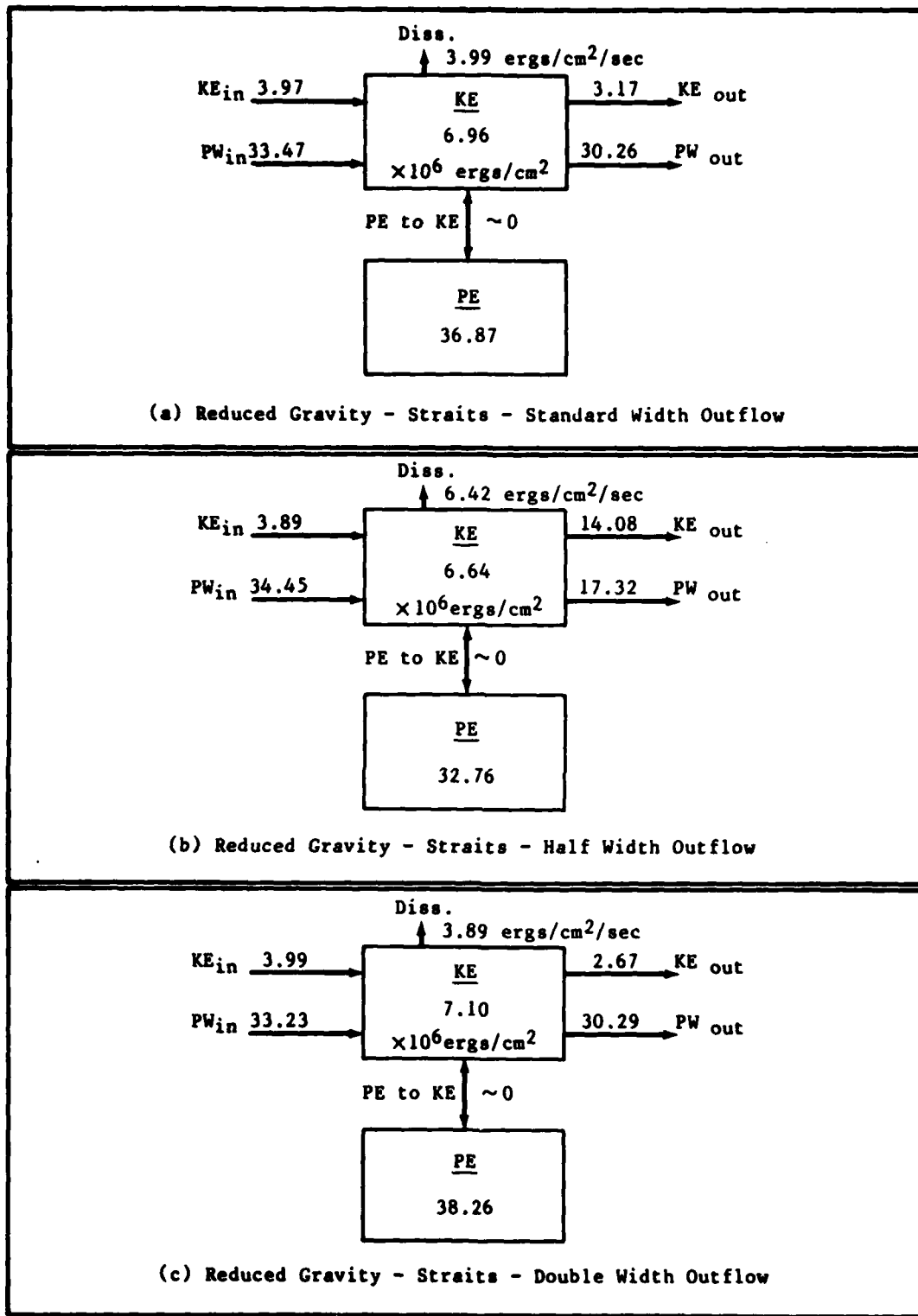


FIGURE 21

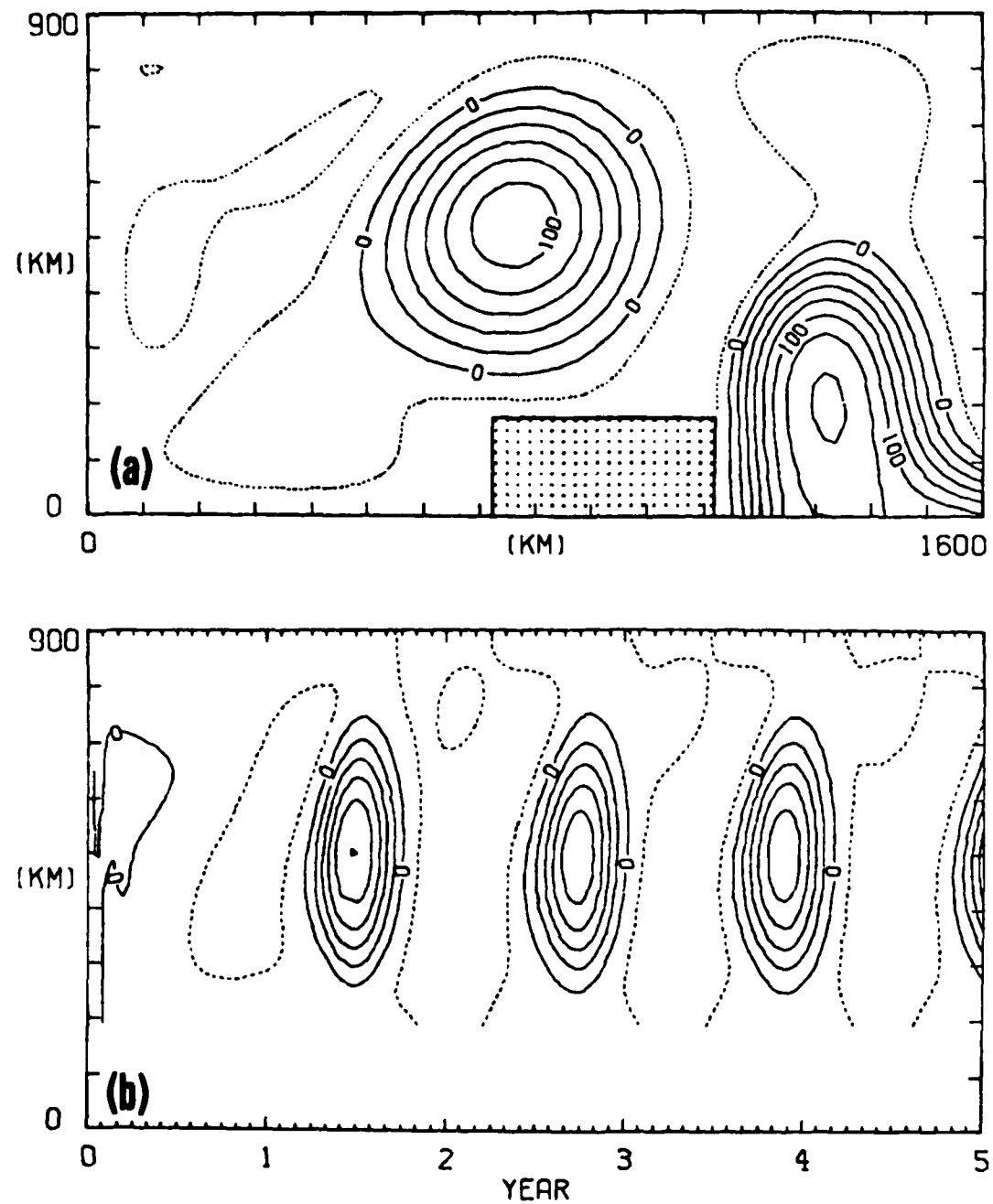


FIGURE 22

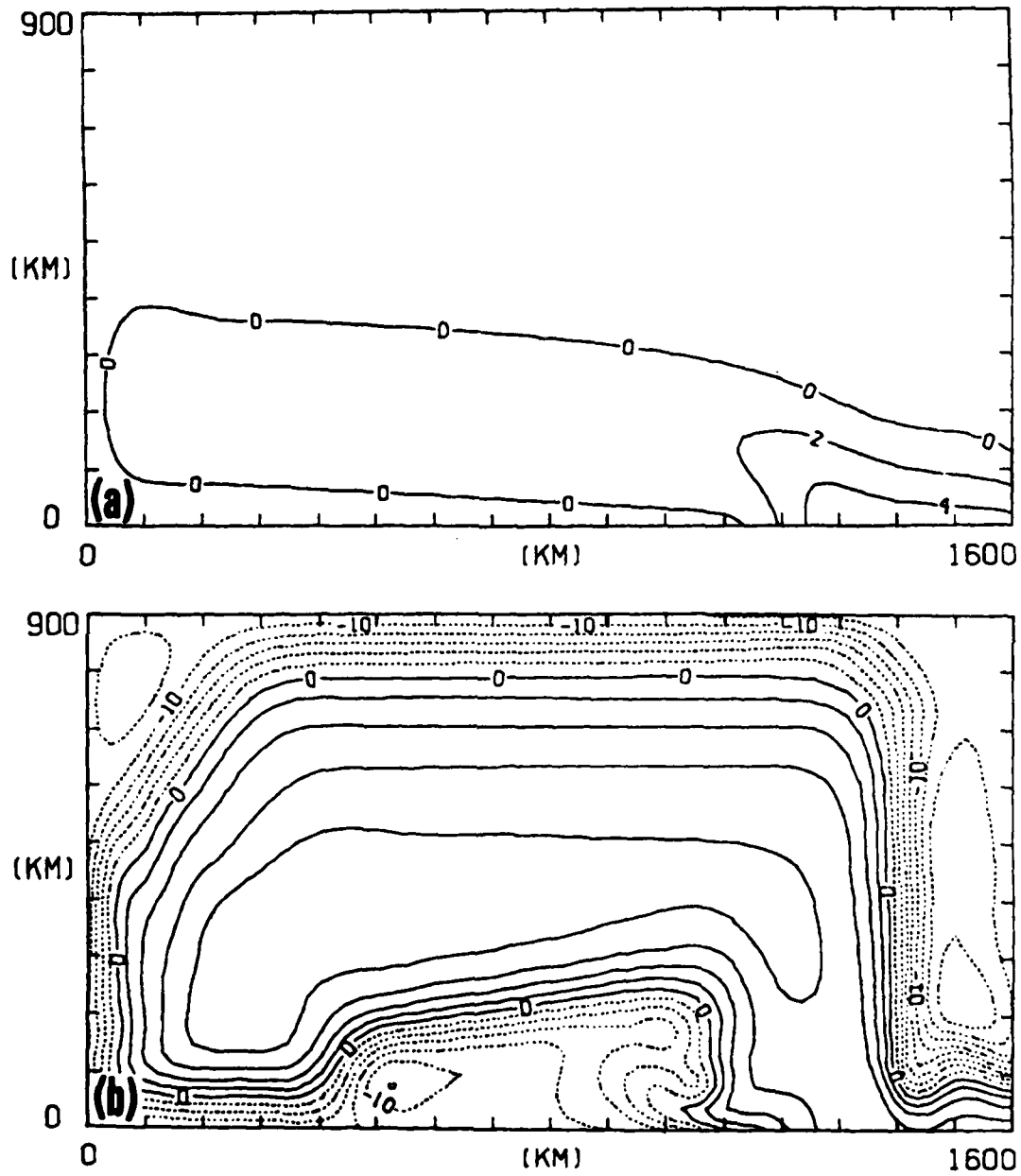


FIGURE 23

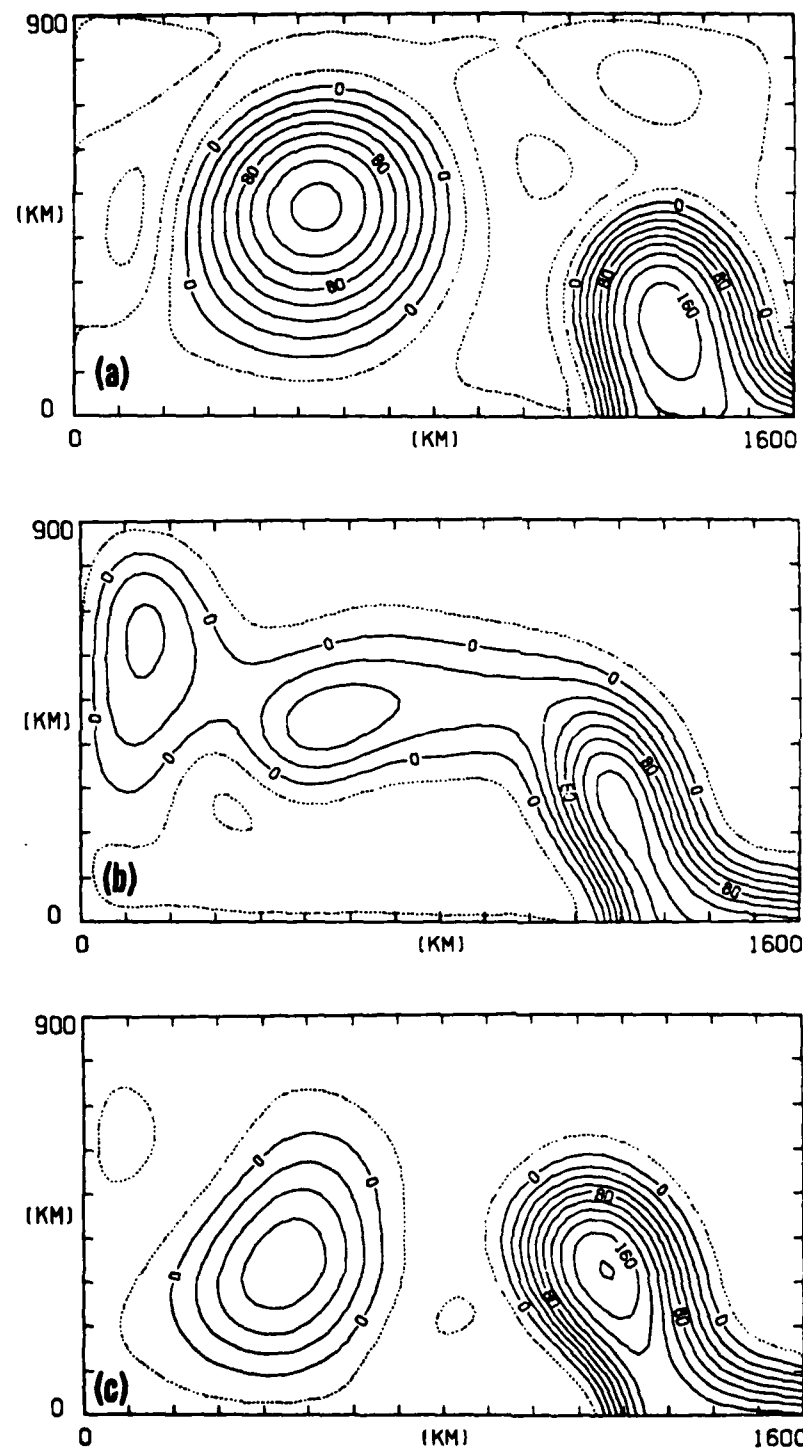


FIGURE 24

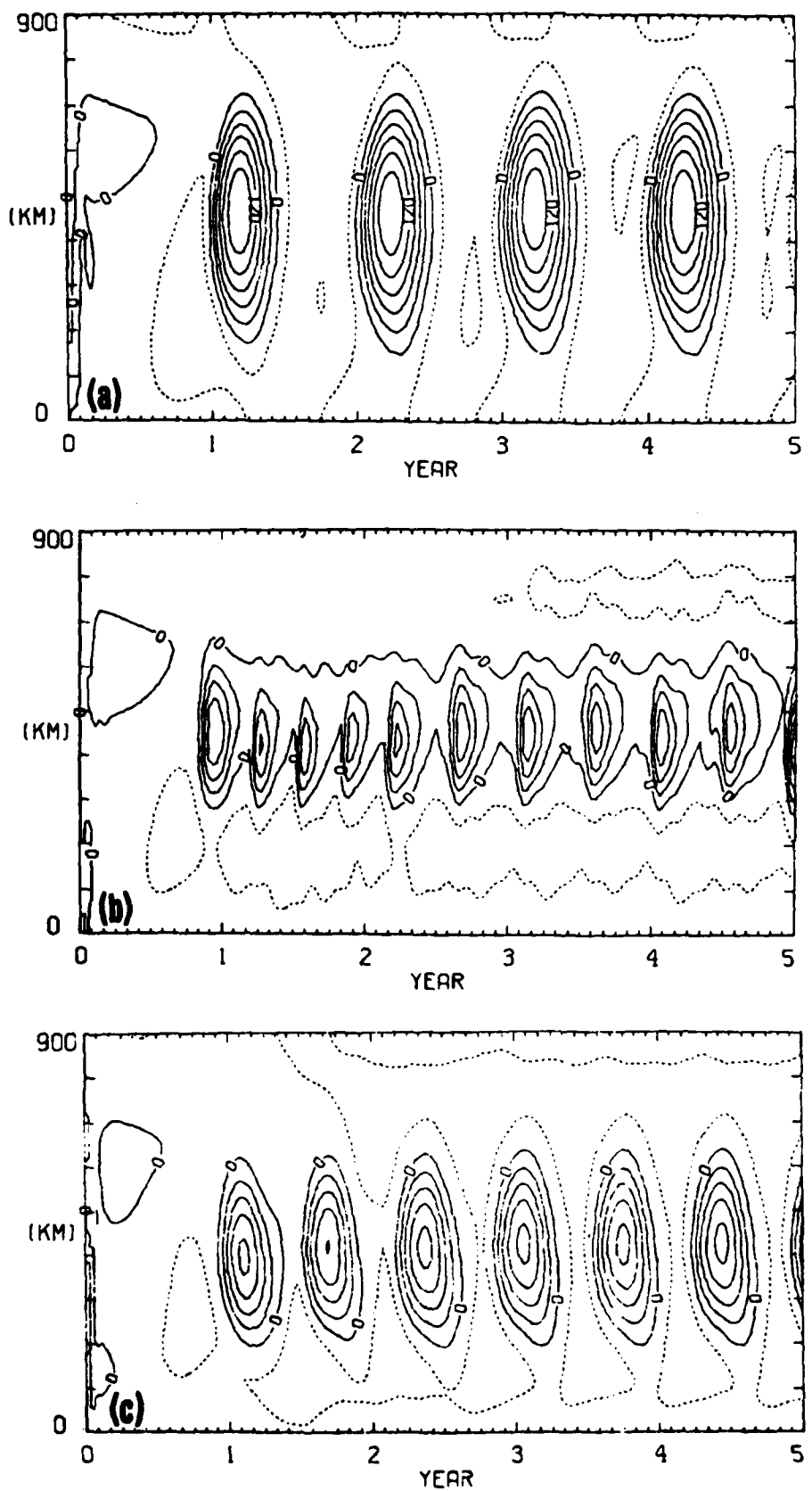


FIGURE 25

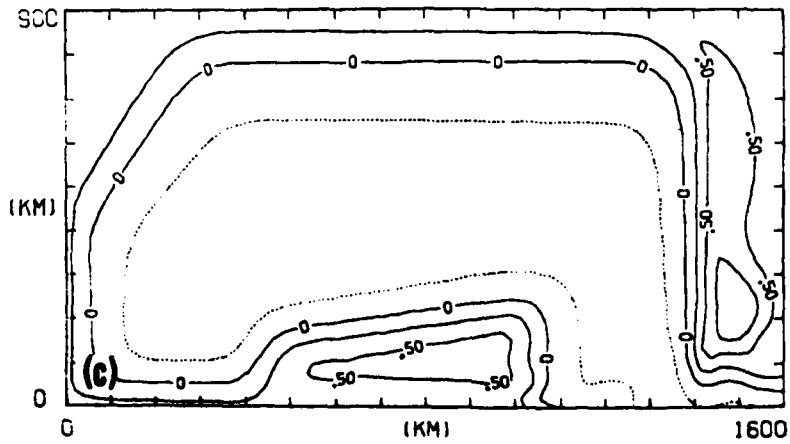
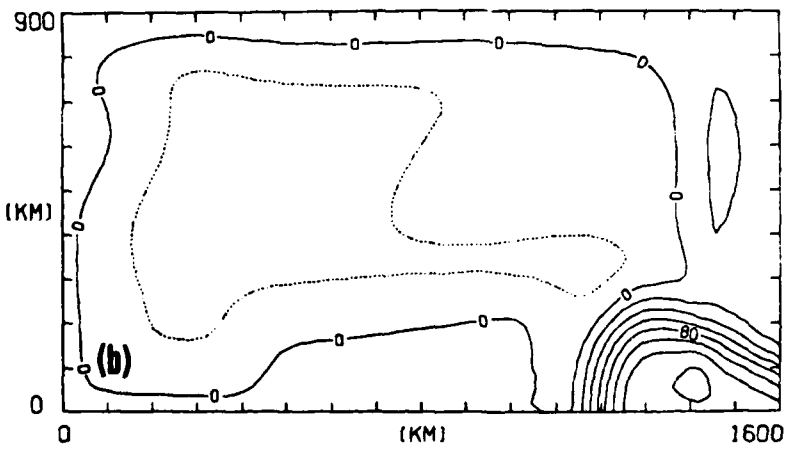
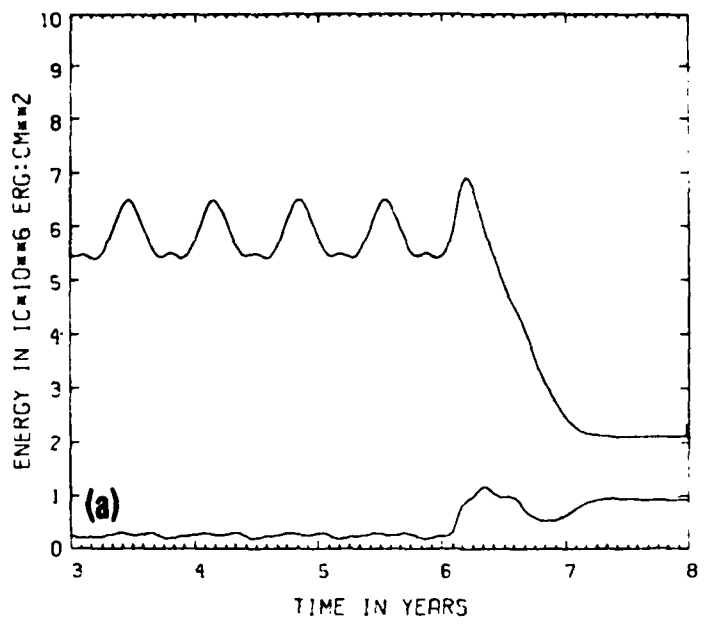


FIGURE 26

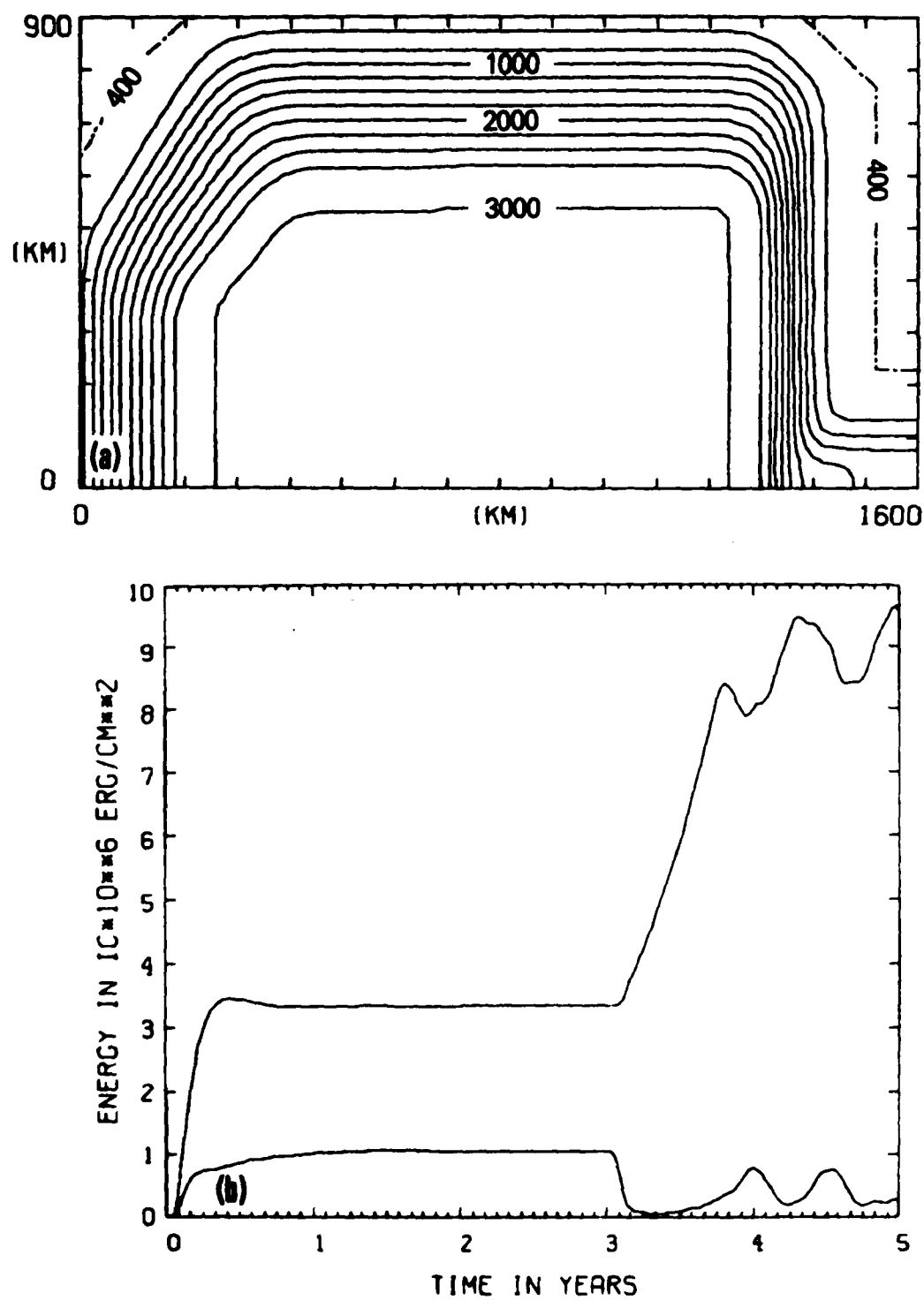


FIGURE 27

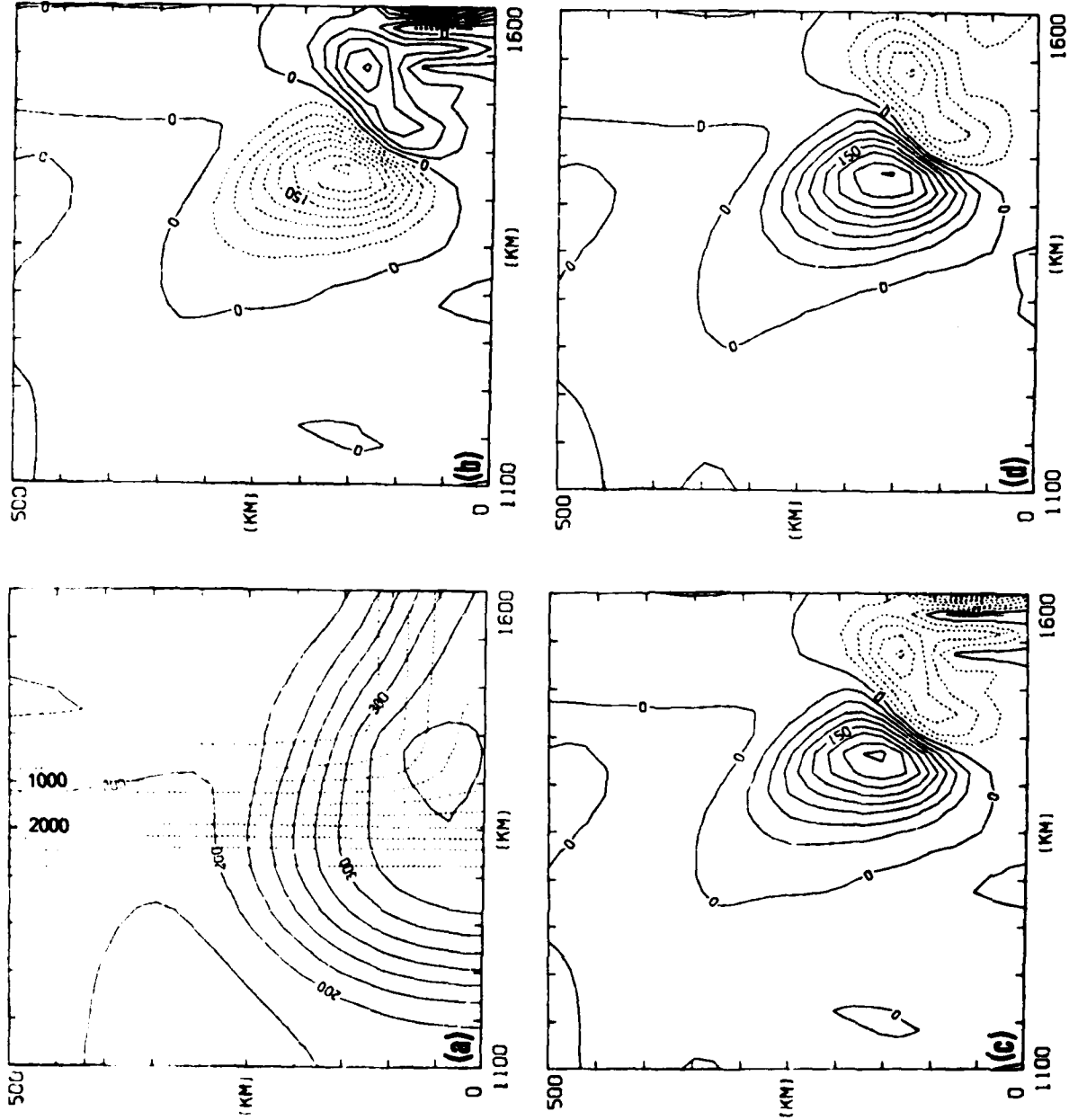


FIGURE 28

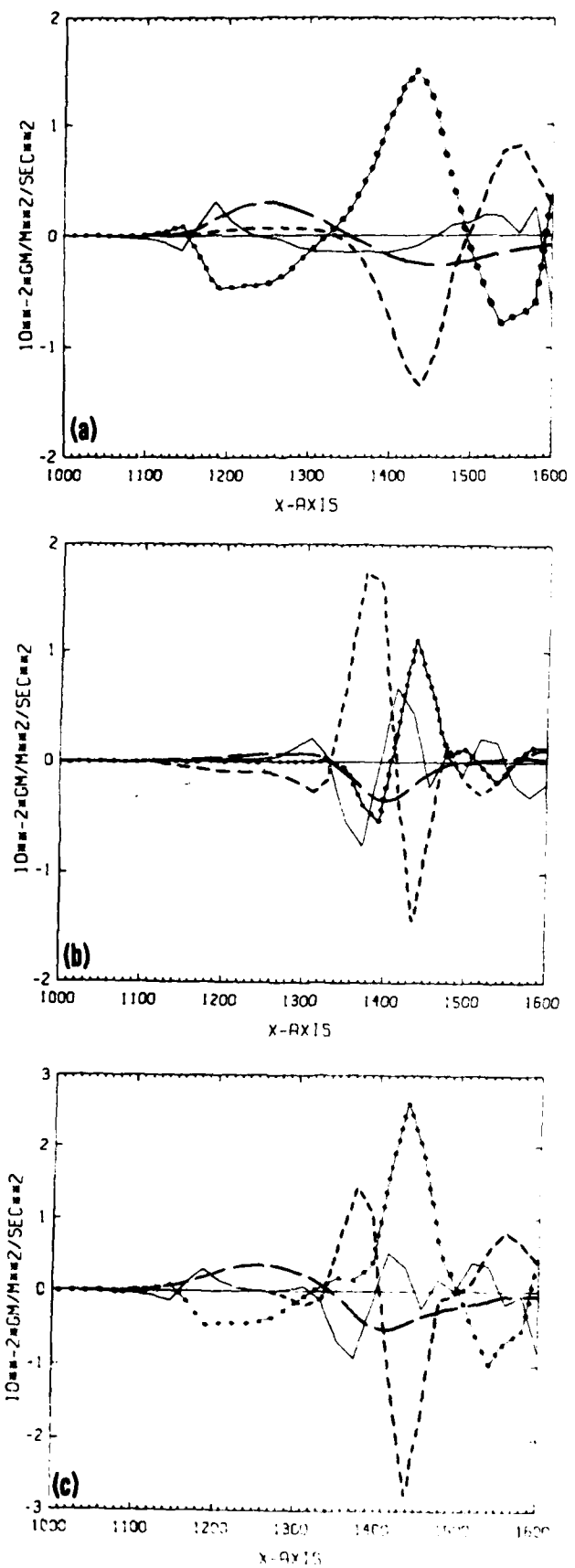


FIGURE 29

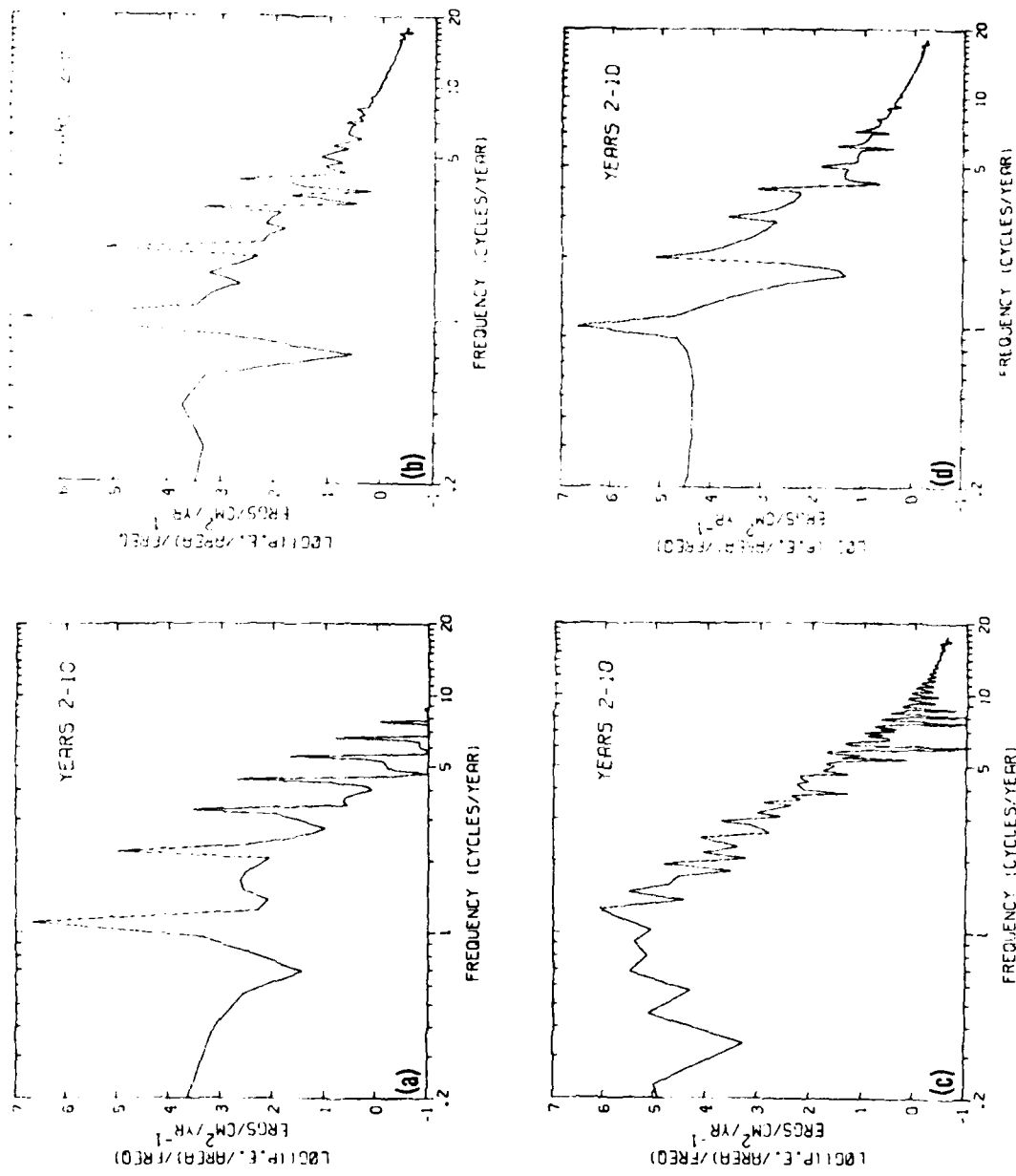


FIGURE 30

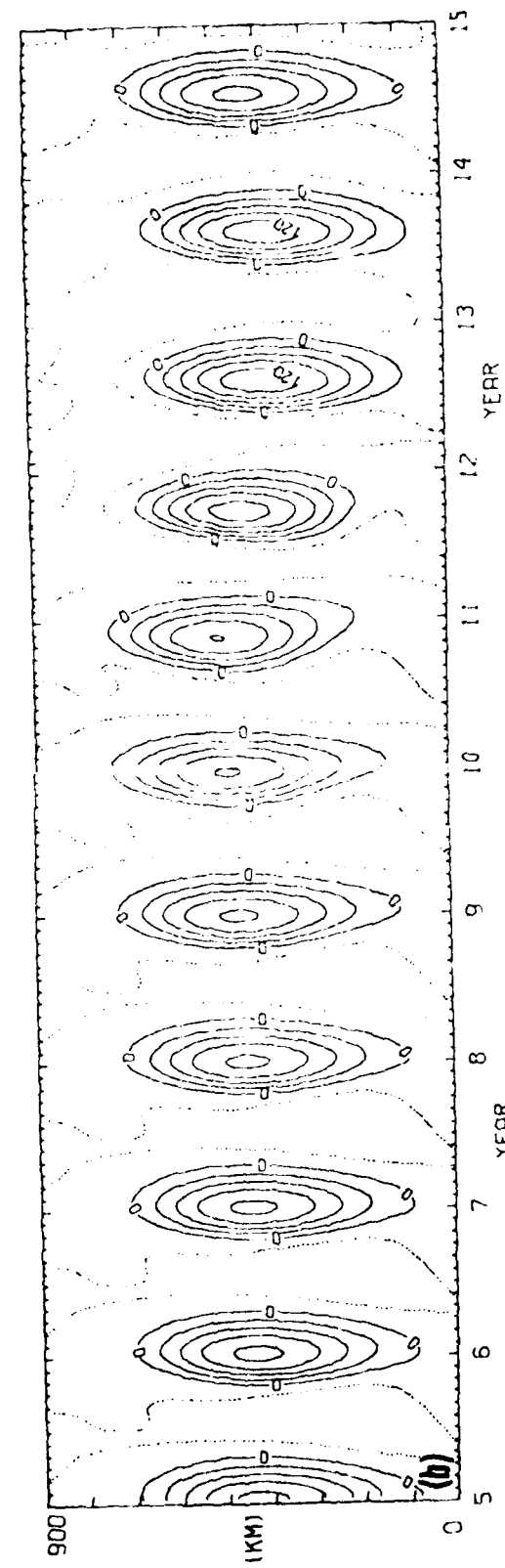
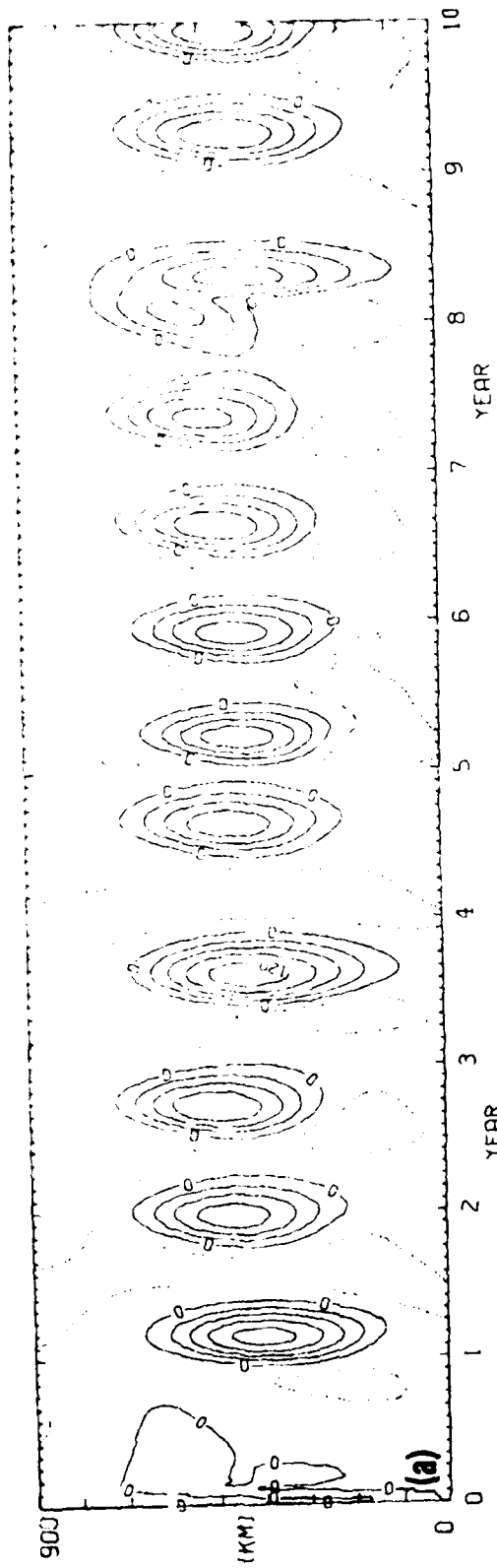


FIGURE 31

SECURITY CLASSIFICATION OF THIS PAGE (When Data Entered)

REPORT DOCUMENTATION PAGE		READ INSTRUCTIONS BEFORE COMPLETING FORM
1 REPORT NUMBER NORDA Technical Note 64	2 GOVT ACCESSION NO.	3 RECIPIENT'S CATALOG NUMBER
4 TITLE (and Subtitle) A Numerical Study of Loop Current Intrusions and Eddy Shedding		5 TYPE OF REPORT & PERIOD COVERED
		6 PERFORMING ORG. REPORT NUMBER
7 AUTHOR(s) H. E. Hurlburt & J. Dana Thompson		8 CONTRACT OR GRANT NUMBER(s)
9 PERFORMING ORGANIZATION NAME AND ADDRESS NORDA, Code 322, Bldg. 1100 NSTL Station, MS 39529		10 PROGRAM ELEMENT PROJECT TASK AREA & WORK UNIT NUMBERS
11 CONTROLLING OFFICE NAME AND ADDRESS		12 REPORT DATE 6/20/80
		13 NUMBER OF PAGES 121
14 MONITORING AGENCY NAME & ADDRESS (if different from Controlling Office)		15 SECURITY CLASS. (of this report) Unclassified
		15a DECLASSIFICATION/DOWNGRADING SCHEDULE
16 DISTRIBUTION STATEMENT (of this Report) Unlimited		
DISTRIBUTION STATEMENT A Approved for public release Distribution Unlimited		
17 DISTRIBUTION STATEMENT (of the abstract entered in Block 20, if different from Report)		
18 SUPPLEMENTARY NOTES		
19 KEY WORDS (Continue on reverse side if necessary and identify by block number) Loop Current; Gulf of Mexico; eddies; instabilities; semi-implicit numerical model, numerical models		
20 ABSTRACT (Continue on reverse side if necessary and identify by block number) The dynamics of the eddy shedding by the Loop Current in the Gulf of Mexico have been investigated using three nonlinear numerical models: two-layer, barotropic, and reduced gravity. The barotropic and reduced gravity models demonstrate the individual behavior of the external and internal modes, and provide insight into how they interact in the two-layer model. Because of the economy of the semi-implicit free surface models, it was possible to perform over 100 experiments to investigate the stability properties of the Loop		

Current. Typically the models were integrated 3 to 5 years to statistical equilibrium on a 1600 x 900 km rectangular domain with a resolution of 20 x 18.75 km. Prescribed inflow through the model Yucatan Channel was compensated by outflow through the Florida Straits.

A long-standing hypothesis is that the Loop Current sheds eddies in response to quasi-annual variations in the inflow. We find that the Loop Current can penetrate into the Gulf, bend westward, and shed realistic anticyclonic eddies at almost an annual frequency with no time variation in the inflow. In this regime, the eddy shedding rate depends on the internal Rossby wave speed, an eddy diameter derived from conservation of potential vorticity on a β -plane, the angle of the inflow, and to a lesser extent on the Reynolds number. Eddy shedding can be prevented by reducing the Reynolds number sufficiently. However, the Loop Current still spreads far westward. The steady state solution for a highly viscous case was found to be almost the same as the mean over an eddy cycle for a lower viscosity case which shed discrete eddies of large amplitude. Eddy shedding and westward spreading of the Loop can be prevented at higher Reynolds numbers when the beta Rossby number, $R_B = v_C / (\beta L_p^2) \cdot 2$, where the appropriate length scale, L_p , is one-half the port separation distance and v_C is the velocity at the core of the current. Differential rotation (β) is also of great importance in determining the diameter and westward speed of the eddies and the penetration of the Loop Current into the Gulf. In a few of the two-layer experiments, baroclinic and mixed instabilities were encountered, but experiments dominated by a horizontal shear instability of the internal mode produced the most realistic results. For sufficiently high Reynolds numbers the shear instability occurred in both the barotropic and reduced gravity models. However, for realistic parameter values eddy shedding occurred in the two-layer and reduced gravity models, but not in the barotropic model.

Consistent with potential vorticity conservation dynamics, the Loop Current and its eddy shedding behavior was quite insensitive to the location and width of the inflow and outflow ports, so long as the western boundary did not interfere with the shedding process and the ports were not separated by much less than $1/\sqrt{2}$ times the theoretical eddy diameter, i.e., when $R_B < 2$. When the entire eastern boundary was opened, the outflow remained confined to a current adjacent to the southern boundary. Also, while the solution depends on the maximum velocity at inflow, it is relatively insensitive to the shape of the inflow profile.

In the presence of significant deep-water inflow through the Yucatan Straits, bottom topography may prevent Loop Current penetration, westward spreading, and eddy shedding. In these cases the interaction between the bottom topography and the pressure field near the Florida Shelf results in a near balance between the pressure torques and the nonlinear terms in the mass transport vorticity equation. When the Yucatan Straits deep water inflow is reduced or the Florida Shelf is moved to the east, the eddy shedding reappears. A kinematic analysis shows that a sufficiently strong current following f/h contours of the Florida Shelf and intersecting the Loop Current at large angles can locally prevent northward penetration of the Loop Current and effectively reduce the port separation. Thus, the effect of the Florida Shelf is similar to cases in the reduced gravity model where the ports are too close for eddy shedding to occur, i.e., when $R_B \geq 2$. Bottom topography also inhibits development of baroclinic instability, yielding solutions more closely resembling those from the reduced gravity model than from the two-layer flat bottom model. However, movement of the shed eddies is significantly modified by the introduction of topography.

In the presence of realistic time variations in the upper layer inflow, the eddy shedding period is dominated by the natural period rather than the forcing period, although the influence of the latter is not negligible.

